Molecular Simulation Studies in Periodic Mesoporous Silicas SBA-2 and STAC-1: Model Development and Adsorption Applications

Carlos Augusto Ferreiro Rangel

PhD
The University of Edinburgh
Institute for Materials and Processes
2011

Declaration

I, Carlos Augusto Ferreiro Rangel, hereby certify that this thesis, which is approximately 42000 words in length, has been composed by me. The work presented is a contribution to the EU project “Design Synthesis and Application of Novel Nanoporous Adsorbent Component“ (DeSANNS) and my own, except for where it is stated to be the work of other members of the project team. Furthermore, this work has not been submitted for any other degree or professional qualification.

15 February 2011, ……

Carlos A. Ferreiro R.

Abstract

Adsorption is a low-energy separation process especially advantageous when the components to be separated are similar in nature or have a low molar concentration. The choice of the adsorbent is the key factor for a successful separation, and among them periodic mesoporous silicas (PMS) are of importance because of their pore sizes, shapes and connectivity. Furthermore, they can be modified by post-synthesis functionalisation, which provides a tool for tailoring them to specific applications.

SBA-2 and STAC-1 are two types of PMS characterised by a three-dimensional pore system of spherical cages interconnected by a network of channels whose formation process was until now obscure. In this work the kinetic Monte Carlo (kMC) technique has been extended to simulate the synthesis of these complex materials, presenting evidence that the interconnecting network originates from spherical micelles touching during their close-packing aggregation in the synthesis. Moreover, for the first time atomistic models for these materials were obtained with realistic pore-surface roughness and details of the possible location of its interaction sites.

Grand Canonical Monte Carlo (GCMC) simulations of nitrogen, methane and ethane adsorption in the materials pore models show excellent agreement with experimental results. In addition, their potential as design tools is explored by introducing surface groups for enhancing CO_2 capture; and finally, application examples are presented for carbon dioxide capture from flue gases and for natural gas purification, as well as in the separation of n-butane / iso-butane isomers.

Acknowledgements

This thesis is a result of the driving force of the unknown, the craving need to explain what is not fully understood and the satisfaction of adding a little contribution to a big jigsaw. But many things that develop alongside research are not said in these pages: experiences, friendships, endings and beginnings of a life cycle that blossoms with every day that dawns.

It is through the support and encouragement of family and friends that I have been able to reach this point, to write these lines and present the reader with my little piece of the jigsaw. I cannot mention all of them in these pages since the space is scarce, but I do want to thank here: Prof. Seaton (Nigel) and Dr. Düren (Tina) whose impeccable guidance and advice made me a better researcher, and a better person, and to whom I am eternally grateful for granting me the opportunity and the means to work alongside them; Dr. Schumacher for its detailed work on MCM-41, on which this work is mostly based; Dr. Sarkisov (Lev) and Prof. Wright (Paul) for useful discussions on the different aspects of the thesis; the one person who day by day stands by me and brings sunshine and joy on those cloudy days, my dear wife Belen; my parents for always encouraging and supporting me; Prof. Olivera-Fuentes who opened my horizons; and my colleagues from the Institute for Materials and Processes (Qiong, Claudia, Carmelo, Patty, Jose, Eduardo, Jennifer, David, Eve, Alessandro, Gaetano) for their insights, and above all their everlasting friendship.

I also want to thank the employees at the University of Edinburgh, especially those who helped me set up and run my simulations in the computer clusters CLX and EDDIE; and the University of Edinburgh, and the EU DeSANNS project for financial support. This thesis could hardly have been possible without their help.

And finally, I dedicate this thesis to all the people mentioned above, and I hope it will provide you with useful information and tools to use on your quest to explain new and exciting phenomena, and add your little piece to the big picture.

(Page left blank intentionally)

Table of Contents

List of Tables

List of Figures

1. Introduction: Modelling Periodic Mesoporous Silicas

1.1. Gas Separation Processes

Separation processes take a mixture of substances and alter it, so that two or more products with different composition are obtained. They account for most of the production costs in the chemical and petrochemical industries (Yang 1997), and although distillation is the most common technique for large-scale applications the use of adsorption is growing because it is energetically less intensive and it is advantageous under certain conditions, as for example when the relative volatility between the components of the mixture is similar (< 1.5) or when the composition of the species to be separated is low.

Adsorption is a surface-driven process. When the pore-surface of a porous solid is exposed to a gas attraction forces act between them and gas molecules attach to the surface. When the gas-solid interactions are weak ($\sim 1\times10^{-20}$ J/molecule) the process is said to undergo physisorption, which means the gas molecules are retained by the surface of the solid preserving their chemical identity. Otherwise, when the interactions are stronger ($\sim 10\times10^{-20}$ J/molecule) the process is called chemisorption and the adsorbate molecules form chemical bonds with the surface. The attractive forces are strongly related to the nature of the adsorbent (the solid surface) and the adsorbate (the gas) molecules. For example, polar surfaces show preferential attraction towards polar adsorbates while neutral surfaces, such as graphitic layers, have more affinity towards non-polar molecules such as hydrocarbons chains (methane, ethane, etc.).

Since adsorption is a surface phenomenon, it follows that the total surface area of the adsorbent is an important parameter to consider. Furthermore, the size and shape of the adsorbent pores have a strong influence on the final outcome of the separation

process, and in fact the evolution of adsorption as a separation technique over the last few decades is greatly due to the development of new, more efficient adsorbents.

1.2. Adsorbents

Pore size has been classified by the International Union of Pure and Applied Chemistry (IUPAC) as follows: micropores as those smaller than 2 nm in diameter, mesopores if they are within 2-50 nm in diameter, and macropores if they exceed 50 nm in diameter. Nanoporous materials are a subset of porous materials with large porosities and pore diameters within 1-100 nm (Lu and Zhao 2004). The smaller the pore size the stronger the interaction between the gas and the pore walls, which is why microporous and mesoporous materials have been the focus of adsorption studies for many years. The focus of this thesis project is the study of mesoporous adsorbents.

Mesoporous materials, besides being remarkable adsorbents, are also valuable in other fields like ion exchange, sensor design, and catalysis among others; but in what follows we will focus on their use in separation processes by adsorption. Different nanoporous materials with different pore sizes, pore shapes, connectivity, etc. may exhibit different separation properties that will determine their usefulness for a specific application. In general however, any potential adsorbent must have the following characteristics,

- Show significant adsorption at low pressures (where the solid-fluid interactions predominate)
- Show a high adsorption capacity at high pressures (which mostly depends on the pore volume)
- Be selective: the best possible adsorbent will adsorb preferentially one substance over the other components in the fluid mixture. Here the nature of the surface plays an important role
- Mechanical stability to withstand the stress forces in adsorption columns

- Thermal and chemical stability. The properties of the adsorbent must remain unchanged even at the high pressures or temperatures that may be required for the separation process

1.3. Introduction to Periodic Mesoporous Silicas (PMS)

Periodic mesoporous silicas (PMS) are amorphous silicates (which may have other metal cations such as aluminium) with a uniform pore structure. The study of these materials increased sharply after 1990, when the Mobil Corporation Laboratories published the controlled synthesis of a material named MCM-41, where MCM stands for Mobil Crystalline Materials (Kresge et al. 1992). During the next decade, silica materials with larger pores and different pore shapes were synthesised at the University of California. These materials are known as the SBA (Santa Barbara Amorphous) family (Huo et al. 1994a).

The main idea behind the synthesis of PMS lies in the polymerisation of a silica precursor in the presence of templating micelles formed by surfactants. Surfactants are surface-active agents. Their main characteristic is that they are amphiphilic, that is to say they contain a hydrophobic part (known as the tail) and a hydrophilic part (known as the head). When the concentration of the surfactants is increased beyond a certain threshold (known as the critical micelle concentration, CMC) they aggregate forming micelles. A micelle is a cluster of surfactants where the hydrophilic heads are in contact with the surrounding solution while the hydrophobic tails are in contact with one another shielded from the solution by the surfactant heads.

The shape of these micelles depends on a number of factors such as temperature, pH, type of surfactant and surfactant concentration. Therefore, a controlled synthesis of PMS can lead to specifically desired structures by:

- Changing the composition of the mother solution, and so changing the type of structure obtained
- Increasing the tail-lengths of the surfactants, resulting in increased pore size and distance between pores
- Using swelling agents (normally an organic substance like methyl-benzene), thus increasing the pore size

Another advantage of PMS is that they can be modified post-synthesis by reflux with a substituted silica source. In other words, it is possible to functionalise the material by placing surface groups on the pore surface. So, even after a certain structure has been achieved the properties of the pore walls can be further tailored to target specific adsorbate molecules.

1.4. Molecular simulation of adsorbents

Any chemical or separation plant deals with large units: tons, gallons, days, etc. That is to say, they are designed to operate continuously at large scales, for which macroscopic equations can be applied which explain phenomena visible to the naked eye. However, in many cases in order to fully understand the physics involved in a phenomena it is necessary to look at it from a microscopic point of view by studying the atom-atom interactions of the molecules within the system.

Molecular simulations look at obtaining the molecular description of a system along with the numerical solution to the equations relating the properties on the molecular scale to those of the collective macroscopic system using statistical mechanics. Statistical mechanics is a tool that transforms statistical averages from a group of atoms or molecules into thermodynamic fluid properties that can be measured and quantified on the macroscopic scale. For this reason, molecular simulations can be regarded as a theoretical workshop (CECAM 2010) to test and develop theories that help to better understand the macroscopic phenomena.

Molecular simulations can be quantum or classical. The first are mathematical descriptions of the particle-like and wave-like interactions of energy and matter in a system at atomic and subatomic scales. Quantum mechanics is based on the wave function, which is a mathematical description providing the probability amplitude of position and momentum of a particle. Classical molecular simulations (such as the ones used in this work) on the other hand study the motions of atoms/molecules constrained within a certain volume where the nuclear motion of the molecules obey the laws of classical mechanics. The two main techniques to perform classical molecular simulations are,

- *Molecular Dynamics*. It is used to compute either the equilibrium or transport properties of a classical many-body system (Frenkel and Smit 2001). In a molecular dynamics study the Newton's equations of motion are solved for a model-system consisting of *N* particles. This is done until the property (or properties) of the system no longer vary (steady state).
- *Monte Carlo*. It is based on the random occurrence of events and unlike molecular dynamics it is mostly used to study systems in equilibrium. Monte Carlo is usually much faster than molecular dynamics.

As far as adsorption is concerned, molecular simulations can be very useful in the study and development of adsorbents, as it provides the appropriate tools to study the solid-fluid interactions of the system and may thus reveal the weaknesses and strengths of an adsorbent for a specific application. Adsorption isotherms, diffusion coefficients, adsorption mechanisms and design parameters can all be obtained when the appropriate molecular simulation technique is applied.

1.5. Carbon capture: today's problem

The behaviour of the periodic mesoporous silica SBA-2 as a potential CO_2 adsorbent is investigated in this thesis. Carbon dioxide is a greenhouse gas that is creating great concern due to its environmental impact. Although there are other greenhouse gases in the atmosphere such as water, methane, and ozone, it is the

steady rise of atmospheric carbon dioxide since the industrial revolution (in the 19th century), and especially during the last decades, that is creating great concern. At present, the UK alone emits over 500 millions of tonnes of carbon dioxide per year (UK Research Council 2011). Carbon capture is one of the most pressing issues to help control the CO_2 being released to the atmosphere, so that later it can be safely disposed of by means of underground (or deep-sea) storage as shown in Figure 1-1.

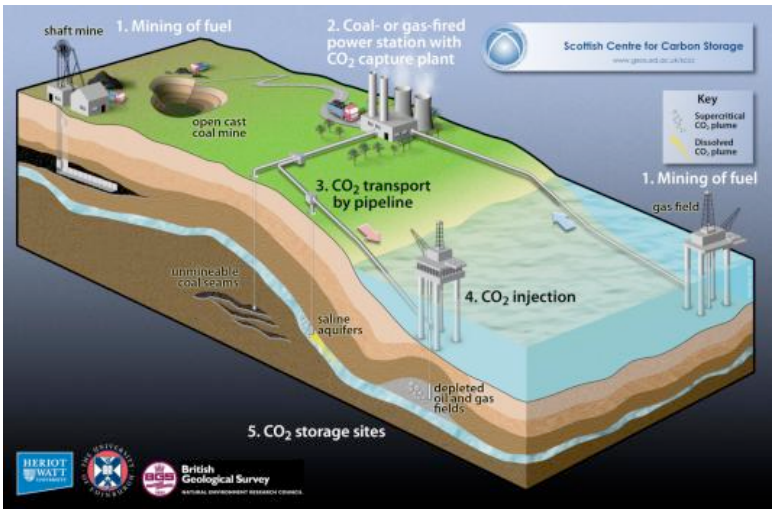

Figure 1-1: Conceptual plan for CO_2 capture and storage (UK Research Council 2011).

The main goal of this technology is not to fully stop carbon dioxide emissions but to reduce them to acceptable levels, and it is aimed at the largest sources of carbon dioxide, which, of all the human processes, is the generation of electricity by burning coal (or natural gas) in power plants. This should help reduce the amount of CO_2 being released into the atmosphere to acceptable levels, while alternative green technologies such as fuel cells for cars and solar and wind energy for power generation (among others) are sufficiently developed to substitute current oil based technologies.

The capture of carbon dioxide from industrial processes is, in general, achieved through one of the following techniques: absorption (currently used in pilot-scale schemes for the capture of carbon from power plants), adsorption, physical separation (by means of, for example, membranes), and hybrid solutions (Ebenezer 2005). Current absorption-based technologies require complicated and costly

absorption plants with high operating costs due to corrosion and regeneration of the absorbent (Sweatman 2010, Delgado et al. 2007), which is why less costly and less energy intensive alternatives are needed. Pressure-swing adsorption (PSA) is one such initiative due to its low initial investment and low energy costs. As an example, the energy cost per ton of CO_2 recovered from flue gases for an amine based absorption process is about 335 kWh, rather than about 170 kWh as required by a PSA process (Delgado et al. 2007). Thus, it is important to search for porous solids that show good carbon dioxide uptake by adsorption and at the same time show good regenerative properties.

Though the most pressing reason for CO_2 capture is environmental, it is not the only one. Natural gas from landfill sources is a gas containing around 45-65 % molar composition of methane and less than 1 % of gases other than carbon dioxide (thus having a large composition of this gas). Carbon dioxide removal here is important because its presence lowers the calorific content of the gas, and also because carbon dioxide is an acidic gas that corrodes the transporting pipes. For that reason, pipelines for natural gas (in general) require very low concentrations of carbon dioxide (below 2-3 %) (Delgado et al. 2007).

1.6. Thesis scope

In this thesis the use of two related amorphous periodic mesoporous silicas named SBA-2 and STAC-1 in adsorption is investigated through classical molecular simulation. For this purpose pore models are created by means of the kinetic Monte Carlo technique (kMC) prior to conducting adsorption simulations using grand-canonical Monte Carlo (GCMC).

In order to achieve accurate adsorption predictions using molecular simulations it is necessary to have a good molecular model of the adsorbent. For crystalline adsorbents such as zeolites, the solid framework structure is known from experimental tests like X-ray or neutron diffraction. However, both STAC-1 and

SBA-2 are amorphous periodic mesoporous silicas, which means that although they exhibit an overall long-range order, the short-range position of the atoms with respect to one another is unknown and variable.

A first, less accurate yet simple, approximation would be to model such materials by means of idealized geometrical structures, as it was done for MCM-41 by Düren *et al.* (Düren 2002) and for SBA-2 by Perez-Mendoza *et al.* (Perez-Mendoza et al. 2004a, Perez-Mendoza et al. 2004b). However, these models are too simple and do not capture some important aspects of the adsorbents. A better model takes into account the irregularities of the pore surface on the atomistic scale (from now on defined as rugosity). Schumacher *et al.* (Schumacher et al. 2006b) developed such a model for MCM-41 by mimicking its synthesis process, which allowed accurate predictions of the adsorption of different gases [(Schumacher et al. 2006b), (Herdes, Ferreiro and Duren 2011)].

SBA-2 presents a more complicated structure than that of MCM-41, having a system of spherical pores connected by comparatively small channels (Zhou et al. 1998). This makes it a good candidate for adsorption applications and catalysis because the small connecting channels can provide molecular sieving effects. The previous simple models used (Perez-Mendoza et al. 2004a) were found insufficient to describe this material, and thus one of the goals of this PhD project was to develop a realistic pore model for SBA-2 which, besides providing a good representation of the material for adsorption processes, would also give information about the formation of key structural features such as the network of interconnecting channels.

To achieve this goal, a kinetic Monte Carlo approach, based on that used for MCM-41 (Schumacher et al. 2006b), was developed which mimics the synthesis of STAC-1 and SBA-2 materials. This approach is explained in Chapter 2, whereas Chapter 3 explains in detail the statistical mechanics approach to simulate adsorption using the developed pore models, provides adsorption predictions and their comparison to experimental adsorption isotherms in order to validate the adsorbent

models, and give insight into the adsorption mechanism of many adsorbate-adsorbent systems.

Chapter 4 deals with material design, tailoring a STAC-1 pore model towards CO_2 capture. Different surface groups are introduced onto the pore surface in order to study the overall effect on carbon dioxide adsorption. Then, Chapter 5 studies the potential use of either STAC-1 or SBA-2 as adsorbents in carbon capture (from either natural gas or flue gases) and in n-butane / iso-butane separation processes. Finally, Chapter 6 contains the conclusions from this work and looks into future research directions.

2. Simulating the Synthesis of PMS

As was mentioned in the previous chapter, in order to assess the suitability of a material for a given adsorption application it is necessary to better understand how it interacts with the fluid passing through its porous network. Molecular simulations provide the tools to do this as long as the molecular representation of the material is sufficiently detailed.

With periodic mesoporous silicas (PMS) this is not a simple task as these materials are amorphous on the atomistic scale. However, Schumacher and co-workers (2004) successfully applied a kinetic Monte Carlo (kMC) technique to obtain what, to our knowledge, is the most detailed atomistic representation of MCM-41 to date. Their approach takes into account the key synthesis stages leading to the final structure of the silica, as it will be pointed out later in this chapter.

An overview of the kMC technique is given as developed for MCM-41 (Schumacher et al. 2006b). Then, the steps taken to further develop and adapt this technique to accomplish realistic atomistic models for STAC-1 and SBA-2 are explained in detail.

2.1. Periodic Mesoporous Silicas (PMS)

2.1.1. Experimental synthesis of periodic mesoporous silicas

Periodic mesoporous silicas may be tailored into many structures (Huo et al. 1994b) and are an important area of materials science. They require thorough characterisation due to their lack of crystallinity. Thus, an X-ray diffraction experiment will not reveal the exact position of the atoms throughout the material, as it does for crystalline solids, which makes creating a realistic model for them very difficult.

The first materials of this kind to be synthesised belonged to the MCM-41 family, and were observed by examining the electron micrographs of the products obtained by hydrothermal reactions of aluminosilicates gels in a quaternary ammonium surfactant (Kresge et al. 1992). Roughly, a typical synthesis of MCM-41 requires the following ingredients:

- A basic water solution prepared with sodium hydroxide (NaOH). The pH is then controlled with acetic acid
- A surfactant compound, the length of its hydrophobic tail playing an important role in the size of the pores of the final material (Kresge et al. 1992)
- A source of silica, the usual choices being tetraethyl-orthosilicate (TEOS) or tetramethyl-orthosilicate (TMOS); although a mixture of silica sources (or combined silica/alumina sources (Kresge et al. 1992)) can be used especially when preparing in-situ substituted materials

A variety of silica sources and surfactants as well as concentration ratios and time/temperature ranges can be used for producing materials from this family (Corma 1997)). The overall process follows this recipe,

- The aqueous sodium hydroxide solution is prepared.
- The surfactant is added to this solution.
- The silica source is added; then the solution is stirred for a sufficiently long time to promote precipitation, using acetic acid to maintain the pH constant.
- The mother solution is placed in an autoclave at high temperature for about a day.
- The precipitate is filtered and dried in air.
- Finally, the solid is calcined at high temperatures (usually over 823 K) to remove the organic content using a constant flux of nitrogen for 5 hours followed by oxygen for another 5 hours. Although calcination temperatures

need to be high, it must be borne in mind that the risk of damaging the long-range order of the material increases with increasing temperature.

There is also the possibility of using swelling agents during the synthesis. A swelling agent is an organic species which solubilises in the hydrophobic region of the solution, therefore helping increase the size of the resulting pores in the inorganic product (Zhao et al. 1998).

The sol-gel polymerisation of silica in aqueous solutions has been a subject of study on its own accord (Ng and McCormick 1996). At first a theory was proposed based on the assumptions of mean field functional group kinetics and no intramolecular reactions (cyclization) taking place: the random branching theory (RBT). However, further study of the reaction kinetics revealed that over a wide range of compositions non-random cyclization occurred. A new model was then proposed that no longer assumes a mean field approximation and rather looks further into the effects of pH on the kinetics of the process.

In this regard, it is observed that for high water/silica ratios (>2) acidic conditions below the isoelectric point favour cyclization – and early aggregation – while low water/silica ratios were impervious to pH. Furthermore, as the pH increases bimolecular reaction competes with cyclization favouring the formation of large branched polymers. This means that under acidic conditions aggregation of silica clusters occur sooner than they would in a basic environment. The pH of a solution can be controlled by means of electron donor/receptor substances, and for that purpose hydrochloric acid ($H_3O^+Cl^-$) and tetramethyl-ammonium hydroxide (TMAOH, which is $N(CH_3)_4^+OH^-$) are usually employed (Ng and McCormick 1996).

It was proposed that the synthesis mechanism follows a “liquid-crystal” template path (Kresge et al. 1992) where the inorganic material occupies the continuous solvent region to create the inorganic structure dividing the surfactant regions. In the case of MCM-41 the micelles are cylindrical with the tails of the surfactant occupying the centre of the cylinder. However, further studies suggested that the

liquid crystalline phase is not present, but that randomly ordered rod-like micelles accumulate layers of silica around them before spontaneously forming the long ranged order of the final product (Corma 1997).

Thus, the following synthesis stages take place (Figure 2-1) (Corma 1997, Schumacher et al. 2006b):

1) Surfactant molecules aggregate and form rod-like micelles dispersed in the solution.
2) The silica source hydrolyses quickly forming silicic acid. The silicic acid molecules are attracted by the charged surface of the micelles promoting their condensation (that is, a chemical reaction by which the silica polymerises).
3) After a thin layer of silica forms surrounding the micelles, further condensation of the silica monomers occurs and the micelles aggregate into a hexagonal regular array, which is the precursor of the final long-range order.
4) As the silica condensation evolves, the silica skeleton of the final material takes shape.

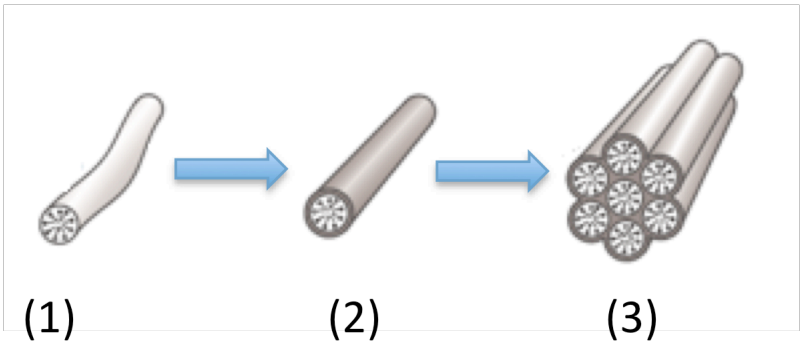

Figure 2-1: Schematic representation of the synthesis mechanism of mesoporous silica MCM-41 [adapted from (Corma 1997)]. (1) Formation of micelles from surfactant aggregation, (2) condensation of silicic acid monomers around a micelle, (3) aggregation of micelles into the final long-range order of the material.

In 1994, Huo and co-workers (Huo et al. 1994b) went further and described four pathways to synthesise mesoporous materials depending on the cationic/anionic nature of both: the surfactant and the inorganic solution species. When the polarity of

the solutions and the surfactants is opposed a direct co-condensation of the species involved is said to occur, indirect co-condensation being proposed when the inorganic solution and the surfactant hydrophilic heads are the same, either cationic or anionic. They proposed a synthesis mechanism based on the cooperative organization of the silicate-surfactant mesophase, where the driving force is the charge density matching at the surfactant inorganic interfaces, and it is suggested that these mechanisms can be extrapolated to the synthesis of other silica-based mesoporous materials.

Under this model it is the charge matching at the surfactant-inorganic interface rather than micelle aggregation what governs the final type of structure generated (Corma 1997). Implicitly then, the early interactions between the silicate and the surfactant play an important roll on the synthesis process, and this is backed up by experimental formation of structures that do not occur in pure surfactant solutions but only in presence of silicate (Firouzi et al. 1995). However, it has been found that the silica condensation and aggregation mechanism is adequate to obtain realistic models for MCM-41 type materials (Schumacher et al. 2006b) by means of kinetic Monte Carlo, and for this reason this synthesis mechanism is adopted for the remainder of this work.

Depending on the synthesis conditions, as well as on the type of surfactant used, it is possible to obtain micelles with different shapes (Huo, Margolese and Stucky 1996) that lead to materials with different pore-shapes and silica structures. For example, using gemini surfactants is possible to obtain spherical micelles, and the materials obtained this way (named SBA-2 and STAC-1) have been shown to be more complex than MCM-41 (Zhou et al. 1998, Hunter and Wright 2001) since they exhibit a higher pore-connectivity making them more attractive for adsorption and catalysis applications (Perez-Mendoza et al. 2004b).

The first part of this research focuses on adapting the kinetic Monte Carlo technique, based on the silica condensation and aggregation mechanism, to the simulation of the synthesis of these complex materials (SBA-2 and STAC-1). In

order to do that it is essential to describe their experimental synthesis and how it relates to that of MCM-41.

Both SBA-2 and STAC-1 exhibit three-dimensional cage-like structure (Zhou et al. 1998) and are prepared by means of gemini quaternary ammonium surfactants like the one depicted in Figure 2-2. Then, the final silica structure develops from a mother source containing, for example tetramethyl-ammonium hydroxide (TMAOH), tetraethyl-orthosilicate (TEOS), and water in a ratio of 0.05:0.5:1:150 respectively.

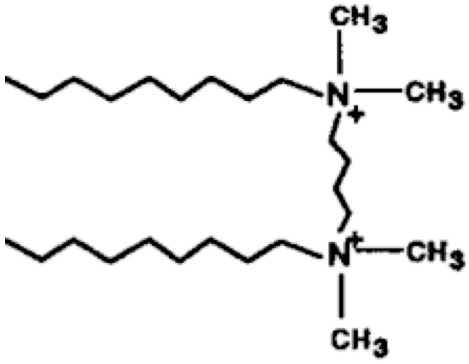

Figure 2-2: Diagram of a gemini surfactant. Adapted from (Huo et al. 1996). The usual gemini surfactant for SBA-2 is $C_{16\text{-}3\text{-}1}$ (16 methylene groups in the hydrophobic chain and three joining the two nitrogen atoms)

It has been found that this synthesis must take place at a pH between 11 or 12 (Prof. Wright 2007-2010), and this is usually achieved by using HCl as a pH regulator. As for MCM-41, stirring of the mixture at room temperature is required (for about 2 hours) after which the solid precipitate is recovered by filtration, washed with distilled water, and dried in air at room temperature. To remove the surfactant in the micelles and produce the desired porous material calcination is necessary and it usually takes place at temperatures above 723 K and below 1123 K for between 2 and 8 hours under the flux of a pure fluid (usually nitrogen, oxygen, or a combination of them). Calcination of this material at temperatures above 1123 K leads to samples where the structure of the material is either broken down due to the high temperatures and/or the few remaining pores are inaccessible (Prof. Wright 2007-2010).

2.1.2. Experimental characterisation of PMS

So far it was explained how periodic mesoporous silicas (PMS) are synthesised with specific examples of MCM-41 and SBA-2. However, to identify possible applications for a PMS as well as to tailor them further for a practical purpose it is necessary to understand both their structure and pore network. These microscopic characteristics can be studied experimentally and they play an important role in validating the simulated models obtained by kMC. Among these tools, the most relevant are mentioned below, (Rouquerol, Rouquerol and Sing 1999).

- **X-Ray powder diffraction (XRD)**: In this method a beam of X-rays hits the sample and diffract in many directions. When the X-rays strike electrons they produce waves (a phenomenon known as elastic scattering) that will cancel out in some directions (destructive interference) but will be strengthen in others by constructive interference. A typical diffraction spectrum consists of a plot of reflected intensities versus the detector angle 2-Θ. This method helps to determine the degree of crystallinity in the material, as well as for the calculation of the unit-cell size of the regular structures.

- **Transmission electron microscopy (TEM)**: This technique requires a beam of electrons to pass through a very thin sample. The resulting interaction between the electrons and the sample provides an image that is later magnified and focused into something discernible by the naked eye. Direct comparison to results from XRD is not possible as the image depends on its processing. The main contribution of this tool is that it provides the means to identify the pore shape and regularity in the sampled material.

- **Si nuclear magnetic resonance (Si NMR)**: This technique provides information on the connectivity of the silicon atoms present in the silica network of the sample. This information is directly related to a parameter

known as Degree of Polymerisation (Q_n) that measures the extent to which a silica monomer is linked to other monomers. The output from Si NMR is a Q_n-distribution, where Q_i refers to the degree to which a monomer has reacted, and the subscript *i* goes from zero (for isolated monomers) to four (for fully linked monomers). Thus, Q_3 for example refers to monomers linked to three other monomers. A fully developed material will typically exhibit distinctive Q_3 and Q_4 peaks. Huo *et al.* presents a good example (Huo et al. 1994b) where the Si NMR for many silica mesophases is shown. Also they compare the outputs obtained for two hexagonal phases: phase A obtained after 30 min reaction, and phase B obtained after 2 h reaction. These results show a 53 % Q_3 and 47 % Q_4 in the hexagonal phase A in contrast to a 36 % Q_3 and a 61 % Q_4 for the hexagonal phase B. This indicates that the longer the reaction time the greater the silanol condensation in the material.

- **Helium pycnometry:** it consists on passing helium through the porous material assuming that it behaves as an ideal non-adsorbent gas. That means that the amount of helium retained inside a porous solid at a given temperature and pressure has the same density as it would have in bulk conditions and by measuring its mass it is then possible to calculate the total volume occupied by the helium molecules V_{He}. The absolute density, also known as the true density, can now be calculated as the mass of the adsorbent over the volume it occupies excluding its – accessible - pore space ($V_T - V_{He}$).

2.1.2.1. Surface area characterisation

Depending on the choice of adsorbate, information about the porosity, pore size distribution, porous connectivity, surface chemistry, and surface area can be obtained from adsorption isotherms (Rouquerol et al. 1999). Details on adsorption and adsorption isotherms are provided in Chapter 3, but the following section concentrates on the BET isotherm, which provides the means to calculate the surface area of an adsorbent.

The BET isotherm, which is based on the Langmuir approach, takes the following form,

$$\frac{P}{N\left(P_o - P\right)} = \frac{1}{v_m c^*} + \frac{c^* - 1}{v_m c^*}\left(\frac{P}{P_o}\right) \quad \textbf{(2-1)}$$

Where N is the adsorbed amount, P is the pressure point, P_o is the saturation pressure of the bulk adsorbate at the adsorption temperature, and v_m and c^* are fitting parameters. It is used for nitrogen adsorption under subcritical conditions (temperatures below the critical temperature of the confined fluid) and it remains the most important tool for measuring the surface area of adsorbents (Yang 1997). In this model it is assumed that each surface site can adsorb an infinite number of non-mobile adsorbate molecules (infinite layers), where for each layer at equilibrium the rate of evaporation from covered sites and condensation on empty sites is the same. More importantly, the heat of adsorption (increase in enthalpy due to solid-fluid interaction near the surface) is considered for the first layer only, while beyond it the ratio of adsorption and desorption is assumed constant and the heat of adsorption is assumed equal to the heat of condensation.

Determining the surface area using the BET equation involves measuring the experimental adsorption isotherm for nitrogen at 77 K for a range of relative pressures. Then, by plotting the left-hand side of Equation (2-1) against the relative pressure a linear fit is obtained where the slope and intercept lead to finding v_m and c. Because the molecular area of nitrogen is known (16.2 $Å^2$) the surface area can be calculated from v_m by means of Equation (2-2). In it, s is the adsorption cross-section of the adsorbate, M is the mass of the adsorbent, N_{av} is the Avogadro's number and υ is the molar volume of the adsorbate (note that v_m has units of volume).

$$S_{BET} = \frac{v_m N_{av} s}{\upsilon M} \quad \textbf{(2-2)}$$

2.1.3. SBA-2 experimental characterisation

SBA-2 is a regular caged mesoporous material (Huo et al. 1995). It has $P6_3/mmc$ symmetry, and results from the hexagonal close packing of spherical surfactant micelles. XRD patterns support this description plus indicates a unit cell parameter ratio (*c/a)* in between 1.61 and 1.63 (Huo et al. 1996) consistent with the theoretical hexagonal close-packed (hcp) unit cell ratio of c/a=1.633.

Close packing of a spherical system is the densest arrangement of spheres in an infinite and regular lattice. There are two lattices that provide a close packing of spheres: the face-centred cubic (fcc) – also known as cubic close packed - and the hexagonal close packed (hcp). The latter, shown by SBA-2, has a coordination number of 12 (each sphere has 12 neighbours) and an atomic packing factor (APF) of 0.74048 [which is the greatest fraction of space occupied by spheres i.e. the highest sphere density]. The hcp lattice is constructed by placing two sheets of spheres arranged at the vertices of a triangular tiling one upon another in a sequence A-B-A-B-… where layer B is slightly staggered with respect to layer A since its spheres are placed directly on top of the gaps left by the spheres touching in layer A (Figure 2-3).

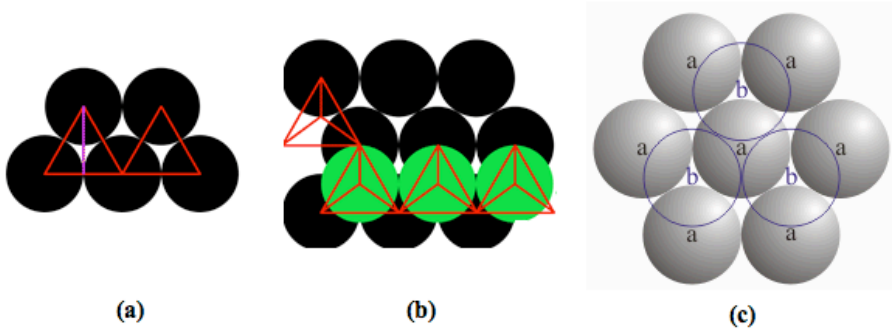

Figure 2-3: Construction of the hcp lattice: (a) Row by row assembly of layer A; (b) Making of layer B on top of layer A; (c) The final HCP stacking of spheres.

The hcp structure is better understood by studying Figure 2-3. In it, layer A is created by: (a) forming a row of spheres touching each other (centres at $[r+2nr,y,z]$ with n a positive integer); (b) then adding a second row with centres arranged as

above but with the initial coordinate shifted to where two spheres touch in the row below; and (c) repeating the process back and forward. This allows the spheres to stack close to each other, in fact, as each sphere touches another two, their centres form an equilateral triangle with sides *2r* which means the shift in the *y* coordinate between rows is $\sqrt{3}r$. As for layer B, it starts by placing a sphere touching three spheres of the layer A below. The four spheres touch so that their centres form a regular tetrahedron of side *2r*, which means the plane difference between layers A and B is $\sqrt{6}r\left(2/3\right)$. The rows of spheres in layer B are created just as those for layer A.

For every sphere present there are three gaps: one surrounded by six spheres (octahedral interstice) and two surrounded by four spheres (tetrahedral interstices). Using their geometry it is possible to work out that for spheres of $r = 1$ the distance from the centre of the spheres to the centre of the interstices is $\sqrt{3}/\sqrt{2}$ for a tetrahedral one and $\sqrt{2}$ for the octahedrals. For mesoporous materials such as SBA-2, the spheres represent the empty spaces (pores) while the interstices are the fraction of the total volume where the silica framework develops.

As for MCM-41, using surfactants with different chain-lengths leads to different unit cell and pore sizes. Huo and co-workers (Huo et al. 1995) report producing SBA-2 with cell sizes from $c = 77$ Å (with surfactant: $C_{12\text{-}3\text{-}1}$) to 102 Å (using the surfactant $C_{18\text{-}3\text{-}1}$). They also report a BET surface area of 609 m^2/g for a sample with unit cell $a = 63.8$ Å and $c = 103.4$ Å, which has a very narrow pore size distribution around 35 Å.

The nitrogen isotherm of this material is found to be consistent with a IUPAC type IV (as it will be shown in Chapter 3), from which it is inferred that SBA-2 consists either of bottle-shaped pores or a network of pores. Indeed, Zhou and co-workers (Zhou et al. 1998) determined that SBA-2 consists of a pore network where the main cavities are connected through 'channels'. In that work SBA-2 samples with unit cell size of $a = 55.5$ Å and $c = 91.4$ Å where produced (as-synthesised), which after calcination contracted to $a = 49.0$ Å and $c = 80.4$ Å. Once again, the ratio of *c/a*

for these materials (1.65 and 1.64 respectively) proved close to the theoretical ratio expected in perfect hexagonal close packing (about 1.63), the resulting pores were estimated to have a diameter of about 40 Å.

The mentioned work of Zhou and co-workers (Zhou et al. 1998) deserves further comment since they go deeper into the description of the connectivity of the pores. Using HRTEM (high-resolution transmission electron microscopy) images they identify two paths of connecting channels: one path along the *c* axis connecting A and B layers in zigzag and another straight-path connecting pores in the same layer (either A or B). Therefore, it is suggested that SBA-2 has a two-dimensional (2D) network of pores consisting of spherical cages joined by MCM-41 like channels depicting corrugated sheets that are not cross connected (see Figure 2-4).

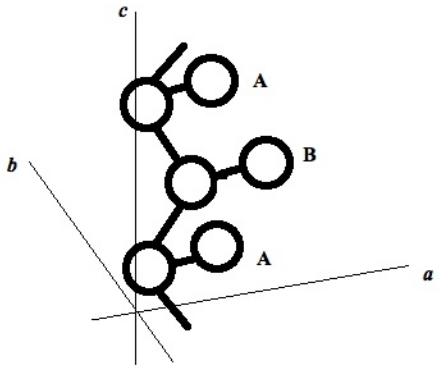

Figure 2-4: Diagram showing the proposed connected network of pores in SBA-2 (Zhou et al. 1998) Zigzag channels connect layers A and B in the c direction while straight channels connect pores in either A and B layers.

2.1.4. STAC-1 experimental characterisation

While preparing SBA-2 it is possible that the final structure of the material will present irregularities. Furthermore, it has been reported (Zhou et al. 1998) that a structure with different properties than those of SBA-2 can be synthesised while trying to obtain this material. This structure was named STAC-1 (St. Andrews-Cambridge 1).

STAC-1 was found in regions of space within the synthesised SBA-2 where the stacking sequence "A-B-A-B…" was replaced by an "A-B-C-A-B-C…" layering consistent with that of a face-centred cubic (or cubic close packing, ccp) of spheres. While both structures are composed of stacked hexagonal layers, have the same type and number of interstitial sites, the same packing efficiency (ergo, the same density), and the same coordination number (12), it is the presence of a third staggered layer (C) that introduces changes in their symmetry (Figure 2-5). The symmetry for a ccp structure is $Fm\bar{3}m$ rather than the $P6_3/mmc$ for hcp, and that simply implies that there is an additional plane of symmetry obtained by rotating the structure about the vertical space diagonal of a cubic unit-cell.

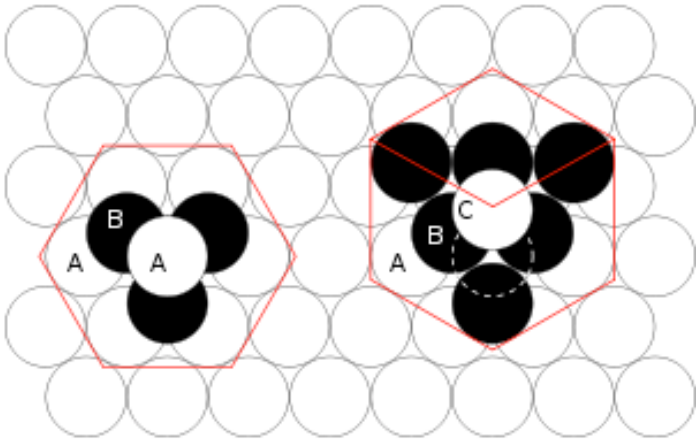

Figure 2-5: Illustration of hcp vs. ccp.

One important fact is that the cubic and hexagonal lattices are very close in terms of energy (which means that they both minimise the energy of the system, and those minimum energies are close to each other). This implies it is difficult to predict which form of packing may be predominant in a given system. Even when studying transitions in metals it is found that the ccp and hcp energies, from the density states curves including the d-orbitals, are comparable and whether one configuration is more stable than the other depends on other features of the system [(Blanc and et al. 1996), (Bera and Manna 2006), (Lanza and Minichino 2009)].

For STAC-1 it has been reported (Zhou et al. 1998) that the connectivity between pores occurs as depicted in Figure 2-6(b), according to which 2D sheets of pores are

connected through a double system of straight channels rather than straight and zigzag channels as depicted in Figure 2-6(a) for SBA-2. This network of strictly straight connections is not possible in SBA-2 due to its hcp packing of spherical layers, and it is said it may be an advantage since the straight channels are less tortuous allowing for faster diffusion of large molecules, which is an attractive quality for a catalyst support.

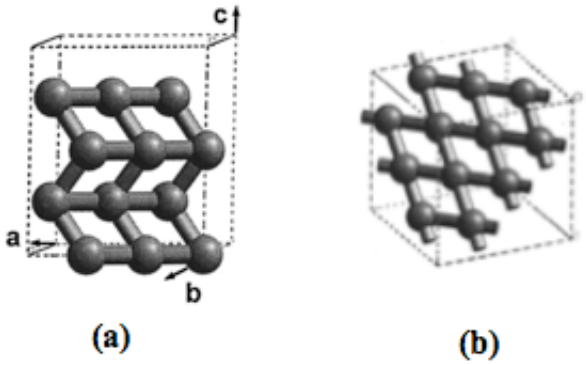

Figure 2-6: Comparison between the pore connections in (a) SBA-2 and (b) STAC-1 as reported in (Zhou et al. 1998).

2.1.5. A note on spherical-packing

To conclude this section, it has to be mentioned that there is a third possible lattice to stack spheres: the body centred cubic (bcc). The representation for this lattice is easier to visualize (Figure 2-7) since it has a sphere in the centre of a cubic unit cell which touches eight spheres situated at the corners of such cube. In this case the coordination number is 8 and the packing efficiency is about 68 %, lower than in either ccp or hcp, and though this is a lattice common in metals, it has not been found while synthesizing SBA-2 mesoporous materials which seems to imply that this packing geometry is not as stable as the other two for these systems.

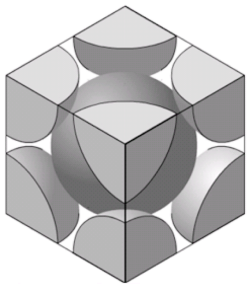

Figure 2-7: Body centred cubic structure.

Examples regarding the ccp vs. hcp packing competition include hexagonal crystals of C_{70}, which have shown interweaving bands of both packing sequences (Blanc and et al. 1996) separated by stacking faults. There, at room temperature, it is said the hcp sequence transforms into ccp indicating the higher stability of the latter – the reverse transformation was not obtained. Another example is polytype solids – those formed by identical layers differing only in the stacking orientation – as titanium-zirconium (Bera and Manna 2006) and Zn. For these materials, there is interest in understanding how its hcp structure transforms into ccp under the influence of external stress (i.e. annealing). Argon clusters also show a mixed ccp/hcp structure (Lanza and Minichino 2009) with random, non-preferential, packed regions.

As for the reason behind the presence of both ccp and hcp structures intermingled in solid crystals (Varn, Canright and Crutchfield 2002) some theories have been proposed (i.e. the fault model), but for the same phenomena in the synthesis product of SBA-2, as reported by Zhou (Zhou et al. 1998) no explanation has been put forward. For other mesoporous silicas (AMS) it has been reported (Atluri, Hedin and Garcia-Bennett 2008) that the formation of 'phase-pure' mesoporous structures depends on the synthesis conditions and a two phase transition (cubic to hexagonal and vice versa) may be induced by their hydrothermal treatment at 100°C.

Thus, in the synthesis of SBA-2 it is possible that the hcp/ccp competition results from a combination of: (a) the stacking energies of both systems being similar due to their equal stacking efficiency and (b) the random occurrence of stacking faults.

Nonetheless this is not proven in this work, and doing so would require simulating systems with large numbers of atoms and micelles that at present are not viable due to computational costs and time constrains. Also, experimentally there has been no mention on whether specific synthesis conditions can favour one stacking sequence over the other [as it was seen for C_{70} crystals (Blanc and et al. 1996), where temperature is of great importance].

2.2. The kMC technique

2.2.1. Metropolis Monte Carlo

Monte Carlo is, in its simplest description, an integration method based on random sampling. That means that instead of integrating Equation (2-3) in the conventional way (using predetermined values on the abscissa), it is done by evaluating random *x* values selected from a uniform distribution in the interval [*a,b*], which on the right hand side of Equation (2-3) is expressed as the unweighted average of *F(x)* indicated by the chevrons (Frenkel and Smit 2001).

$$I = \int_a^b dx F(x) = (b-a)\langle F(x)\rangle \qquad \textbf{(2-3)}$$

While using this procedure it is important to keep in mind that the more random numbers are selected for evaluating the function the more accurate will be the evaluation of the integral above. However, absolute integrals in statistical mechanics would require a very large number of evaluations, which make this simple approach unpractical.

In classical statistical mechanics the quantity that encodes the properties of a system in thermodynamic equilibrium is called a *partition function*, which is shown in its most general form by Equation (2-4). In that equation, the Hamiltonian $H_{(r^N p^N)}$ is a function that expresses the total energy of the system (potential plus kinetic

energy) related to the coordinates r and momenta p of its particles N; T is the temperature of the system and k_b is the Boltzmann constant - see Equation (2-7).

$$Q = c \int dp^N dr^N \exp\left[-\left(\frac{1}{\kappa_b T} \right) \mathrm{H}_{(r^N p^N)} \right] \quad \textbf{(2-4)}$$

The partition function is shaped according to the ensemble representing the system under study. An ensemble is a – mental – collection of a very large number of configurations, where a configuration can be seen as a 'picture' depicting the positions of the molecules in the system at any moment. Each configuration is a microscopic representation of the thermodynamic (macroscopic) system being studied.

Regardless of the system being studied the Boltzmann factor (the exponential term in Equation (2-4)) determines the contribution of a selected point to the overall value of the integral, and as it happens there are many points where this contribution is negligible. It is clear then that sampling points uniformly is not the most efficient way to evaluate the partition function, specially since it is a system of N particles where the larger the number of particles the greater the number of points that need to be evaluated to achieve an accurate result.

Because of the reasons stated above, and because absolute integrals in multidimensional configuration space cannot be computed, a method is needed to allow the calculation of statistical averages by sampling only the part of the configurational space (the space of possible positions for the molecules within a system) relevant to the partition function: an importance sampling method.

Among the importance sampling methods, the Metropolis algorithm is probably the best known and consists of obtaining a sequence of random samples from a probability distribution, for which direct sampling is difficult, based on a Markov chain of events. It is founded on the fact that, although absolute integrals such as $\int \exp\left[-\beta U_{(r^N)} \right] dr^N$ cannot be computed, it is possible to calculate a ratio of integrals as

seen in Equation (2-5) common in statistical mechanics (where $\langle A \rangle$ represents the statistical average of a property *A*, and *U* is the potential energy of the system).

$$\langle A \rangle = \frac{\int A_{(r^N)} \exp\left[-\beta U_{(r^N)}\right] dr^N}{\int \exp\left[-\beta U_{(r^N)}\right] dr^N} \quad \textbf{(2-5)}$$

To better explain this point let us analyse Equation (2-5). Its denominator is the absolute probability of visiting different points in space (therefore it is called the configurational part), and from now on it will be called Z. By close inspection of Equation (2-5) it is possible to identify the probability density of finding the system in a configuration r^N - Equation (2-6).

$$\wp_{(r^N)} = \frac{\exp\left[-\beta U_{(r^N)}\right]}{Z} \quad \textbf{(2-6)}$$

The upper part on the equation above is called the relative probability (or Boltzmann factor) and, unlike Z, it can be computed. Interpretation of statistical mechanics in relation to the fundamental macroscopic thermodynamic equations allows deriving the relation in Equation (2-7) (Frenkel and Smit 2001), where k_b is called the Boltzmann constant and relates the energy at the particle level with the temperature observed for the bulk system. The Boltzmann constant can be obtained by dividing the gas constant (R) by the Avogadro number (N_A=6.022141×10^{23} mol^{-1}) and is therefore a direct bridge between microscopic and macroscopic physics.

$$\beta = \frac{1}{k_b T} \quad \textbf{(2-7)}$$

$$k_b = 1.380658 x 10^{-23} J/K$$

The calculation of Equation (2-6) is not straightforward. Having the absolute probability Z in the denominator is inconvenient and therefore a means to bypass this calculation is necessary, which is the key to the Metropolis algorithm. The idea is as follows:

1. Define an old system configuration 'o', which has a non-zero Boltzmann factor
2. Define a new system configuration 'n', also with a non-zero Boltzmann factor, displaced a ΔU from the old system
3. A transition probability from the old configuration to the new one can then be defined as $\pi(o \rightarrow n)$
4. A criterion has to be established to accept or reject the proposed transition from the original configuration to the new one
5. If the new configuration is rejected, then the system reverts to the old configuration, otherwise the new configuration becomes the new link in the Markov chain

The important steps in the Metropolis algorithm are the 'trial' moves (from the old configuration to the new one) and the decision on whether to accept the trial or not. The underlying matrix of a Markov chain α is the transition matrix that determines the probability to perform a trial move from 'o' to 'n', which basically means that the total probability of moving between configurations can be expressed in terms of Equation (2-8).

$$\pi(o \rightarrow n) = \alpha(o \rightarrow n) \times acc(o \rightarrow n) \quad \textbf{(2-8)}$$

The acceptance probability, Equation (2-10), is calculated by choosing a symmetric Markov matrix α(o➔n)=α(n➔o) so that the transition probability satisfies Equation (2-9). Where $\wp$ is a distribution denoting the probability of being in a given configuration.

$$\wp(o) \times \pi(o \to n) = \wp(n) \times \pi(n \to o) \tag{2-9}$$

$$acc(o \to n) = \begin{cases} 1 & if \quad \wp(n) \geq \wp(o) \\ \dfrac{\wp(n)}{\wp(o)} & if \quad \wp(n) < \wp(o) \end{cases} \tag{2-10}$$

As was mentioned before, the partition function has different shapes according to the ensemble being studied and because the probability density is directly related to the partition function, the acceptance criteria will also be ensemble-specific. Of relevance to this chapter is the *canonical ensemble*, also known as a *NVT* system that has a constant number of molecules *N*, constant volume *V*, and constant temperature *T*. It can be defined as a closed system of molecules confined in box of known volume in contact with a heat bath large enough to maintain the temperature in the system invariable.

The partition function for the canonical ensemble is presented in Equation (2-11), where Λ is known as the thermal de Broglie wavelength – Equation (2-12) - and is a function of the temperature *T* and the mass of the gas particles *m*, *h* being Planck's constant (h=6.626068×10^{-34} J•s). In the canonical ensemble the system under study only exchanges energy with its surroundings via a very weak contact with the thermal bath. This is important because it means that the energy conserved in the system is no longer fixed (as would be for a fully isolated system) but rather submitted to small variations that, after a sufficiently long time, equilibrate the system with its surroundings.

$$Q_{(N,V,T)} \equiv \frac{1}{\Lambda^{3N} N!} \int dr^N \exp\left[-\beta U_{(r^N)}\right] \tag{2-11}$$

$$\Lambda = \sqrt{\frac{h^2}{2\pi m k_B T}} \tag{2-12}$$

From Equation (2-11) it is easy to see that Equation (2-13) represents the probability density for this ensemble since the canonical ensemble has a fixed number of molecules. Then, the only changes in configurations can come from those

molecules changing positions within the known volume. Equation (2-14) presents the acceptance criteria for this trial.

$$\mathrm{N}_{\left(r^N\right)} \propto \exp\left[-\beta U_{\left(r^N\right)}\right] \tag{2-13}$$

$$acc(o \rightarrow n) = \min\left\{1, \exp\left[-\beta\left(U_{(n)} - U_{(o)}\right)\right]\right\} \tag{2-14}$$

From the acceptance criteria it can be seen that those configurations that minimise the energy in the system are favoured, as expected due to the principle of minimum energy, which is derived from the second law of thermodynamics. The internal energy of a close system will decrease and approach a minimum value at equilibrium. In terms of the simulations, Equation (2-14) means that a random number in the interval (0,1) has to be generated and compared to the Boltzmann factor: if the random number is lower or equal to it then the new configuration is accepted, otherwise the old configuration is kept.

2.2.2. The kMC algorithm

The name kinetic Monte Carlo has had different meanings in the past, and in general it is used in reference to a method that is capable of studying dynamically evolving systems from state to state. It originated in the 1960s in the study of radiation damage annealing and since then it has been further developed and applied to other areas like surface adsorption, diffusion and growth (Voter 2005). Though in theory kMC can give the exact dynamic evolution of a system, this is very unlikely and hardly ever attempted.

Transient systems, those evolving with time, are mainly studied by means of molecular dynamics (MD), where variations in the positions and velocities of the molecules for very small time intervals (~10^{-15} s) are studied using the classical equations of motion. Integration of those equations in time is computationally expensive, which is why MD is only a viable tool to study small time-scale problems

(~10^{-6} s). However, for a chosen interatomic potential and boundary conditions, MD gives a close representation of the dynamical evolution of the system. The time limitation is nonetheless very important since many processes take place on greater time scales than just a microsecond. kMC originated as a mean to overcome the MD time constraint, its applications include: chemical vapour deposition (Kalke and Baxter 2001, Battaile 2008, Battaile and Srolovitz 2002), vacancy diffusion, grain growth (Battaile 2008),and heterogeneous catalysis (Reuter and Scheffler 2006) among others.

As it was originally conceived, kinetic Monte Carlo assumes that the long-time dynamics of the evolving system consist of 'diffusive jumps from state to state' (Voter 2005); in other words, instead of following the trajectory of every molecule through time, kMC relies on occasional transitions being able to characterise the dynamics of the system through infrequent-events. This means that in kMC after a new trial *i* is attempted the new state *i* can only be achieved after the system has been allowed to relax: the energy must be minimised (either by steepest descent or conjugate gradient algorithms) permitting the system to reach a configuration in which the total forces on every atom are zero. In other words, a *state* in kMC is a locally stable configuration impervious to small vibrations that may affect the system.

As opposed to a standard Monte Carlo simulation, kMC does not strictly obey microscopic reversibility (equal probabilities of moving from configuration *i* to *j*) for each trial though it does from state to state. This is expected and is related to a property of infrequent-event systems: since the system is trapped in a state-basin for a long time (relative to vibrational periods) it has no memory on how it got there which is a defining property of a Markov chain.

kMC allows to relate the evolution of the process to a physical time-step, but to do that it is necessary to know in advance the rates of all possible events (usually obtained through MD simulations) (Kratzer 2009); in fact, if these rates were known accurately, the state-to-state trajectory generated this way would be identical to a MD

trajectory. That is not an easy task, and the kMC method applied in this thesis to mimic the synthesis of periodic mesoporous silicas SBA-2 and STAC-1 is based on that developed by Schumacher and co-workers (Schumacher et al. 2006b) that aims to study the final outcome of the simulation rather than the precise kinetics of the synthesis. Therefore, we are not tying the kMC to a physical time-evolution – and so, the rates of the possible events are not researched beforehand.

2.2.3. Simplifications

Despite the advantages presented by the kMC technique over MD in terms of speed, a complete simulation of the synthesis of amorphous mesoporous silica (which in real time takes from a few hours up to a few days) using a full description of the substances involved would still be computationally very expensive. To make the simulations viable, a few simplifications are put in place that do not affect the overall result of the simulations. These simplifications were first introduced by Schumacher and co-workers (Schumacher et al. 2006b) and can be enumerated as follows:

- Hydrogen atoms are not explicitly accounted for in the simulations
- Water molecules are not represented explicitly
- No electrostatic interactions are taken into account
- The surfactants are not present, but rather a geometric representation of the micelle shape to which a soft attractive potential is given
- The silicon atoms do not contribute to the potential energy.

At pH above eleven a large percentage of the silanol groups are deprotonated (Wu and Deem 2002). The justification to not account for the Si interactions in the system arises from the way the simulations take place. During the entire simulation the Si atoms are fully coordinated, that is to say they are fully surrounded by oxygen atoms and so, it is them who make the most contribution to the potential energy rendering any Si contribution – other than that arising from Si-O bonds - negligible

in comparison, as commonly assumed in zeolite simulations (Bezus et al. 1978) (Yun et al. 2002).

Although the absence of water molecules and electrostatic interactions may seem a harsh simplification, and certainly means that the reaction path followed may differ from the actual experimental reaction path, it has been proved by previous studies (Schumacher et al. 2006b) that the final model configuration obtained this way is a realistic representation of the real material; therefore these simplifications were also used within this research.

2.2.4. Steps for kMC technique implementation

In order to simulate the synthesis of amorphous silicas along the entire process, from silica aggregation around micelles up to calcination, it is necessary to model the interactions using realistic force fields that are simple enough to avoid excessively large computational times.

The kMC technique is in essence an internal energy minimisation process of a system defined by a number of molecules, a known volume, and a fixed 'simulated' temperature that is not necessarily equal to the experimental temperature of the process. The acceptance criterion is presented by Equation (2-15).

$$acc(o \rightarrow n) = \min\left\{1, \exp\left[-\beta\left(U_{(n)} - U_{(o)}\right)\right]\right\} \quad \textbf{(2-15)}$$

The kMC technique as applied in this thesis consists of the following trials: shaking, condensation, hydrolysis, and swapping, all of which are independently explained below. After each trial a deterministic minimisation of the network energy takes place, computed through the steepest descent method for a minimum of 50,000 steps. The kMC trials described next are consistent with those used by Schumacher

and co-workers in the simulation of the synthesis of MCM-41 (Schumacher et al. 2006b), which is why they are only briefly described here.

2.2.4.1. Shaking

This trial introduces a disturbance on the system displacing every atom by a fixed distance (set to 1.6 Å) in any direction. The idea is to compensate for the minimisation process used, which might lead the system to get trapped into metastable states for too long preventing its evolution towards more stable configurations. This introduces stresses in the different bonds present as well as creating disturbances in non-covalent and micelle-atom interactions that, followed by minimisation, will help the system overcome energy barriers that might otherwise be a serious drawback of the kMC technique in modelling the synthesis of PMS.

2.2.4.2. Condensation: bond formation

During this trial two monomers are bonded. Once a condensation pair (two non-bonding oxygens) is chosen one Si-O bond is broken while the remaining oxygen forms the Si-O-Si bridge. The exact reaction mechanism through which silica monomers polymerise is not fully represented. Such mechanism would require for the silica monomers to be temporarily penta-coordinated in the course of the reaction (Garofalini and Martin 1994) whereas during the kMC simulations the silicon atoms are always fully coordinated (silica monomers are always represented as SiO_4^{-4}).

For a condensation trial to be allowed a cut-off distance of 4 Å was set, so that any two non-bonding oxygens closer than that are eligible to bridge the two monomers to which they belong – a reversible reaction depicted in Equation (2-16). The cut-off distance was taken from a previous work on MCM-41, where it was proven it was the right choice to yield a reasonable acceptance probability while respecting microscopic reversibility.

$$H_4SiO_4 + H_4SiO_4 \leftrightarrows H_6Si_2O_7 + H_2O \quad \textbf{(2-16)}$$

The energy of the reaction is -13.4 kJ/mol as it was used for the previous MCM-41 kMC simulations, a number found through quantum mechanical calculations of the polymerisation of silicic acid in an aqueous environment (Catlow et al. 1997). Although for MCM-41 it was assumed that water quickly diffuses out of the evolving silica structure – which allowed removing the unbound oxygen generated after reaction – in simulations for SBA-2 and STAC-1 this assumption led to the condensation trials been rejected. It was found that the contribution of these unbound oxygens to the energy in the system helped condensation to take place.

For this reason, these oxygens were left in the simulation to interact with the other atoms, their main contribution to the system energy coming from non-covalent repulsion to neighbouring oxygen atoms and attraction interactions to the micelles present. In a way, it can be said that the unbound oxygen represents the water molecule that is produced by the reaction.

2.2.4.3. Hydrolysis: bond breaking

This is the reverse trial to condensation. To attempt this trial, a random bridging bond is selected and replaced by two non-bonding oxygens linked to the silica monomers previously joined by the bridging oxygen, keeping the silicon atoms fully coordinated. Because this reaction consumes water [see Equation (2-16)], when this trial is attempted the closest unbound oxygen is identified and removed from the simulation.

Hydrolysis may occur at any point during the synthesis process except during calcination. When the sample reaches the calcination stage it has been thoroughly dried, and calcination takes place under the flux of a dry fluid at very high temperatures, which means there is no water available for the reverse-condensation

reaction to take place. Mimicking this, the simulated calcination steps do not allow for hydrolysis to take place.

2.2.4.4. Swapping

Swapping consists of taking two O-Si bonds belonging to two different silicon atoms that are connected by bridging oxygen and exchange them. Clearly, this move makes sense only if the two O-Si bonds are different in nature, i.e. one is non-bridging oxygen and the other one is.

This trial arises from quantum mechanical studies that indicate this is an appropriate representation of the diffusion mechanism in amorphous silica (Sarnthein, Pasquarello and Car 1995). This trial allows the evolution of the ring size in the silica network, for example transforming three-member rings into four-member rings, but even more important is that this trial has a direct impact in what will become the final topology of the pore walls.

2.2.4.5. Steepest descent minimisation

This method is a first-order algorithm to find the local minima of a function by looking at its first derivatives around a point and moving in steps proportional to their negative absolute value; Equation (2-17) represents how a new point *b* is obtained from an initial point *a* of a function *F(x)*, knowing that *F(x)* is soft and differentiable in the vicinity of point *a*. In that equation, the value of γ is a positive number, small enough to assure the accuracy of the method, yet large enough to help improve its speed.

$$b = a - \gamma \nabla F(a) \qquad \textbf{(2-17)}$$

$$\frac{F(x+s) - F(x)}{s} \qquad \textbf{(2-18)}$$

The gradient method is fully applicable in the simulations because the potential force fields are continuous and soft. The evaluation of the gradient is done numerically through finite difference approximation – Equation (2-18) is an example of this in one dimension – where the spacing s is chosen small enough (1×10^{-4} Å) to ensure the stability of the method. Steepest descent is a slow converging method, but it is effective, and it suffices for the purpose of this thesis.

No further details on the gradient method are given here because it is very well explained in the literature (Arfken 1985, Press et al. 1992), however there are a few points worth mentioning regarding its application to simulate the growth of periodic mesoporous materials. Firstly, the gradient being evaluated is nothing but the derivative of potential energy in a given direction: a force. Secondly, since it is a very large system with many atomic interactions, the general approach to applying the method involves:

- Calculating the total potential derivatives (forces) to which each atom is subjected in all directions (x, y, and z) due to the effect of the remaining atoms
- The maximum step is linked to the maximum force exerted on any of the atoms, so that each one of them is moved a fraction of the maximum step directly proportional to its force ratio with respect to the maximum force
- If the unit cell volume is allowed to vary, the total force contribution in each direction is computed and their lengths are adjusted in a similar way as described above

2.2.5. Force field

A force field is a function which given a set of parameters is capable of describing the potential energy of a system of particles. Both the functions and the

parameters are derived from quantum mechanical calculations to represent as accurately as possible real systems.

The total potential energy during the kMC simulations is calculated through Equation **(2-19)**. It shows that the potential energy in the system is the result of the Si-O bonds bending/stretching U_{bond}, the repulsion experienced by oxygen atoms U_{rep}, the micelle-oxygen interactions U_{mic}, plus –if present- the external pressure contribution U_{vol}, and finally a penalty for the cell volume deformation U_{def} (when allowed).

$$U_{tot} = U_{bond} + U_{rep} + U_{mic} + U_{vol} + U_{def} \qquad \textbf{(2-19)}$$

Each one of the contributions mentioned above are detailed in what follows, for further reading it is suggested to take a look at the work of Schumacher (Schumacher et al. 2006b) on MCM-41.

2.2.5.1. Bonds force field

The strain from the Si-O bonds is modelled through the harmonic spring potential of Tu and Tersoff (Tu and Tersoff 2000),

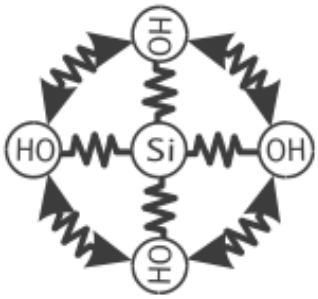

Figure 2-8: Representation of the Si-O bonds bending/stretching contributions. (Schumacher et al. 2006b).

The numerical equivalent to Figure 2-8 is presented by Equation (2-20). Parameters for the equation are presented in Table 2-1 and they are the same used by

Tu and Tersoff and later by Schumacher and co-workers for MCM-41. The sums are evaluated over the entire unit-cell, which means that all Si-O bonds are considered first and then, for each selected atom *a,* the bending stress between bonds *i* and *j* is calculated. If centred on a silica atom there are four bending stresses while at the oxygen atoms there is one contribution at the most (for bridging oxygens). In the equation, b_o is the bond length at equilibrium, and $cos\theta_{o,a}$ is the cosine of the angle centred at atom *a* at equilibrium, while k_{st} and k_{bnd} are the stretching and bending spring constants respectively.

$$U_{bond} = \frac{1}{2}\sum_{i} k_{st}\left(b_i - b_o\right)^2 + \frac{1}{2}\sum_{a}\sum_{i\neq j} k_{bnd}\left(\cos\theta_{ij} - \cos\theta_{o,a}\right)^2 \qquad \textbf{(2-20)}$$

Table 2-1: Spring force field for silicic acid monomers (Tu and Tersoff 2000).

	Equilibrium	Spring constant
Bond length	1.60 Å	$k_{st}/K_B=31.33\times10^6$ K/nm^2
Angle O-Si-O	109.47 °	$k_{bnd}/K_B=8703$ K
Angle Si-O-Si	180.00 °	$k_{bnd}/K_B=50131$ K

A final word is required in reference to the equilibrium Si-O-Si bond angle. Experimentally it is found to be around 145 ° rather than 180 ° as used in these simulations, however the latter value artificially introduces strain in small silica rings (for rings of less than 5 members) as predicted by quantum mechanical simulations for real silica, and though this affects the orientation of the non-bonded oxygens, specially for the small non-cyclic oligomers, it is unlikely to affect the final topology of the silica network (since cyclisation occurs quickly from the beginning of the simulations).

2.2.5.2. Repulsive interactions

These interactions only involve the oxygen atoms and are modelled so as to account for repulsion between close atoms. Numerically, this is approached through

a quadratic approximation – Equation (2-21) – of the repulsive part of the 12-6 Lennard-Jones (LJ) potential.

$$U_{rep} = \frac{1}{2} \sum_{\substack{a \neq b \\ r_{ab} < r_c}} k_{rep} \left(r_c - r_{ab} \right)^4 \qquad \textbf{(2-21)}$$

Following the work for MCM-41, the cut-off radius for these interactions is set at r_c = 2.80 Å while the constant is k_{rep} = 5411.48×10^6 K/nm^4. The cut-off radius ensures that even small silica rings do not suffer stress from atom-atom repulsion but only from covalent interactions within its members. For the application of kMC on MCM-41 it was found (Schumacher et al. 2006b) that applying an attractive-repulsive potential, though suitable, required much longer simulation times due to the larger cut-off required. The systems studied in this thesis are even larger (at least twice as large) than those for MCM-41, therefore using these latter type of potential was not even considered.

In order for this approximation to be valid, the cut-off radius for the attractive micelle-oxygen interactions must be large enough so that all oxygen atoms in the simulation are attracted to at least one micelle. Thus, the micelle(s) becomes responsible for pulling the system together. In a way this could be interpreted as if the attractive influence of the micelle greatly exceeds any attractive contribution from oxygen pairs.

2.2.5.3. Micelles force field

The contribution of the micelles to the energy is twofold: from micelle-oxygen interactions and from micelle-micelle repulsion,

$$U_{mic} = \sum_m \sum_O U^{MO}_{(r_{mo})} + \sum_{m_i \neq m_j} U^{MM}_{(r_{m_i m_j})} \qquad \textbf{(2-22)}$$

Micelles in this work are a geometric representation of those known to exist in the real synthesis solution. Hence, knowing that the micelles precursor to both SBA-2 and STAC-1 materials are spherical, this is the geometric shape introduced in the simulations. However, in order for this geometric shape to be a realistic representation of a real micelle its force field must be chosen carefully since the micelle has small interstices or gaps between the polar heads of the surfactants (forming the boundary of the micelles) where silicic acid monomers can penetrate whereas the spherical representation has a closed perimeter.

To address this issue, the first contribution in the equation above (micelle-oxygen interactions) requires a potential strong enough to pull the atoms towards the micelle surface but at the same time soft enough to allow them to penetrate its surface. This is accomplished, as it was done for MCM-41 (Schumacher et al. 2006b), by means of the force field described in Equation (2-23).

$$U_{(r_{mo})}^{MO} = -\varepsilon_{MO} \cdot \begin{cases} 1 - \left(\dfrac{r_{mo} - r_{\min}}{r_{null} - r_{\min}} \right)^2 & \forall r_{mo}[0, r_{join}] \\ \dfrac{(r_{cut} - r_{mo})^2}{(r_{cut} - r_{null})(r_{null} - 2r_{\min} + r_{cut})} & \forall r_{mo}[r_{join}, r_{cut}] \\ 0 & \forall r_{mo}[r_{cut}, \infty] \end{cases} \qquad \textbf{(2-23)}$$

$$r_{join} = \frac{r_{null}^2 - 2r_{\min} r_{null} + r_{\min} r_{cut}}{r_{cut} - r_{\min}}$$

This is a double-parable potential with four parameters: the minimum potential depth ε, the radius at which the micelle potential is null r_{null} (the micelle surface), the radius where the potential depth is at a minimum r_{min} and the cut-off radius r_{cut} after which the oxygen atoms no longer feel the attractive force of the micelle. The difference between the point where the potential is at a minimum and that where the micelle surface stands (r_{min}-r_{null}) provides a cushion where the silicic acid monomers can reside, and in theory the larger this difference the greater the heterogeneity of the pore surface in the final model.

The second term in Equation (2-22) refers to micelle-micelle interactions. The surfaces of the micelles in the real solution are positively charged. If we were to be rigorous then we would have to account for the charge density matching mechanism acting around each micelle, but in order to achieve results in a feasible time this level of detail is not considered and we rather focus on the long range polymerisation effect created by the presence of micelles. Thus, unless different parameters are given to different micelles, within a simulation all micelles are alike and in consequence they repel each other. Furthermore, since the unit-cell is periodic they will be interacting not only with other micelles in the simulation volume but also with those close enough within the neighbouring cells.

The micelle-micelle repulsion is calculated not from the micelles' surface but from the position of their centres and is approximated through the empirical Equation (2-24). In it, r_{min} is the sum of the minimum radius of the two micelles being considered.

$$U^{MM}_{(r_{m_i m_j})} = k\left(r_{\min} - r_{m_i m_j}\right)^2 \left(\frac{r_{\min}}{r_{m_i m_j}}\right)^{10} \qquad \textbf{(2-24)}$$

In Figure 2-9 an example of micelle-micelle repulsion with $k = 1\times10^{-20}$ J/Å and r_{min} = 30 Å is presented for different repulsion models. As can be seen, all models presented account for very weak micelle repulsions if they are scattered – nowhere near touching each other. This is a reasonable approximation since if the charge density matching mechanism takes place early in solution then each micelle will have its surface charge cancelled out by the silicic acid layers surrounding them. The inflection point at which micelles feel no repulsion is chosen as that of the ideal packing: where the minimum potential depth of the spherical micelles touch. Further compression by packing effects and the strain created by the linking of different micelle surface-layers are penalized by strong repulsions. This is to account for the fact that in the real solution the micelles are densely packed structures with the

organic tails crammed inside and whose hydrophilic heads present a strong barrier – both due to charge and steric effects – for the micelles to merge.

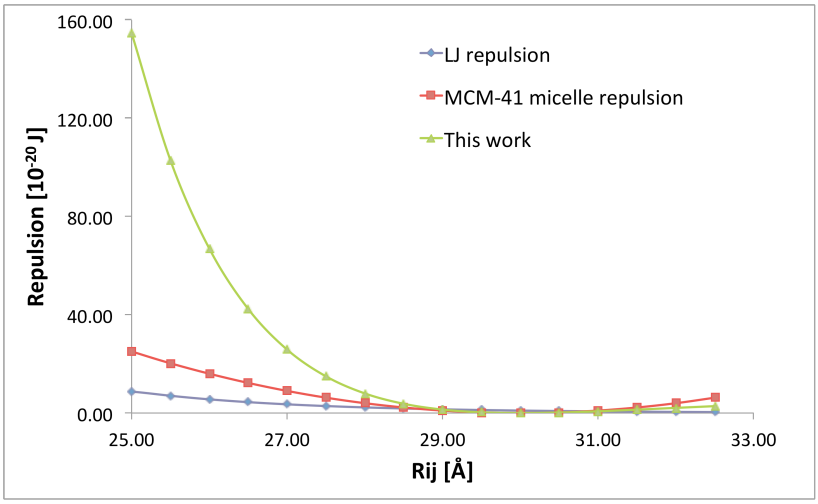

Figure 2-9: Comparison between different estimations of micelle-micelle repulsion. R_{ij} is the distance between the micelle centres.

In this work it was found that both the Lennard-Jones model and that used in a previous work for the simulation of the synthesis of MCM-41 (Schumacher et al. 2006b) are insufficient to describe the repulsion between spherical micelles for the synthesis of the studied materials, since when more than one micelles were included in the simulation cell they merged. Figure 2-9 clearly shows the great difference between the repulsion predicted by the model used in this work with respect to those mentioned above. This is likely to be linked to higher repulsion generated by the two hydrophilic heads in each surfactant molecule (Figure 2-2), although this is not a quantity that can be measured experimentally.

2.2.5.4. External pressure

The kMC simulations as derived for MCM-41 allow exerting an external pressure onto the simulation cell. This feature is used during the aggregation stage explained later in this chapter to ensure the effective packing of micelles in the system. Equation (2-25) is used to calculate the resulting energy from this contribution (Schumacher et al. 2006b), where *a*, *b*, and *c* are the lengths of the unit-cell.

$$U_{vol} = P\left[(a \times b)\cdot c - \sum_m V_m\right] \quad \textbf{(2-25)}$$

2.2.5.5. Cell-volume deformation

When simulating the amorphous silica MCM-41 it was noted that if a defect or weak region appeared on the model walls, its periodicity made it susceptible to collapsing under 'mechanical' stress. The proposed solution was to couple the axes so that their length ratio was constrained within a certain value. To that end Equations (2-26) through (2-28) are used, where the Young's modulus (E) is taken as that measured experimentally for calcined MCM-41, 3190 MPa (Schumacher et al. 2006b). This value was used in absence of an experimental value for SBA-2, and judging that both materials share a similar synthesis mechanism (in these equations σ is the tension according to Hooke's law).

$$I_1 = \sqrt{I\cdot J\cdot R_{IJ}^o} \quad \textbf{(2-26)}$$

$$J_1 = I_1 / R_{IJ}^o$$

$$\sigma = \frac{E\lambda}{n} \equiv \frac{E(I - I_1)}{nI_1} \quad \textbf{(2-27)}$$

$$U_{def}^I = \int_{I_1}^{I} \sigma A dI = \frac{1}{2}\frac{E(I - I_1)^2}{nI_1} A \quad \textbf{(2-28)}$$

In the equations above, I and J represent any axis pair. R_{IJ}^o is the desired rate around which the axis must be kept and I_1 and J_1 are the values of the axis as calculated for a non-deformed unit-cell. A is the area perpendicular to the axis where the force is applied. The total contribution to the system's energy is the sum over the entire coupling restrictions imposed (distributed evenly across n neighbouring cells).

2.3. Stages in the simulated synthesis of SBA-2 and STAC-1

In this section a step-by-step explanation of the synthesis stages being modelled through the kMC technique is given. Since the full synthesis of the materials spans several processes, from micelle formation to calcination, they have to be accounted for in the simulation. This is achieved by partitioning the simulation into stages, each one accounting for the characteristic elements of their experimental counterpart:

1- Monolayer formation around micelles.
2- Micelle aggregation and deformation.
3- First calcination stage where the micelles are still present but the temperature has already increased.
4- Second calcination stage where micelles are no longer present (equivalent to the total removal of the organic content in the experimental material).
5- Cooling where the system is slowly returned to its original temperature.

These stages are explained in depth below, from the kMC trials involved to how the transition between stages is done. The simulations were carried out in blocks of 20 accepted trials for the STAC-1 models and of 50 accepted trials for the SBA-2 models, since the latter has at least twice the number of atoms in a simulation cell – defining an accepted trial as a successful Monte Carlo move after the energy minimisation takes place.

2.3.1. Stage 1: Monolayer formation

Physically, as soon as the TEOS is hydrolyzed (which occurs almost instantaneously) the silica monomers are attracted to the surface of the micelles present in the solution. A layer of silica, that might have to some degree polymerised

forming small rings or clusters of isolated bi-units, then evenly covers the micelles boundaries.

In simulation terms a spherical model-micelle is placed in the simulation cell and immediately afterwards SiO_4^{-4} monomers are placed randomly in the empty space between the micelle surface and the edge of a sufficiently large unit cell. To mimic the experimental counterpart, condensation, swapping, and hydrolysis (since there is water in the solution permitting the reverse reaction) trials are allowed, as well as shaking. Although both condensation and hydrolysis are given the same probability of occurrence, the latter was found to have a very low acceptance rate, clearly indicating that silica polymerisation is favoured.

For the simulation of SBA-2 models it is necessary to have two micelles in the simulation cell, Figure 2-10b. This was found necessary to mimic the hcp packing of the real material.

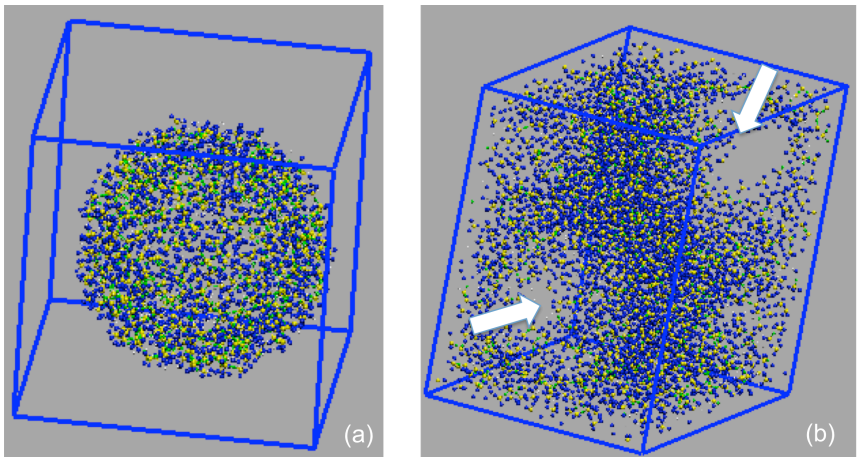

Figure 2-10: (a) silica layer formation on STAC-1 model-micelle; (b) initial system for SBA-2 with the two micelles indicated by white arrows. Yellow indicates Si atoms, while green and blue mark bonded and non-bonded oxygens respectively.

Besides the number of micelles in the simulation cell, the other factor directly affecting the final symmetry of the model materials is the shape of the simulation cell. To achieve the hcp symmetry exhibited by SBA-2 materials, the simulation cell is set with both *x* and *y* axes perpendicular to *z* while the angle between *x* and *y* is 60

° (hexagonal cell). The axes are given an initial length in the range presented earlier in section (2.1.3) as referenced in the literature (Huo et al. 1995). For SBA-2 the shape of the simulation cell is then already imposed, and so it is also allowed to vary its volume using the coupling energy penalty (explained in section 2.2.5.5) to keep the ratio between *a* and *c* close to 0.63, as is expected for a hcp structure. This forces the simulation into keeping the centre of the two micelles staggered, representing the A and B layers or the hcp structure, since at this point the periodic images of the micelles have not been introduced.

The ccp symmetry for STAC-1 is achieved not only by using a different number of micelles (one, as shown in Figure 2-10a) in the simulation cell but also by imposing it a different shape (triclinic). However, the combination of the micelle size with the simulation cell shape for this material leaves a reduced space for monomers to be inserted, which is why to facilitate the placing of silica monomers at this stage by providing them with more accessible volume a simple cubic shape is imposed on the simulation cell. This means that the correct shape must then be introduced in the next stage of the simulation.

A visual inspection indicating that a silica monolayer has covered the surface of the micelle(s), supported by a low percentage of isolated monomers (Q_o lower than 10 % for STAC-1 models and lower than 40 % for SBA-2 models), is used as an indication that this stage of the simulation has finished, and the next synthesis stage involving micelle aggregation must be initialized. The percentage of isolated monomers is not meant to be an accurate representation, but rather to ensure that the silica polymerisation is well underway, and more isolated monomers are allowed for the SBA-2 model to keep the cross-linking between the layers surrounding the two micelles in the simulation cell to a minimum, as this phenomena is to be modelled in the next stage.

2.3.2. Stage 2: Micelle aggregation and deformation

In this section, the main symmetries of the systems are imposed and interactions between the micelle(s) present in the unit-cell and those in the surrounding periodical images are initialized. Also, a small external pressure is applied on the unit-cell that ensures micelles will aggregate and their surrounding silica layers will start cross-linking.

The STAC-1 simulation cell is changed to rhombohedra (see Figure 2-11), with all the angles between axes set to 60 °. The axis lengths are now allowed to vary without imposing energy penalties. These are not needed here because the shape of the simulation cell suffices to assure the ccp ABCABC… layering is achieved upon periodicity.

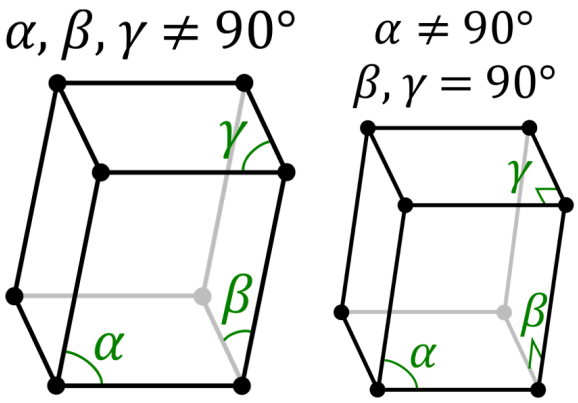

Figure 2-11: Comparison between the unit-cell shapes for STAC-1 (left, triclinic - rhombohedra) and SBA-2 (right, hexagonal, since a≠c).

Allowing the micelle(s) in the unit cell to 'see' those in the periodic images and applying a small external force (pressure, 200 bar) to the unit-cell are the main features enforcing the aggregation of the micelles and forcing the cross-linking of the silica layers so that they evolve into the final silica network holding the system together. As micelles aggregate, they are also allowed to deform (its null-radius varies) due to the strain they feel as the silica network evolves.

As the micelle(s) deform, an expected initial increase in the micelle size is observed. The increased surface area that it provides maximises the micelle interaction with the silica structure and, in doing so, minimises the energy of the system. However, it is clear that the system reaches a point where the strain posed by the silica structure on the micelle balances the initial expansion and starts contracting the micelle towards its original size. In the vast majority of the simulations the final micelle radius is within its original size (±3 Å).

As it can be seen in Figure 2-12, after the micelle aggregation and deformation has taken place the systems are compact. The radius of the micelles might exceed the unit-cell axis, which is why there are empty spaces on the simulation boxes that, at this point, are no indication of connection between micelles but rather prove of the increasing density of the silica structure surrounding them.

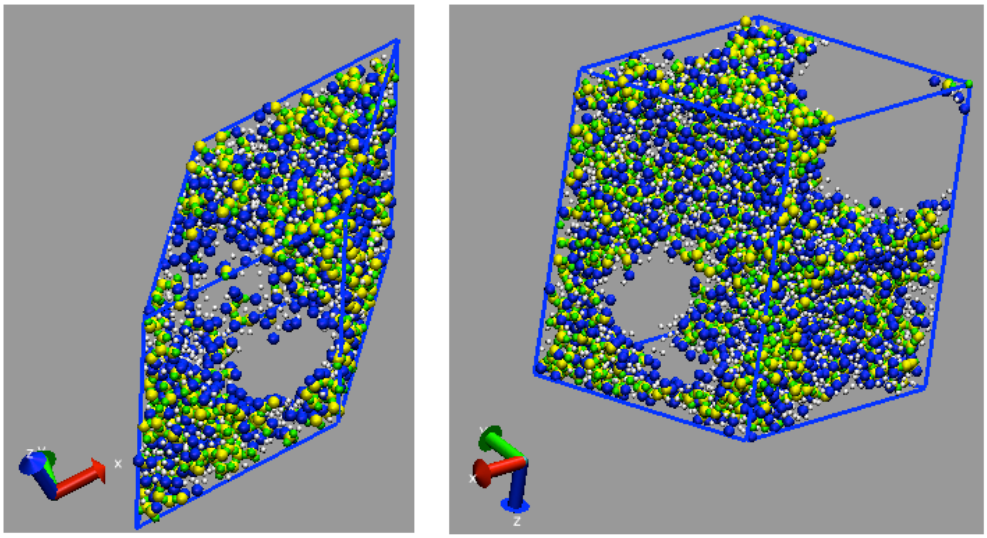

Figure 2-12: On the left is the triclinic unit-cell for the STAC-1 models while on the right is the SBA-2 model, both after micelle aggregation and deformation has taken place. The white dots represent unbound oxygens arising from the polymerisation of the silica, and they can be seen sitting near the micelle-silica interface.

The aggregation and deformation is ended once (1) the ratio between bond formation and bond breaking has equilibrated, and (2) the micelle radius has reached an approximated equilibration (its rate of change is slow). This means the silica

network is stable and only minor local strain corrections are occurring at the current temperature.

2.3.3. Stage 3: First calcination stage

This stage represents the material being dried by the increased temperature. The micelle is still present and the unit-cell and micelle radius are still variable, but all unbound oxygens (derived from silica condensation) are removed. Experimentally, due to the high temperatures provided by a pure dry gas, any water produced by the formation of further bonds immediately leaves the system. To account for this in the simulations, unbound oxygens are withdrawn as soon as a condensation trial takes place and, because water is needed for hydrolysis to take place, bond breaking is no longer allowed as a simulation trial.

The unit-cell density at the beginning of this step is unbalanced due to the amount of material that was withdrawn. The system then seeks a balance by contracting the unit-cell, which in turn affects the micelle radius (it also contracts).

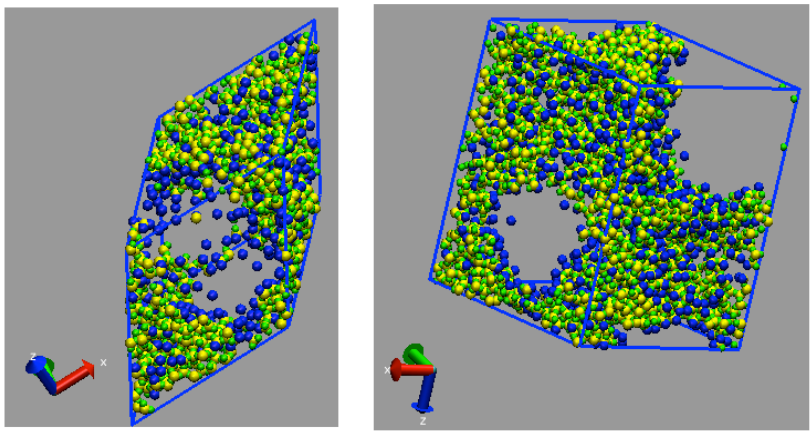

Figure 2-13: Example configuration of STAC-1 and SBA-2 models (left and right respectively) after stage 3 is completed.

This stage of the simulations ends arbitrarily once the condensation acceptance ratio is very low (less that 10 % of trials are accepted) and the micelle radius is close to that of the desired pore-size. The degree of polymerisation at this point typically

shows comparable Q_3 and Q_4 percentages, all the silica has polymerised to some degree (Q_o is zero), and the percentages of Q_1 and Q_2 add up to less than 10 % of the total silica present.

2.3.4. Stage 4: Second calcination stage

At some point during the experimental calcination of the material the contents of the micelles have been completely removed. This is mimicked by this stage, by removing the model micelle(s) and any interaction derived from it (them).

The energy penalty due to cell deformation is now introduced for the STAC-1 models to avoid the pores from collapsing due to structural defects enhanced by periodicity (Schumacher et al. 2006b). However, after a simulation ran without introducing this axes-coupling condition lead to a realistic model pore, it was concluded that this restriction is not necessary when simulating STAC-1.

It is relatively straightforward to identify the end of this stage since both the bond formation and the bond swapping trials are accepted less than 5 % of the time. In general, after this stage all models present a percentage of fully polymerised silica Q_4 larger than Q_3. Also, the until cell contraction after both calcination stages compares well to experimental observations where a contraction of about 33 % is detected on SBA-2 unit-cells (Hunter and Wright 2001). In the simulations the unit-cell contraction was 27.5 % on average, ranging from 21 % (for models STAC-1^J and STAC-1^O) up to 38 % (for STAC-1^G). Also, the average micelle contraction was about 2-3 Å.

2.3.5. Stage 5: Cooling

This stage relates to the part of the synthesis where the material cools down after calcination at ambient temperature. In simulation terms, the system is allowed to relax stepwise (every 100 K), from the high calcination temperature (800 K) to that prior to calcination (300 K). During this process the model undergoes minor adjustments to its structure leading to a configuration with a lower energy than that at the end of the previous stage.

The cooling process is gradual, which is why it is simulated by decreasing the temperature on a ramp, 100 K every ten blocks of trials until returning to the initial simulation temperature. Overall, it was observed that no major changes to the silica structure occurred during this stage with acceptance ratios for bond forming and bond swapping being less than 1 %, which also confirms the stability of the structure obtained at the end of the calcination stage.

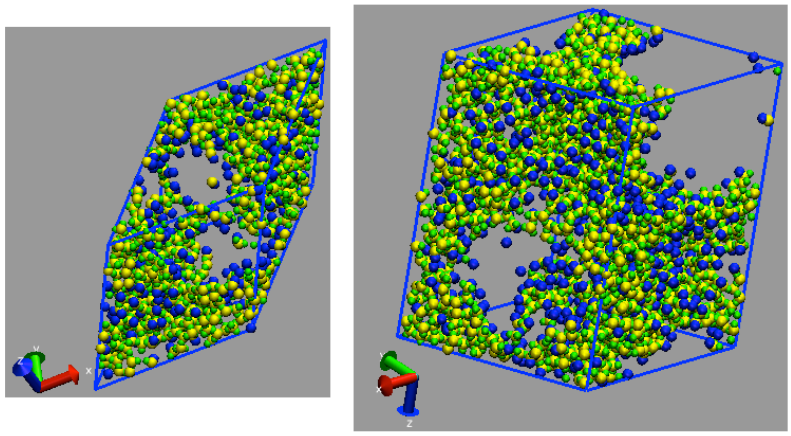

Figure 2-14: Final configuration for a STAC-1 model (left) and a SBA-2 model (right) after cooling.

2.3.6. Summary of differences between the simulation of these materials compared to that of MCM-41

Manipulation of the unit cell for the new systems (either SBA-2 or STAC-1) was easily done through a transformation matrix, which was embedded in the original code. However, the shape of the model micelles is now spherical rather than the MCM-41 rod-like micelles. The overall monomer-micelle interactions are thus changed in the sense that rather than being based on the distance between a point and a line (the cylindrical axis) they are now dependant on a point-point difference with respect to the centre of the spherical micelle. Furthermore, although the interaction potential of the micelles with the silica monomers remains the same as for the MCM-41 case, the micelle-micelle repulsion potential had to be modified (increased) as mentioned in section 2.2.5.3. The fundamental reason for this change became evident when working with the SBA-2 model pore, where the originally weak micelle repulsion led to the merging of the in-cell micelles.

The inclusion of these spherical model-micelles works in a similar way as the rod-like MCM-41 micelles. Thus, these micelles are also hard spheres at the beginning of the simulation preventing silica monomers from being placed within its radius. On the other hand, the number of neighbouring cells (from periodic boundary conditions) taken into account for micelle-micelle interactions in the original MCM-41 code was eight. This is reasonable for rod-like micelles since, when stacked in the hexagonal packing, their axis run parallel to each other and thus micelles in front, or behind, other micelles are effectively the same. This however is not true for the spherical micelles. In these systems all 26 neighbour images need to be taken into account. This means that the spherical micelle(s) in the unit cell may now interact with micelles in all neighbouring images provided their centre-to-centre distance is within the interaction cut-off.

The last important difference between the new code and that used to create MCM-41 model pores is the presence of unbound oxygens (i.e. water molecules) in

the unit cell. When simulating MCM-41 it is assumed that water produced during the polimerisation reaction diffuses quickly out of the system and thus they are immediately removed upon condensation. For the current systems however these unbound atoms representing water molecules can be left within the cell, moreover their presence was found necessary to promote the silica polymerisation reaction Since experimentally calcination temperatures force water molecules out of the system this now has to be taken into account in the simulations as well. Thus, the simulated SBA-2 and STAC-1 synthesis allows removing all the water molecules in the unit cell at once when the calcination stage begins.

Table 2-2: New features needed for the SBA-2/STAC-1 simulated synthesis.

	MCM-41	SBA-2
Micelle shape	Rod-like	Spherical
Micelle-micelle repulsion	Weak	Strong
Interaction with neighbour micelles	Micelles in eight neighbour cells considered	Micelles in 26 neighbour cells considered
Unbound oxygens (i.e. water molecules)	Not considered (disappear upon formation)	Present and interacting with other oxygens and micelles. Removed upon calcination.

In the following diagram (Figure 2-15) a flow chart of the algorithm used for the simulated synthesis of SBA-2 and STAC-1 is presented. Save for the differences stated above, it is consistent with the algorithm initially developed for MCM-41.

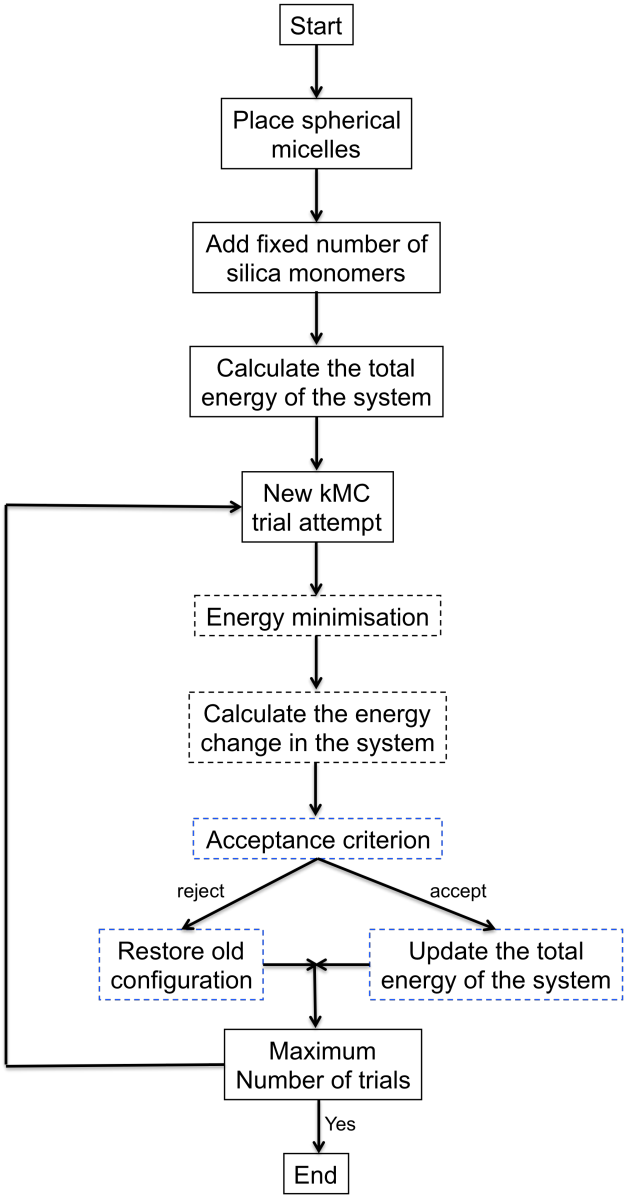

Figure 2-15: Backbone algorithm for the simulated synthesis of SBA-2 and STAC-1 materials

2.4. Characterisation of the model-materials

Just as experimentally different techniques provide information of different aspects of the porous materials, in simulations there are means to characterise the models to validate them by comparison to the experimental characterisation. These are presented below.

2.4.1. Visual inspection

By looking at the periodic representation of the models, using a program such as VMD, we aim to validate them by comparison to the TEM images reported in the literature (Zhou et al. 1998, Hunter and Wright 2001). The first thing that becomes apparent is that the shapes imposed to the simulation cells lead to the correct symmetry of both materials. In Figure 2-16 (left) the ccp layering structure for STAC-1 (A-white, B-green, C-red) is clear and the central pore is surrounded by 12 neighbour-pores as expected. The side view of the SBA-2 model (Figure 2-16, right) depicts the staggered AB sequence typical of the hcp packing.

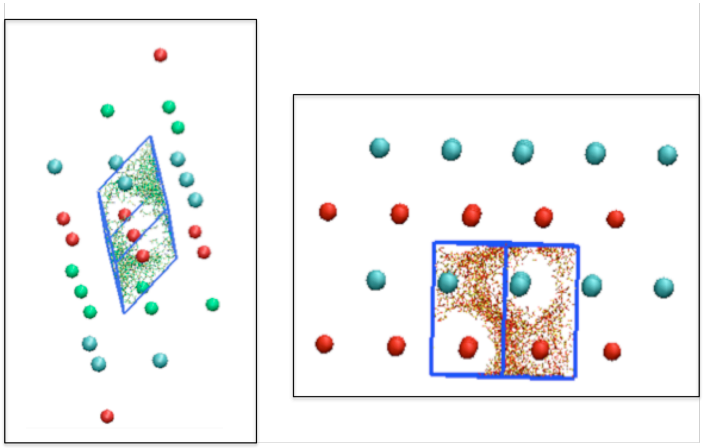

Figure 2-16: Location of the centre of the periodic pores showing the ccp sequence for STAC-1 (left, layers A-white, B-red, and C-green) and hcp sequence for SBA-2 (right, A-white, B-red) as achieved by the model-materials. The atoms in the unit-cells are shown in red (oxygens) and yellow (silicon atoms).

2.4.2. Degree of polymerisation

The degree of polymerisation proves that polymerisation of the silica monomers was achieved, and that it properly represents the Si-MASNMR spectrum of the SBA-2 samples. A direct comparison is difficult because the results published in the

literature are graphic rather than numeric (Hunter and Wright 2001), but nonetheless give an idea to what extent the simulations underwent a realistic polymerisation.

For both STAC-1 and SBA-2 models the evolution of the degree of polymerisation (DP) through the synthesis stages is similar, and thus it suffices to present one to represent them all. A quick recount of the silica monomers and their bridging oxygens provides the DP for the models as presented in Figure 2-17. From it, it is clear that the final model (after cooling) has two distinctive peaks for Q_3 and Q_4 with the latter being predominant. This agrees well with the reported SI-MASNMR spectrum found in the literature for samples calcined at 550 °C (Hunter and Wright 2001). Simulated models provide the advantage of giving a numerical result, and it can be seen that the fully polymerised monomers account for about 60 % of the total silica present with the remaining monomers being Q_3 which agrees well with the ~66 % Q_4 and ~30 % Q_3 for SBA-2 calcined at 550 °C reported by (Gonzalez 2005).

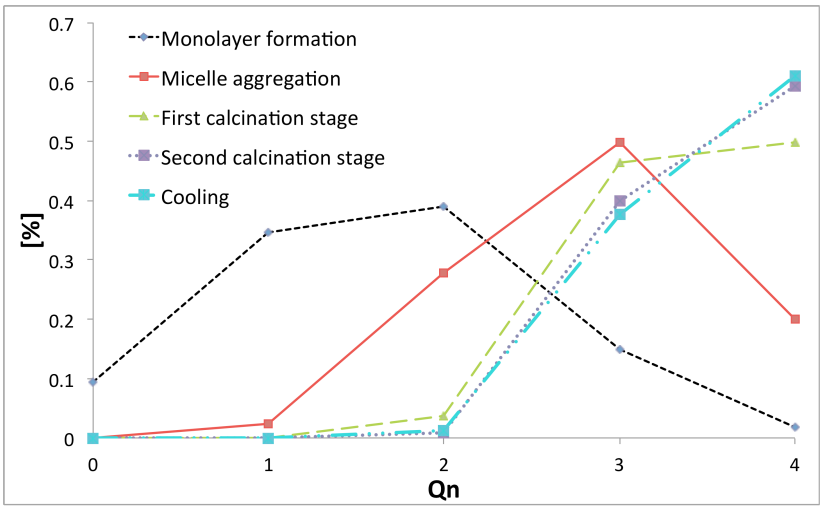

Figure 2-17: Q_n evolution example for a STAC-1 model synthesis.

2.4.3. Ring size distribution and radial distribution function

A ring is defined as the shortest non-reversing path of oxygen-silicon bonds connecting two different bonds on the same silicon atom (Schumacher et al. 2006b).

The number of Si atoms in a ring determines its size. In Figure 2-18 the evolution of the ring formation in the STAC-1 material is viewed by examining the STAC-1^J model during the different simulated synthesis stages.

At the end of the fist stage a very low number of 4-membered rings is seen probably due to the initial clustering of silica monomers, as evidenced by the large percentage of Q_1 and Q_2 silicon atoms showed in Figure 2-17. After the aggregation stage (i.e. stage two) rings of different sizes start to appear. The larger rings with more than nine silicon atoms result from the linking of different clusters of polymerized silica monomers. However, as the silica structure evolves the tension in these high-member rings force their silica members to condense and so the percentage of Q_4 monomers increases (Figure 2-17). When this happens, by the ring definition used here, rings of smaller sizes are created.

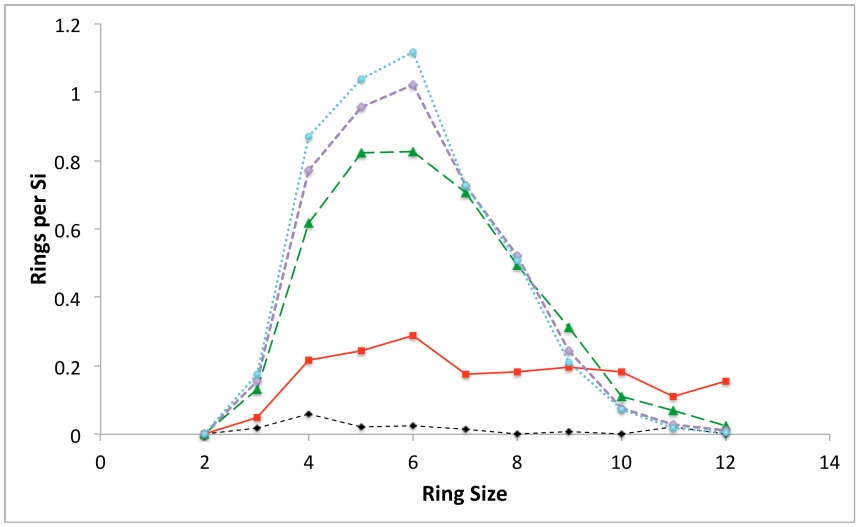

Figure 2-18: Ring size distribution evolution for the model STAC-1^J during the simulated synthesis. The colour coding is: stage one in black, stage two in red, stage three in green, stage four in purple, and stage five in cyan.

This can be seen in Figure 2-18 where after the first calcination stage the numbers of four to eight-member rings increase in detriment of the larger rings. This process is accentuated in the second calcination stage when the micelle is removed from the system and the shrinkage of the unit cell volume is greater. It is also evident that the cooling stage (Figure 2-18) other than allowing the formation of a few more small rings does not really vary the shape of the distribution. This is in line with

Figure 2-17, which shows that Q_n distribution variation provided by the cooling stage is negligible.

Figure 2-19 presents a similar study to that shown in Figure 2-18 but for the model SBA-2^A. At the end of the first stage the number of rings formed, unlike for STAC-1, is imperceptible. However this is likely to be related to the methodology of the simulation where SBA-2 silica condensation in this stage is restricted (as explained in section 2.3.1) to avoid the cross-linking of the silica layers belonging to its two different micelles before micelle aggregation is accounted for (stage two). In the real synthesis these two phenomena occur simultaneously, thus we imagine that the ring size distribution of the real material at this point is closer to that in Figure 2-18. Unlike for STAC-1, there is an increased presence of small rings (four to eight-member rings) early in the simulation after the aggregation stage concludes. This is reasonable since the space between the two micelles in this model pore allow for greater proximity of the silica clusters whereas in the STAC-1 model-pore they are more scattered.

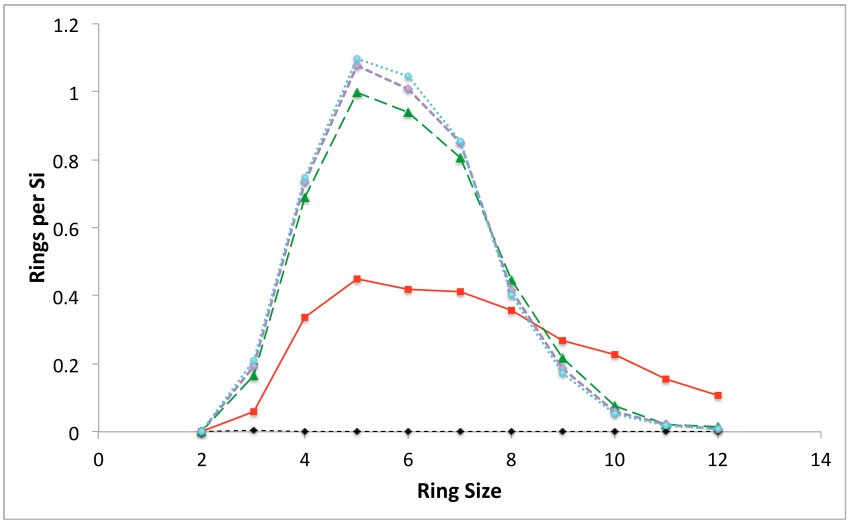

Figure 2-19: Ring size distribution evolution for the model SBA-2^A during the simulated synthesis. The colour coding is: stage one in black, stage two in red, stage three in green, stage four in purple, and stage five in cyan.

By comparing Figure 2-18 and Figure 2-19 it is clear that the early presence of small rings (over large ones) in the SBA-2 model pores allows a faster evolution of the ring size distribution in the material. Thus, after the first calcination stage of the

SBA-2 model pore, the ring size distribution is very close to that exhibited at the end of the simulated synthesis.

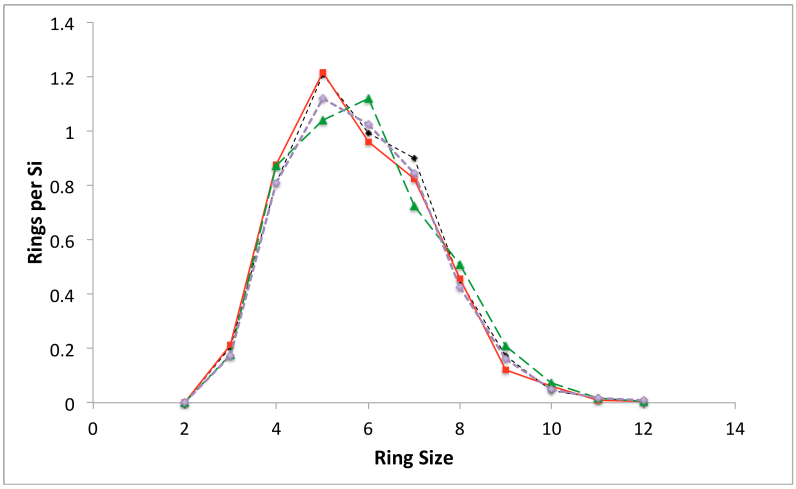

Figure 2-20: Ring size distribution comparison for models STAC-1^{B} (black), STAC-1^{F} (red), STAC-1^{J} (green), STAC-1^{H} (purple).

The evolution of the ring size distribution presented here for STAC-1^{J} (Figure 2-18) and SBA-2^{A} (Figure 2-19) is representative for each material studied. This is reinforced by Figure 2-20, where save for small differences in the final number of five and six-member ring for different STAC-1 model pores the final overall shape of the ring size distribution is comparable. In general, for both materials bi-monomer interactions and small cluster formation prevail at the beginning of the simulation. As the synthesis evolves rings formation takes over, being predominant from the first calcination stage onwards. Finally, it is worth noting that simulations of dense silica gels (Schumacher et al. 2006b) also showed that high-member rings (>8) tend to disappear as the kMC simulation evolve.

The radial distribution function depicts the short and long-range order of model-materials. The idea behind it is to examine the density of a given type of atoms *j* in a spherical shell separated by a radial distance $[r, r+\Delta r]$ from a selected type of atoms *i* by using (2-29) – further details are given in (Frenkel and Smit 2001). In ordered crystalline solids different peaks of *G(r)* indicated the lattice positions of the atoms respect to one another.

$$G(r)_{ij} = \frac{N_j(r, r+\Delta r)}{\frac{4}{3}\pi\rho_j\left[(r+\Delta r)^3 - r^3\right]} \quad \textbf{(2-29)}$$

However, for atomistically amorphous materials only a peak at very short distances is expected since its atoms do not occupy preferential lattice positions. By examining the relative position of the silicon atoms in the models this is clearly observed, Figure 2-21, corroborating that the model materials thus obtained through kMC simulations comply with this important characteristic of the real silica samples.

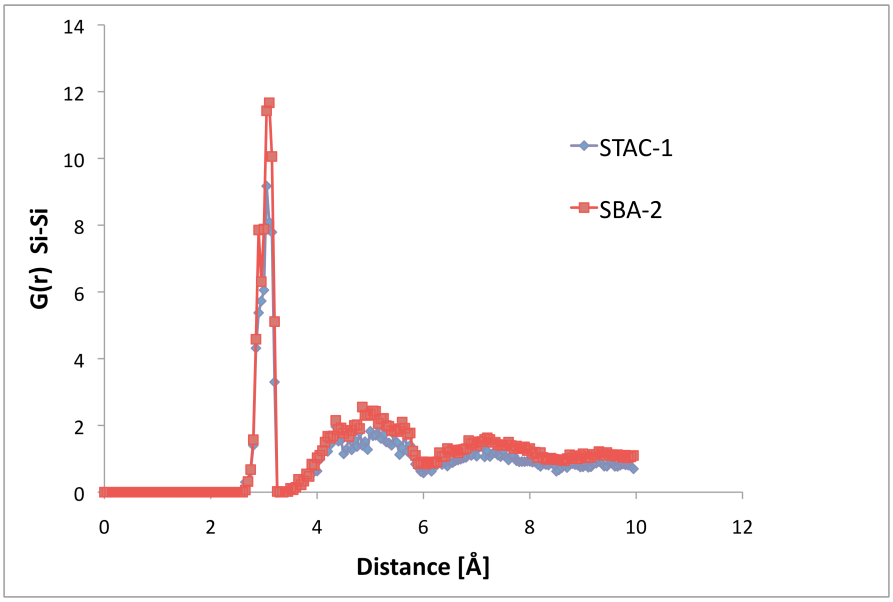

Figure 2-21: Si-Si radial distribution function.

2.4.4. Characterisation data of the pore models

The data presented in the following table were obtained as reported in sections 2.4.5 to 2.4.8. STAC-1 models O, P, Q, R, and S deserve special mention since they were obtained by simulated calcination of the same pre-calcined configuration at different network temperatures: 800 K, 1000 K, 1200 K, 1500 K, and 2000 K respectively.

Table 2-3: Characterisation of the pore models. M is the mass of the unit cell, a/b/c are the unit cell dimensions, CV_c is the contraction of the unit cell volume after calcination, Vt is the total volume of the final cell, Rnull is the final micelle radius before its removal, R is the final pore radius, SA is the surface area of the pore, ρ is the absolute density of the model, d is the fractal dimension, and PC indicates the presence (or not) of connecting windows. Data calculated by means of a random walk with a probe sphere of diameter 3.3 Å are indicated with *. Note that SBA-2 model pores are created from unit cells with two micelles.*

	Si atoms	*Silanol groups**	*M* (10^{-20} g)	*a*	*b*	*c*	CV_c (%)	V_t ($\times 10^{-20}$) (cm^3)	R_{null} (Å)	R^* (Å)	S_A^* ($m^2 g^{-1}$)	ρ (g cm^{-3})	d^*	*PC*
STAC-1[A]	800	323	8.45	48.03	49.38	47.41	27.0	7.95	22.28	19.93	994.4	3.31	2.83	Yes
STAC-1[B]	770	309	8.14	48.37	48.08	47.83	27.5	7.87	22.07	20.68	1087.2	3.37	2.84	Yes
STAC-1[C]	770	303	8.13	48.51	48.69	46.86	35.9	7.83	22.71	20.13	1053.0	3.25	2.78	Yes
STAC-1[D]	770	269	8.08	47.91	48.00	46.49	38.0	7.56	22.07	19.72	1041.7	3.57	2.85	Yes
STAC-1[E]	770	377	8.24	50.08	50.17	48.84	30.3	8.67	24.69	21.30	1165.7	3.21	2.78	Yes
STAC-1[F]	810	341	8.58	52.11	53.26	50.13	29.2	9.84	24.26	23.66	1290.1	3.31	2.74	Yes
STAC-1[G]	941	401	9.98	55.01	56.51	53.51	38.0	11.76	28.91	25.40	1291.3	3.26	2.70	Yes
STAC-1[H]	941	439	10.03	57.99	59.67	56.10	22.0	13.73	28.61	26.87	1342.5	3.07	2.49	Yes
STAC-1[I]	950	401	10.07	49.24	50.81	49.07	30.0	8.68	22.22	23.32	826.9	3.17	2.80	No
STAC-1[J]	1000	423	10.60	52.93	54.64	52.47	23.0	10.73	25.82	22.95	1045.7	3.07	2.79	Yes

Table 2-4: Continuation from Table 2-3

	Si atoms	*Silanol groups* *	*M* (10^{-20} g)	*a*	*b*	*c*	CV_c (%)	V_t ($\times 10^{-20}$) (cm^3)	R_{null} (Å)	R^* (Å)	S_A^* ($m^2 g^{-1}$)	ρ (g cm^{-3})	d^*	*PC*
STAC-1[K]	1150	463	12.15	54.81	54.90	53.46	32.0	11.37	24.79	22.84	871.5	3.03	2.73	No
STAC-1[L]	1150	509	12.22	54.73	55.49	53.72	34.7	11.54	26.38	22.97	881.9	3.20	2.73	Yes
STAC-1[M]	1150	525	12.24	57.24	58.37	55.33	26.0	13.07	28.64	24.77	1062.7	3.20	2.72	Yes
STAC-1[N]	1250	619	13.38	60.90	62.69	59.21	23.9	15.98	30.97	27.46	1172.0	3.06	2.68	Yes
STAC-1[O]	1150	565	12.30	56.69	57.94	55.76	23.4	12.95	28.05	25.06	1075.3	3.08	2.76	Yes
STAC-1[P]	1150	543	12.27	56.75	57.30	55.31	24.8	12.71	28.05	24.40	1052.4	3.19	2.77	Yes
STAC-1[Q]	1150	523	12.24	56.07	57.12	55.26	26.0	12.51	28.05	24.25	1039.6	3.13	2.75	Yes
STAC-1[R]	1150	461	12.15	55.52	56.55	54.34	28.7	12.06	28.05	23.73	999.2	3.10	2.75	No
STAC-1[S]	1150	435	12.11	55.54	55.69	54.58	29.4	11.94	28.05	24.31	1009.9	3.50	2.74	No
SBA-2[A]	1693	797	18.06	53.20	53.15	85.53	26.6	20.95	24.89 24.93	23.81 24.49	1245.0	3.29	2.70	Yes
SBA-2[B]	2300	1263	24.80	56.28	56.71	92.11	22.4	25.45	27.85 27.72	24.85 24.61	999.4	3.03	2.72	Yes

2.4.5. Pore radius and surface area

Because of the amorphous nature of the material the radius of the pores need to be represented statistically by means of an average and standard deviation. Imaging tools are not sufficient for this purpose, thus a quantitative method based on a random walk was developed.

The random walk uses a 'probe' sphere of a given size that is placed at the centre of the pore to be studied. From that position a random orientation is given with a step size short enough to ensure the new and the old positions overlap each other (the radius of the probe was chosen as the step size), and this process is repeated for a great number of steps (two million steps). Once the probe reaches the surface, each time it touches a wall-atom it reports its distance to the centre of the pore and then the probe is replaced in its previous position so that the random walk may continue. A record of wall atoms touched by the probe is kept to avoid repeating measurements, and in the end a radius distribution is reported. Following the work of Gadelmawla and co-workers (Gadelmawla et al. 2002) the statistical numbers thus obtained are:

- Average radius (r_{av})
- Standard deviation of the radius
- Skewness: based on the profile of the third central moment of the distribution and sensitive to both gaps in the walls and peaks. Profiles with more peaks than valleys will have a negative skewness while for the opposite scenario it adopts positive values
- Kurtosis: based on the fourth central moment, it describes the sharpness of the profile. If it is lower than 3 then the distribution has few peaks and gaps (platykurtoic), whereas if it is larger than 3 there are many (leptokurtoic).

In general, the pore models show a positive skewness and kurtosis above the mentioned threshold, indicating very rough surfaces characterised by many gaps in

the pore wall. The pore radiuses for the different models are reported in Table 2-3 and Table 2-4, their diameters varying between 40 Å and 55 Å in agreement with reported pore sizes for SBA-2: ~41 Å (Huo et al. 1995), ~45 Å (Kim and Stucky 2000), ~47 Å (Perez-Mendoza et al. 2004a).

The surface area of the pore wall is calculated by (Düren et al. 2007) taking the probe sphere and placing it randomly (5000 times) on the Lennard-Jones surface of each wall-atom, then the surface area contribution from the wall-atom is given by the fraction of times the probe did not overlap a neighbour wall-atom multiplied by the averaged radius of the probe and the wall-atom being checked. Finally, the sum of the surface area contributions from every wall-atom is the total surface area on the pore walls.

Figure 2-22 shows a comparison between the surface areas calculated for the STAC-1 models as presented above versus the ideal surface area obtained as the surface of a sphere with mean radius r_{av} (as reported in Table 2-3 and Table 2-4). Clearly for all the models the calculated surface area is larger than that of the idealized spheres, and this was expected as the excess surface area is a direct result of the nooks and crannies on the pore surface: the pore-wall rugosity.

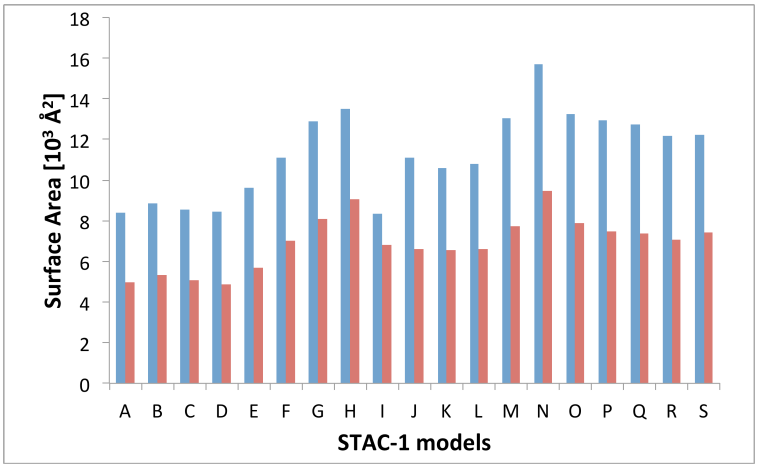

Figure 2-22: Surface area for the different STAC-1 models. Blue bars correspond to the surface area calculated as in (Düren et al. 2007), while red bars indicate the surface area corresponding to an ideal-smooth sphere of mean radius r_{av} (calculated with the probe molecule).

In Table 2-3 and Table 2-4 the surface area of the different models is reported in m^2g^{-1}, which are its common units. Its value (including the SBA-2 models) oscillates between 800 m^2/g and 1350 m^2/g (the mean being slightly above 1000 m^2/g), and this compares well to experimental calculations reported in the literature: 572 m^2/g (Kim and Stucky 2000), ~900 m^2/g (Hunter and Wright 2001).

2.4.6. Absolute density

Helium is an ideal gas and as such feels little interaction with the siliceous adsorbent; in fact for any purpose it is assumed that helium is a non-adsorbing gas (though there may be some exceptions (Myers and Monson 2002)). Details about adsorption simulations can be found on Chapter 3, at this point it suffices to know that by carrying out such simulations using helium as an adsorbate at a given temperature and pressure then the ideal gas equation [in its microscopic expression, Equation (2-30)] is applicable and the helium-volume V_{He} can be obtained from it, which is equivalent to the total void volume in the system.

$$PV_{He} = N_{He}k_bT \qquad \textbf{(2-30)}$$

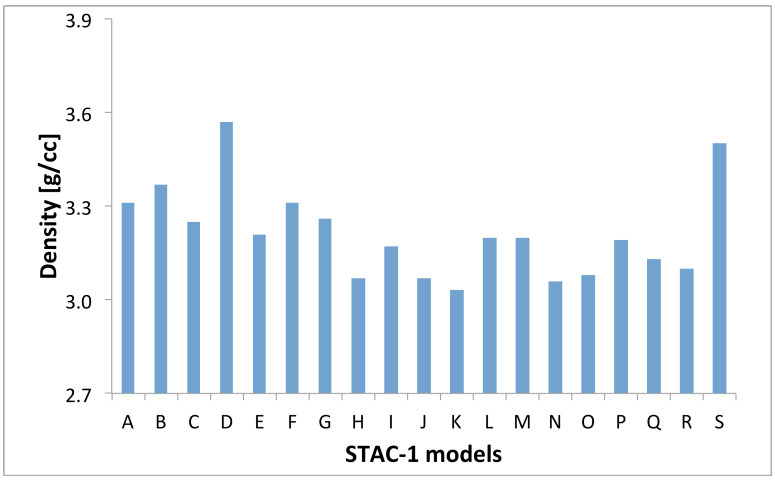

Figure 2-23: Absolute density for the STAC-1 models.

After calculating the pore volumes (i.e. V_{He}) for the pore models their absolute densities are calculated as the ration between the mass of the unit cell and the volume occupied by the silica structure (V-V_{He}). From Figure 2-23 it can be seen that the density of the STAC-1 models varies between 3.0 g/cm^3 and 3.6 g/cm^3, which is also true for the SBA-2 models for which densities of 3.0 g/cm^3 and 3.3 g/cm^3 were achieved. This compares well to experimental calculations on SBA-2 samples calcined at 550 °C for which an absolute density of 3.2 g/cm^3 was found (Prof. Wright 2007-2010).

2.4.7. Surface roughness

Using probe molecules of different sizes it is possible to calculate the fractal dimension of the pore-wall surface (Torrens and Castellano 2006) using Equation (2-31), where r_{probe} and A_{probe} are the probe radius and surface area of the corresponding sphere, d is the fractal dimension to be estimated and S_A is the surface area of the pore wall. Plotting the surface area obtained for each probe size gives a linear fit with a slope equal to the fractal dimension, which is directly related to the roughness of the pore model – see Figure 2-24.

$$\log\left(\frac{S_A}{A_{probe}}\right) = d * \log\left(\frac{1}{r_{probe}}\right) \quad \textbf{(2-31)}$$

Figure 2-24 shows an example calculation of the fractal dimension for the model STAC-1^B. Considering that the fractal dimension must lie between two (smooth surface) and three (subsequent dimension), this model has a high fractal dimension (2.84), in fact, of all the models the one with the lowest fractal dimension is STAC-1^H (2.49). This supports the conclusion derived from the surface area calculations, where it was found that the walls of the pore models have an increased surface area contribution from this roughness.

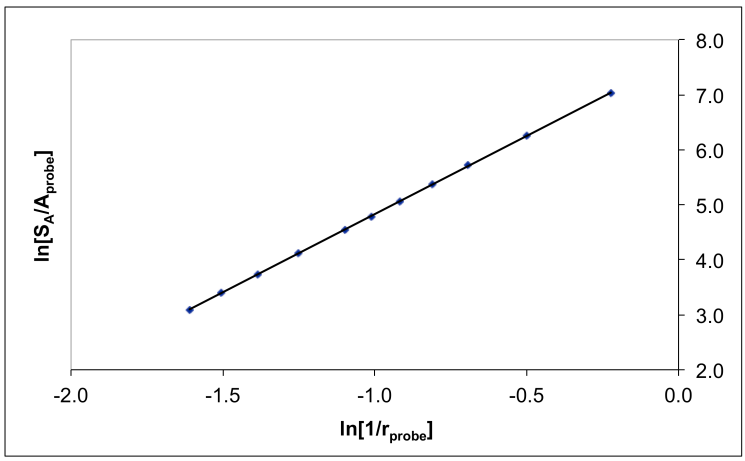

Figure 2-24: Calculation of the fractal dimension for STAC-1^B. The reported fractal dimension for this model pore is d = 2.84.

However, no experimental measurements of the SBA-2 or STAC-1 surface roughness or on the fractal dimension of their surfaces are available. Therefore these values cannot be validated against experimental results but rather provide a mean to compare the behaviour of the different models in terms of their relative roughness.

2.4.8. Pore connectivity

An important feature of both STAC-1 and SBA-2 materials is the connectivity of their pores. It has been reported that the process leading to the formation of this connections is unknown (Perez-Mendoza et al. 2004a), and it was hoped that the kMC technique would help shed some light on the matter. The simulation of the synthesis process through the different stages showed a possible mechanism for the formation of these connections: micelle aggregation leads to weak – thin – silica walls separating them, and even in some cases, micelles directly touching each other through areas of scarce silicic acid monomers partially due to the presence of unbound oxygens near the micelle-silica interface.

The resulting connections should be described as 'windows' rather than channels as can be seen in Figure 2-25. In both the ccp and the hcp structures a coordination number of 12 means every pore '*p*' is surrounded by 12 others, but out of those 12

only up to four were found connected to *p*. In fact, the number and size of the connections varies for each model pore and this makes their study through percolation not worthwhile pursuing with these models. Systems with at least twice the number of micelles would be needed to get an accurate percolation description of the problem at hand. This unfortunately would lead to excessively large simulations, computationally expensive and time-consuming, that at present are not feasible, though it may be a suitable study in the near future.

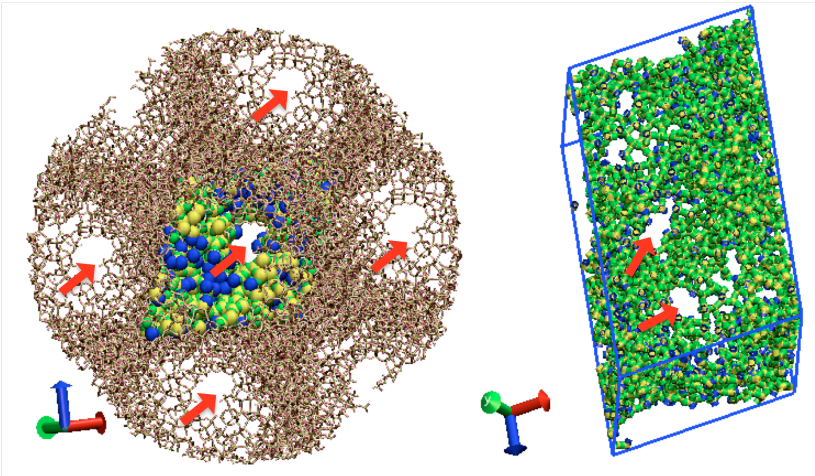

Figure 2-25: Example of pore connectivity for: STAC-1^{B} (left), where the neighbour silica network is shown for clarification purposes while the main unit-cell is highlighted using spherical representation of its atoms; and SBA-2^{A} (right). Red arrows indicate the place and direction of the connections present.

Figure 2-25 also shows that the two model pores STAC-1^{B} and SBA-2^{A} correlate well with experimental TEM images (Zhou et al. 1998) where the STAC-1 model presents straight connections while the SBA-2 model presents both straight and zigzag connections. Note that the top arrow on the SBA-2 model points to a connection between the two micelles in the simulation cell representing the layers A and B respectively (if we periodically repeat the layers in *c* it is easy to visualize the zigzag connections) while the bottom arrow points at two micelles in the same A layer being connected.

Furthermore, by taking a closer look at these connecting windows (using visualization software such as VMD) it is possible to get a general idea of their size –

see Figure 2-26. The numbers reported in that figure are in Å and represent point-to-point distances between Si atoms in edges of the windows. Knowing that the Si atoms are fully surrounded by oxygens, which have a Lennard-Jones diameter of 2.708 Å if they are bonding oxygens and 3.000 Å if they are non-bonding oxygens (encompassing the effect of the bonded hydrogen atom) (Düren 2002) it is safe to say that the true width of the opening is somewhere about 6 Å. This is about the size expected by experimentalists as has been discussed in meetings with Prof. Paul Wright from the University of St. Andrews (Prof. Wright 2007-2010). However, it can also be observed in Figure 2-26 that this width depends on the position of the atoms used for the measurement, which is to say that these windows do not present a distinctive geometry.

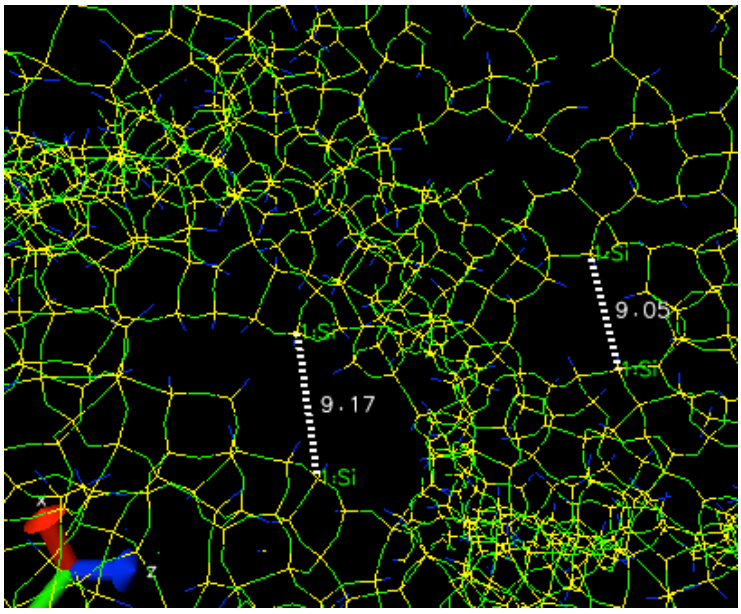

Figure 2-26: Close up of the connecting windows for the SBA-2^{A} model. Distances are given in Å and were displayed around the centre of each connection measured from the centres of the silicon atoms.

Because the connecting windows are tortuous: they do not posses a uniform width, and their edges are rarely directly opposed in the same plane, they are likely to affect the dynamics of adsorption especially for large molecules. Although the image presented is specific to the SBA-2^{A} model pore, the same characteristics are observed in the other model pores synthesised, with the exceptions of a few with no connections at all (Table 2-3 and Table 2-4).

With the random walk, it is also possible to gather information regarding the connectivity of the pores. If for example we are interested in separating CO_2 from other mixture components, a probe sphere with a diameter of 3.3 Å (which corresponds to the kinetic diameter of CO_2) could be used to check if it can escape the pore into the neighbouring pores or not (this is the Boolean connectivity reported in Table 2-3 and Table 2-4).

2.4.8.1. Evolution of connections during the simulations

The evolution of the connecting windows formation during the synthesis simulation is presented in this section. The model SBA-2^A (represented in Figure 2-27 during the aggregation stage) was chosen as case study for visualisation purposes. The discussion presented here can be readily extended to the window-formation in any other SBA-2 or STAC-1 pore model.

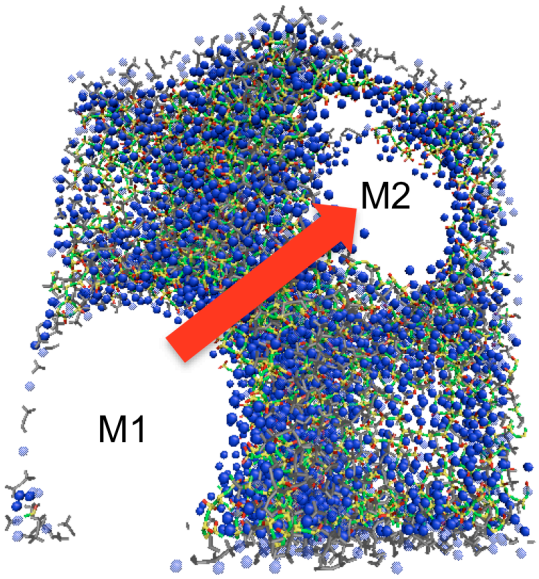

Figure 2-27: SBA-2^A pore model during the early stage two (structure in grey, water molecules in pale blue) compared to the configuration at the end of the same stage (structure in red and yellow, water molecules in blue).

The SBA-2 model pore has two micelles in the simulation cell that for the purpose of this discussion are named M1 and M2 (Figure 2-27). When positioned

inside M1 and looking in the direction of the red arrow (figure above) towards M2 a snapshot such as the ones in Figure 2-28 is obtained. This figure presents two overlapped snapshots, one taken at an early configuration (structures in grey and water molecules in pale blue) and another at the end (structure in colours and water molecules in blue) of the aggregation stage. Note that the silica structure between the micelles is withdrawing in this region (which is the area where the micelles are closest to each other) as the aggregation stage takes place. The evolution of the silica condensation leads to the presence of more water molecules (there is a larger percentage of blue spheres than those in pale blue), which are lured to the silica-micelle interface by their interaction with the micelles' potential. Furthermore, many of these new water molecules end up in the region where the silica structure was already thinned by the micelles proximity (shaded area in Figure 2-28).

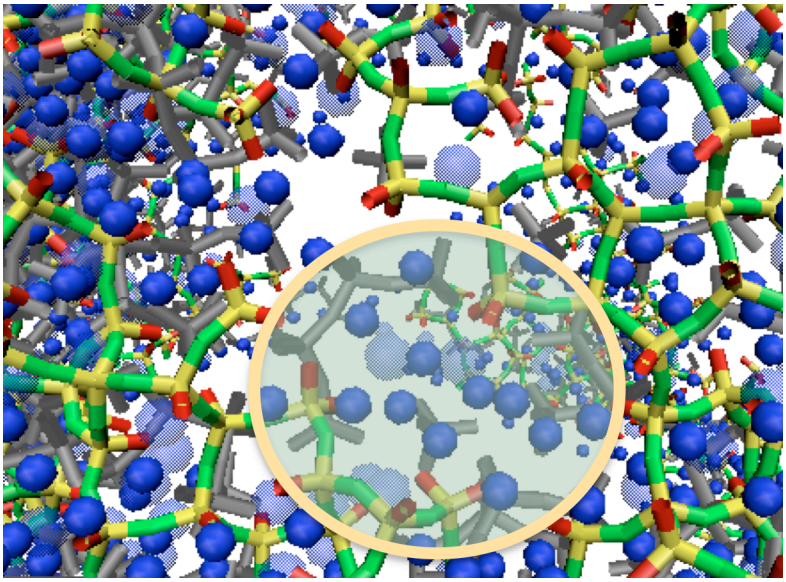

Figure 2-28: Zoom into the evolving connecting window between the two micelles (looking from M1 to M2, compare Figure 2-27). The structure at an early configuration in stage two is in grey (water molecules in pale blue) while the structure at the end of the stage in fully coloured: bounding oxygens in green, non-bounding oxygens in red, silicon atoms in yellow and water molecules in blue. The shaded area show water molecules placed in the region where the silica structure was thinned by the proximity of the micelles.

In Figure 2-29 the structure at the end of the aggregation stage (grey structure) once the water molecules are removed can be compared to the structure at the end of the first calcination stage (coloured). By comparing both snapshots it is possible to

see a slight contraction of the window as the calcination takes place. The calcination network temperature in this case is 800 K and it is apparent that the shrinkage of the unit cell does not close this opening. This may also be because of the model-micelles initial expansion searching to maximise the contact area with the silica monomers (thus minimising the energy in the system). Nonetheless, larger temperatures may induce strong shrinking stresses (as later reported for pore models STAC-1^R and STAC-1^S) thus closing these connections. Figure 2-29 also shows the approximate size of the studied connection at the end of the first calcination stage.

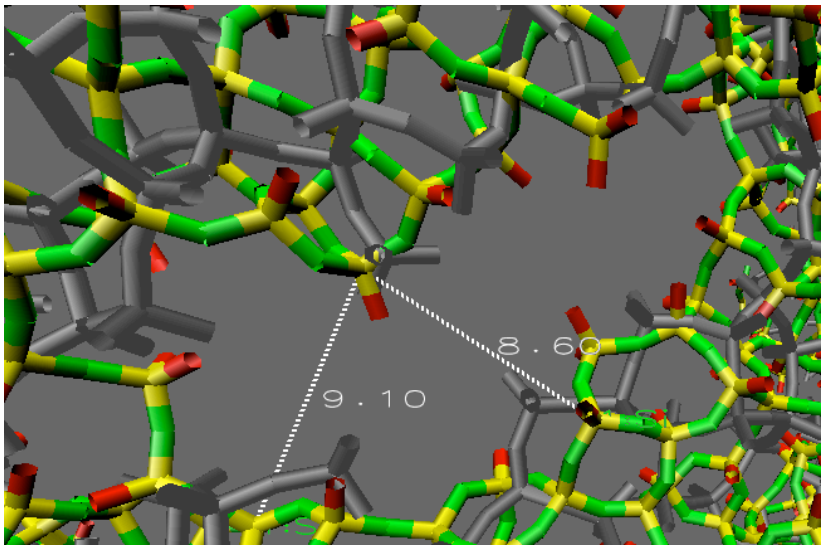

Figure 2-29: Evolution of the connecting window between micelles M1 and M2 (as seen from M1) from the beginning (structure in grey) to end (structure in colour) of stage 3. The colour code is: bonding oxygens in green, non-bonding oxygens in red, and silicon atoms in yellow. The size of the window is measured only for the coloured structure.

Finally, Figure 2-30 shows the variation of the structure between the configuration at end of the first calcination stage (colour) and that of the final material (grey). The window remains almost the same in shape and size despite the absence of the model micelles in the simulation cell. This indicates that the effect of the second calcination stage is that of restructuring the silica connections by promoting the transition from Q_3 to Q_4 monomers, and thus affecting the ring size distribution, rather than promoting the formation of new bonds by structural reorganisation of the models.

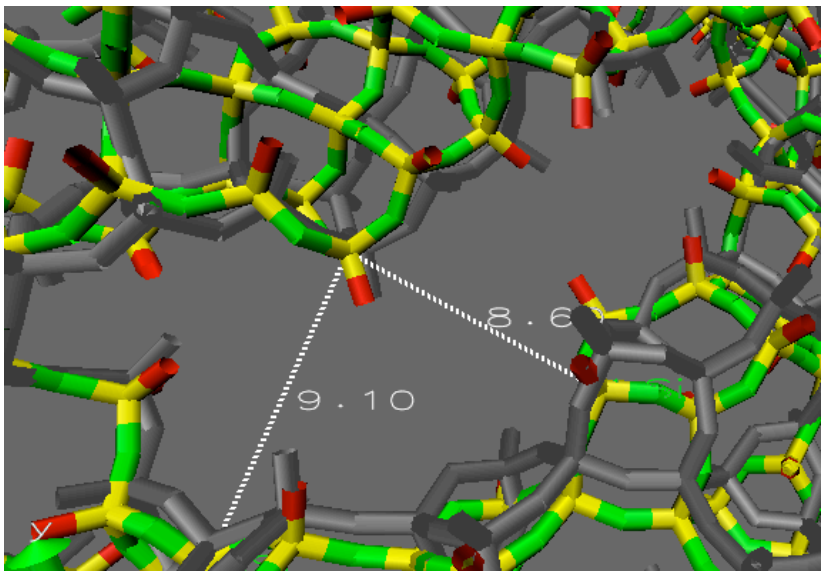

Figure 2-30: Evolution of the connecting window between micelles M1 and M2 (as seen from M1) from the beginning (structure in grey) to end (structure in colour) of stage 4. The colour code is: bonding oxygens in green, non-bonding oxygens in red, and silicon atoms in yellow. The size of the window is measured only for the coloured structure.

2.4.9. Effect of the calcination temperature

The effect of the calcination temperature is further studied using the models *O* through *S*, where the same parent configuration obtained after stage 2 was used for calcination at 800 K, 1000 K, 1200 K, 1500 K, and 2000 K respectively. Figure 2-31 shows that in general the pore size diminishes with increasing calcination temperature, which is also what happens to the simulation cell. Furthermore, it is found that for the two highest calcination temperatures the connecting windows are closed even for a small probe the size of CO_2. This is consistent with experimental observations where calcination at temperatures higher than 900 K seems to lead to structures with either unconnected or collapsed cavities (Prof. Wright 2007-2010). The unit-cell contraction increases with higher calcination temperatures. Calcination of models *O* through *S* lead to 23.4, 24.8, 26.0, 28.7, and 29.4 % of shrinkage respectively. Moreover, a stepwise increase in temperature during calcination seems to favour network restructuring over cell contraction, since the STAC-1^H model showed both the lowest cell contraction (22 %) and smoothest surface.

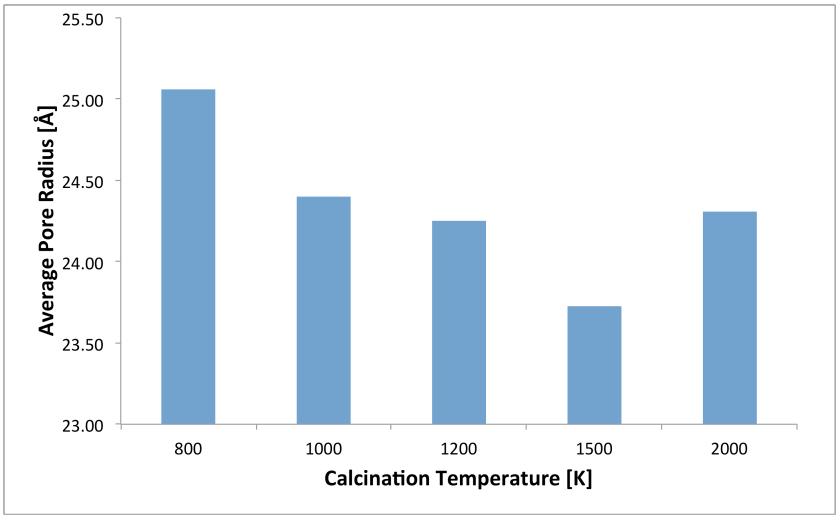

Figure 2-31: Average pore radius after different calcination temperatures. Model O was calcined at 800 K, model P at 1000 K, model Q at 1200 K, model R at 1500 K, and model S at 2000 K.

Models *G* and *H* provide an insight into the difference between calcination through a step-like (*G*) increase in temperature and calcination by means of a ramp-like increase of temperature (*H*, using step intervals of 25 K). The latter provides a model with less surface roughness (fractal dimension of 2.49 rather than 2.70), this may arise because small increments in temperature allow the system to relax better and soften surface strains that otherwise remain present.

As a final comment, it must be noted that producing models for STAC-1 is a time consuming task since the entire simulation can take up to three weeks, with each system consisting of at least 700 silicon atoms (2800 oxygen atoms). However, that is still a very reasonable amount of time when compared to the almost eight weeks (in one CPU using parallel OMP) that may take for an SBA-2 model to be completed (this systems being at least twice as large, 7000 atoms, as the STAC-1 models). It is for this reason that many models for STAC-1 could be produced whereas only two were made for SBA-2.

The pore models were obtained by means of the CLX cluster at the University of Edinburgh, running on dual-core CPU machines, each with 32 GB of RAM and AMD opteron processors (8 GB per core) and 2.4 / 2.6 GHz.

2.5. Concluding remarks

Modelling the formation of SBA-2 and STAC-1 materials by means of the kMC methodology following the silica condensation and aggregation mechanism was successfully achieved. Characteristics such as the symmetry of the materials and their pore size were imposed by careful manipulation of the unit cell shape and model-micelle(s) size respectively. However, the latter serves just as an indication as to the final pore size since this is also affected by other factors such as the number of silica monomers, the parameters of the micelle potential, and the network-temperature of calcination (which effectively contracts both the unit cell and the micelle(s) in it).

In order to achieve the distinctive ccp and hcp layering in the materials the repulsive potential between micelles needed to be stronger than that used previously for MCM-41 (Schumacher et al. 2006b). Physically this can relate to the double-headed nature of the gemini surfactants, although a direct relation is hardly possible due to the simplistic nature of the micelles used for the simulation that consist of a spherical geometric shape rather than explicitly including the surfactant molecules. Furthermore, unlike for MCM-41, the unbound oxygens (i.e. water molecules) product of the polymerization reaction had to be kept in the unit cell until the calcination stage, as their interaction energy contribution was found necessary to promote the silica condensation. These unbound oxygens were assumed to have the same interaction potential as the oxygens belonging to the silica monomers.

As a normal consequence of the synthesis simulation connecting windows formed between the pores, as early as in the second simulation stage where the micelles aggregate. Their formation appears to be related to the combined effect of the proximity of the micelles plus the presence of ‘water’ molecules on the silica-micelle interface, both leading to thin (or non-existent) silica wall regions that later become the means for pore connectivity. The number of connections (about four on average) is very low when compared to the pore coordination number (twelve). The

symmetry of the material influences the direction of such connections in close relation to experimental studies (Zhou et al. 1998).

The calcination stage correlated well to the experimental synthesis of these materials. An average cell contraction of 27.5 % was observed compared to 33 % experimentally (Hunter and Wright 2001). It was also noted that this shrinking effect is related to the calcination temperature: higher temperatures increase the unit cell contraction. The amorphous nature of the final pore model is confirmed by studying its radial distribution function. Furthermore, its degree of polymerisation shows distinctive peaks at Q_3 and preferentially at Q_4 clearly indicating the presence of a fully developed silica structure.

In the next chapter the behaviour of these model pores in adsorption simulations is evaluated with the aim of using them later for material design by surface modification. To that end we studied systems with both polar and non-polar adsorbates and derived quasi-pore size distributions to improve the obtained predictions.

3. Adsorption Study

This chapter begins by giving a brief overview on adsorption, how it is measured experimentally, and how simulated adsorption results can be compared to these experimental results. It continues by giving relevant information on the theory behind molecular simulations of adsorption and presenting a description of the adopted force field to represent the silica structure. Adsorption simulations results for the following pure adsorbates: helium, nitrogen, methane, ethane, and carbon dioxide are then presented and, where possible, compared to measurements on a SBA-2 sample calcined at 550 °C, (Perez-Mendoza et al. 2004a, Perez-Mendoza et al. 2004b). The possibility of improving the predictions by means of a quasi-pore-size distribution is also examined.

Comparisons to the experimental data for SBA-2 mentioned above are made independently of whether the pore model corresponds to SBA-2 or STAC-1, since there is no conclusive proof in the literature that the synthesis process leads to either material preferentially (see discussion on spherical close-packing in Chapter 2). These materials are likely to coexist in the same sample (Zhou et al. 1998) and thus they alter the number and tortuosity of the pore connections within it but rather exhibit the same pore shapes and size. It is a sensible assumption then that isotherms obtained using either modelled material will lead to equally accurate predictions.

3.1. An overview of adsorption

Adsorption is a surface phenomena: molecules from a gas flowing through a porous solid are attracted to the surface of the pores where they stick with varying strength depending on the nature of both the adsorbate (i.e. the gas) and the adsorbent (i.e. the solid). When this interaction is too strong, so that the adsorbate molecules lose their identity by forming bonds (sharing electrons) with the surface, it

is called chemisorption, while when the interactions are weak enough to barely disturb the molecule's electrons it is called physisorption.

Physisorption unlike chemisorption does not necessarily lead to a single layer deposition on the solid surface but rather to multiple layers. Due to the weaker solid-fluid interactions in physisorption, the reverse process (desorption) requires less energy and is therefore less expensive. This makes physisorption very appealing for processes where the adsorbed fluid needs to be recovered (like carbon capture and storage). Adsorption isotherms show the amount adsorbed at a fixed temperature with varying pressure,

$$N = f(T,P) \tag{3-1}$$

The amount adsorbed results from the equilibration of the chemical potentials on the surface of the solid and on the fluid occupying the porous space. As it is depicted in Figure 3-1, when the chemical potentials for each adsorbate species present equilibrate then for every molecule of species *i* approaching the surface there will be one molecule of the same species heading back to the fluid bulk.

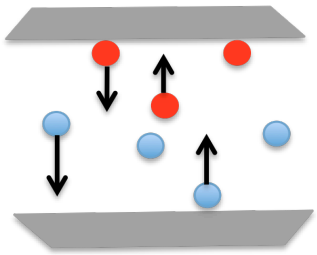

Figure 3-1: When adsorption equilibrium is reached for a thermodynamic system defined by a given temperature and pressure, just as many new adsorbate molecules are adsorbed onto the surface as they are released to the fluid bulk

Depending on the nature of the adsorbent, the isotherm can adopt different shapes. At low pressures the adsorption occurs mainly due to solid-fluid interactions, whereas at high pressures it is the capacity of the adsorbent that determines the amount of fluid that can be retained in it. Both are very important factors when designing adsorbents for specific applications. The International Union of Pure and

Applied Chemistry (IUPAC) classifies adsorption isotherms according to Figure 3-2 (Rouquerol et al. 1999)

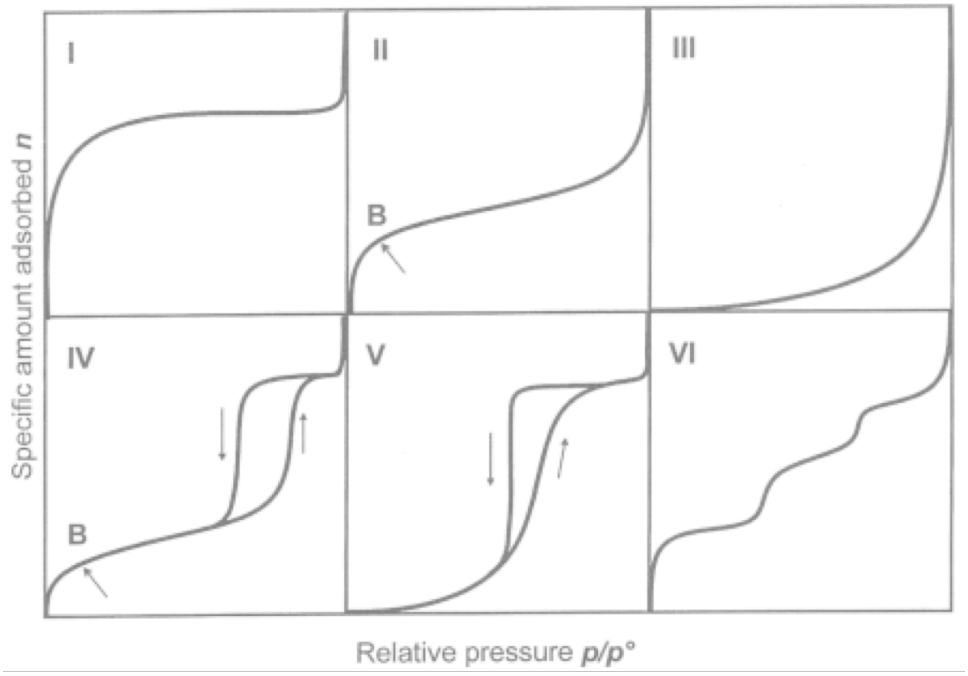

Figure 3-2: Classification of adsorption isotherms (IUPAC) (Rouquerol et al. 1999).

Type I isotherms are typical of microporous adsorbents. Mesoporous adsorbents usually exhibit one of the other isotherms, where type II and IV isotherms indicate a system with strong solid-fluid interactions as opposed to types III and V isotherms. Different theories and models have been developed aiming to describe the most common isotherms (types I and II), among which are those based on the Langmuir approach, the Gibbs approach and the potential theory. However, they rely on adjustable parameters that give little information of the nature of the solid-fluid interactions in the systems.

There are many methods to measure adsorption experimentally, among which are the volumetric, the gravimetric, the dynamic, and the chromatographic methods, which are described in the literature (Yang 1997). Adsorption experiments can be costly and time consuming, so it is desirable to avoid making numerous experiments. Simulation of adsorption processes provides the means to narrow the experimental

measurements to those adsorbents that are potentially useful for a desired application, and also provides insight into the nature of the solid-fluid interactions taking place. The accuracy of the simulations depends on the realistic representation of the adsorbent being studied, as well as of the intermolecular forces acting on the adsorbate molecules, which for the solids under study are: dispersion (London) and polar forces.

London forces are the result of fluctuations in the atoms electron-density inducing electric moments in its neighbouring atoms; these are therefore short-ranged forces leading to weak attractive effects. Polar forces, on the contrary, are long-ranged in nature and have an important contribution to adsorption when the adsorbate molecules have permanent dipoles and/or quadrupoles.

3.2. Microscopic approach to adsorption

Molecular simulation of adsorption uses Monte Carlo integration in form of a Metropolis algorithm (as described in Chapter 2) to calculate the amount adsorbed in a system with known pressure, volume and temperature. Unlike the kinetic Monte Carlo technique described in the previous chapter we are no longer interested in the evolution of the system but rather on its properties at equilibrium.

The thermodynamic equilibrium of a macroscopic system is defined as the moment after which its properties remain constant in time. This could be directly applied to molecular dynamics simulations, where the basic idea is to study the time-evolution of the system but not to MC simulations. The latter describes the system through a collection of microstates (called an ensemble) that, as was mentioned before, are ‘pictures’ representing the positions of the molecules within the system according to the specified thermodynamic conditions by means of a partition function.

What must be noted is that although the thermodynamic equilibrium means the macroscopic properties are constant, the microstates corresponding to the macroscopic state are infinite since molecules are in constant movement. This conceptual basis is the foundation upon which macroscopic properties can be calculated by means of MC simulations and it is called the 'ergodic hypothesis': in a thermodynamic system for which an appropriate ensemble (i.e. that describes the thermodynamic state and environment of the system) is chosen the – sufficiently long – time average of a property $\rho(r)$ is equal to its ensemble average $<\rho(r)>$ as the number of microstates approaches infinity.

$$\bar{\rho}_i(r) = \langle \rho_i(r) \rangle \qquad \textbf{(3-2)}$$

The thermodynamic properties that define the macroscopic system also define the ensemble to be chosen for computer simulations. Adsorption simulations are simulated through the grand-canonical ensemble (μVT) by means of the Metropolis Monte Carlo method.

3.2.1. Grand-canonical Monte Carlo

First, it is necessary to introduce the grand-canonical ensemble (Figure 3-3). It consists of an open system (adsorbate molecules are constantly exchanged with an infinite reservoir) thermodynamically defined by constant temperature T (i.e. it is assumed to be submerged in a thermal bath), known volume V, and constant chemical potential for each adsorbate (*i)* μ_i. Since the chemical potential is fixed, its thermodynamic conjugate variable - the particle number N_i – varies, and it is the average of this fluctuating variable that leads to the amount adsorbed.

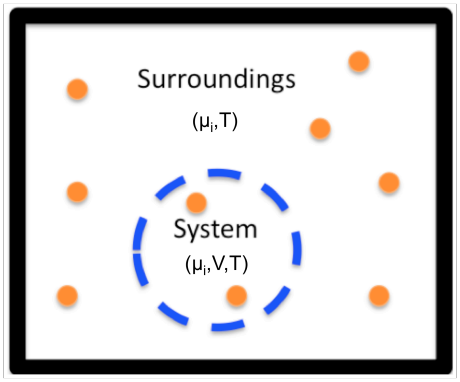

Figure 3-3: Thermodynamic system definition for a grand-canonical ensemble in contact with the surroundings. The dash blue line indicates particles can be exchanged between the system and the surroundings.

In Figure 3-3 the open system under study (at fixed temperature and volume) is able to exchange *a* molecules (orange dots) with the surroundings. The partition function for the system in the ensemble is given by (Frenkel and Smit 2001),

$$Q_{(\mu,V,T)} \equiv \sum_{N=0}^{\infty}\left[\left(\frac{V^N}{N!}\right)\frac{\exp(\beta\mu N)}{\Lambda^{3N}}\right]\int ds^N \exp\left[-\beta U(s^N)\right] \tag{3-3}$$

This equation is the basis for the derivation of the acceptance criteria in a Metropolis Monte Carlo scheme. If the system contains many species, then Equation (3-3) can be written for each species and the partition function of the total system can be calculated as the multiplication of the partition function of the specie-subsystems according to (Frenkel and Smit 2001).

$$Q_T = \prod_i Q_i \tag{3-4}$$

Thus, for a grand-canonical ensemble of a system with *x* species, equations (3-3) and (3-4) combined lead to the general expression of its probability density:

$$\psi_{\mu VT} \propto \prod_{i=1}^{x}\left[\left(\frac{V^{N_i}}{N_i!}\right)\frac{\exp(\beta\mu N_i)}{\Lambda^{3N_i}}\right]\exp\left[-\beta U_{(s^N)}\right] \tag{3-5}$$

The derivation of the corresponding criteria for the different scenarios becomes then just a matter of relating the probability density of the system at a new *(n)* microstate with respect to that in the old *(o)* microstate (Markov chain) for the specific move that is been considered.

Standard, specific trials for this ensemble are insertion/deletion of molecules as well as their displacement (translation and/or rotation) within the simulation volume. When mixtures are present, then it is possible to combine the deletion of a molecule from species *a* with the creation of a molecule from species *b* into what is known as a 'swap' trial. The acceptance criteria for each of these trials in the Metropolis Monte Carlo scheme have been derived in the literature (Frenkel and Smit 2001), and in their derivation it is useful to consider the relation between the chemical potential of a specie and its fugacity f_i (Hill 1956).

$$\lambda = \exp\left(\beta\mu_i\right) = \beta\Lambda^3 f_i \qquad \textbf{(3-6)}$$

The translation/rotation of a molecule within the volume of the system leads to an acceptance criterion equivalent to that derived for the canonical ensemble, Equation (2-14), which is reasonable since during this trial the number of molecules remains constant. The insertion of a molecule of type *i* (*i* being either species) means the probability density feels a disturbance in N_i as well as in the total energy of the system as described by,

$$acc(o \to n) = \left\{1, \beta f_i \left(\frac{V}{N+1}\right) \exp\left[-\beta\left(\Delta U_{\left(s^N\right)}\right)\right]\right\} \qquad \textbf{(3-7)}$$

where ΔU is the energy of the new configuration minus that of the old configuration.

Physically, this criterion states that the system is looking for its thermodynamic equilibrium (i.e. it is minimising the free energy of the system, which in this case is the Gibbs free energy), which can be seen by examining the Boltzmann factor. Also,

Equation (3-7) can be macroscopically interpreted since the *(V/N)* relation can be seen as the inverse density, indicating that high density states make it difficult for new particles to access the system, while the βf_i term implies higher temperatures make it difficult for molecules to be inserted (which can be related to the higher kinetic energy of the molecules inside, ergo larger mean free path – larger collisions) and higher fugacities favour the insertions (fugacity is a pressure corrected by non-ideal interactions). This is reasonable since it means the system equilibrates at higher chemical potentials.

For the simulations then it is sufficient to set a unit cell of known volume V (fixed) and specify P and T, from which the fugacity needed for the acceptance criteria can be calculated by means of an equation of state (EOS). For this purpose the cubic EOS of Peng-Robinson was used (Sandler 1999, van Wylen and Sonntag 1986).

In the deletion trial the new configuration has lost a molecule and, based on the discussion presented above for the insertion of a molecule we would expect deletion to be favoured by lower energy configurations, higher densities and temperatures, and lower fugacities (this implies the molecules want to change phase). Indeed, this is read from the acceptance criterion for the deletion trial – Equation (3-8).

$$acc(o \rightarrow n) = \left\{1, \frac{1}{\beta f_i}\left(\frac{N_i}{V}\right)\exp\left[-\beta \Delta U_{(s^N)}\right]\right\} \qquad \textbf{(3-8)}$$

When mixtures are present the simulations can be carried out with the trials mentioned above, but in order to achieve equilibration faster and avoid that microstates remain in metastable configurations for too long it is convenient to introduce an additional trial: the swap. This is a combination of deletion (of a molecule from species i) and insertion (of a molecule from species j) and the corresponding acceptance criterion evidences just that (compare Equations (3-7) and (3-8) with Equation (3-9)).

$$acc(o \to n) = \min\left\{1, \left(\frac{f_j}{f_i}\right)\left(\frac{N_i}{N_j + 1}\right)\exp\left[-\beta\Delta U_{(s^N)}\right]\right\} \quad \textbf{(3-9)}$$

3.2.2. Simulation conditions

Although the system under study consists of a few hundred molecules it must be kept in mind that it represents a real – macroscopic – thermodynamic system. In other words, the simulation cell chosen to represent a system of infinite molecules is always too small and that implies that the boundary conditions chosen for it may have an effect on the properties that will be calculated (Frenkel and Smit 2001). The best way to overcome this issue is to assume that infinite identical cells surround the simulation cell under study: periodic boundary conditions. This means that any molecule in the simulation cell can also interact with molecules in neighbouring cells as long as they are within the interaction cut-off distance.

The adsorbent molecules in the simulation cell occupy space, thus rendering part of the unit-cell volume unavailable for insertions since any trial attempting an insertion within the solid wall would be rejected. To avoid too many rejections and therefore improve the efficiency of the Monte Carlo scheme a volume-bias insertion technique was adopted. Figure 3-4 depicts a simplified 2D version of the technique.

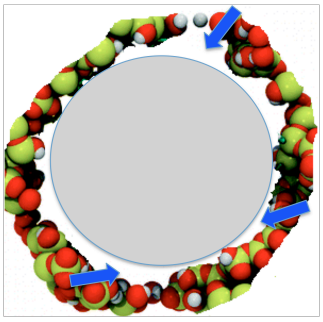

Figure 3-4: Volume bias: the grey area indicates where insertion/deletion can take place, the blue arrows point at the white area (nooks and crannies) accessible to the adsorbate molecules by translation.

The microscopic balance is obeyed since insertions and deletions can only take place on the specified volume (which in this work is equivalent to the volume of a sphere determined by the mean radius of the pore). Translation moves (which are not bounded by the volume bias) provide the adsorbate molecules with access to the nooks and crannies of the pore wall as well as to the accessible volume due to pore-shape irregularities.

At the end of the simulations, a statistical analysis of the number of molecules through mean and variance leads to the amount adsorbed in the system. Here it must be mentioned that, just as the experimental system needs time to equilibrate upon changes in the environment, the microscopic system needs a – sufficiently – large number of configurations (a priori unknown) before reaching equilibrium, this is known as the equilibration stage. The values relevant for the statistical study are thus taken after the equilibration stage has been completed (sampling stage), and for a number of configurations large enough so that the statistical calculations are meaningful.

3.2.3. Intermolecular potentials

In order to estimate the potential energy, U, in a given system it is necessary to know and account for all the attraction/repulsion interactions that take place in it, whether they are short or long ranged in nature, and it will be assumed that they occur only between pairs of molecules. Molecules are represented by bond lengths and angles that give the spatial location for their charges and atoms (which are the location of the LJ interaction sites). These are reported in the literature and they provide the means for calculating interaction distances, thus allowing the quantification of the potential energy.

To represent the dispersion energy the potential of Lennard-Jones was used. Equation (3-10) shows the LJ potential for the interaction of all LJ sites (i) with all other LJ sites (j) [for $j \neq i$]. This potential has two parameters – σ, or hard-sphere

diameter, and ε, or potential depth – which have been reported for many molecules in the literature. The term to the power of 12 accounts for the repulsion of the molecules while that to the power of 6 accounts for attractions. It is clear then that repulsion prevails at very short distances, but it is the attraction between molecules that becomes more significant as the distance between them increases.

$$U_{LJ} = \sum_{i=1}^{N-1} \sum_{j=i+1}^{N} 4\varepsilon_{ij} \left[\left(\frac{\sigma_{ij}}{r_{ij}} \right)^{12} - \left(\frac{\sigma_{ij}}{r_{ij}} \right)^{6} \right] \quad \textbf{(3-10)}$$

When the LJ interaction occurs between atoms of different nature then the Lorentz-Berthelot combining rules [Equation (3-11)] are applied.

$$\sigma_{ij} = \frac{1}{2}\left(\sigma_{ii} + \sigma_{jj}\right) \quad \textbf{(3-11)}$$
$$\varepsilon_{ij} = \left(\varepsilon_{ii}\varepsilon_{jj}\right)^{1/2}$$

Long-ranged Coulombic interactions are calculated through Equation (3-12), where ε_o is the electric constant (8.854187×10^{-12} F/m) and q_i are the charges involved, by means of the Ewald summation technique (Frenkel and Smit 2001).

$$U_{Coul} = \sum_{i=1}^{N_q} \sum_{j=i+1}^{N_q} \frac{q_i q_j}{4\pi\varepsilon_o r_{ij}} \quad \textbf{(3-12)}$$

So far the intermolecular interactions have been described, but molecules are entities consisting on more than just one atom, and these bonded atoms are spatially arranged so that they are positioned at characteristic distances from each other determined by (a) a preferred bond-length and (b) a bond-angle, both contributing to minimise stress on the molecule due to intramolecular forces. The OPLS force field, which is used to represent molecule interactions, accounts for these forces [(Jorgensen, Madura and Swenson 1984, Jorgensen, Briggs and Contreras 1990), (Jorgensen, Maxwell and TiradoRives 1996)] through the following equations

[**(3-13)** to (3-15)], where r_{ij}^{o} is the equilibrium bond-length between atoms *i* and *j*, and θ_{ijk}^{o} is the equilibrium bond-angle defined between atoms *i,j,k* and ϕ is the dihedral angle which defines the torsional stress in the molecule. The constants involved have been reported (Jorgensen et al. 1996) for many molecules.

$$U_{str} = K_{str}\left(r_{ij} - r_{ij}^{o}\right)^{2} \quad \textbf{(3-13)}$$

$$U_{bend} = K_{bend}\left(\theta_{ijk} - \theta_{ijk}^{o}\right)^{2} \quad \textbf{(3-14)}$$

$$U_{tor} = K_{o} + \frac{K_1}{2}\left[1+\cos\phi\right] + \frac{K_2}{2}\left[1+\cos 2\phi\right] + \frac{K_3}{2}\left[1+\cos 3\phi\right] \quad \textbf{(3-15)}$$

Finally, for very large chain-molecules – those where at least one atom is farther than three bonds from another atom in the same molecule – the LJ and Coulombic 1-n interactions (where n=4,5,6…) need to be taken into account through Equations [(3-10) to (3-12)].

3.2.4. Silica-Wall representation

The siliceous walls making up the framework that sustains the pore network in mesoporous silicas are composed of four types of atoms: silicon, hydrogen, non-bonding oxygen atoms (nbO) and bonding oxygen atoms (bO). Their LJ parameters and Coulombic charges have been reported for MCM-41 (Düren 2002, Schumacher et al. 2006b) and are presented in Table 3-1.

It is assumed that the wall-atoms do not move (their positions remain fixed throughout the simulation), and based on the fact that oxygen molecules always surround the silicon atoms the silicon-adsorbate interactions are not taken into account explicitly (Bezus et al. 1978) (Yun et al. 2002) but rather are incorporated into the LJ parameters for the oxygen sites. The same is true for the silanol groups, where the oxygen LJ site accounts for the LJ contribution of the hydrogens. Furthermore since the hydrogen atom is small and close to the oxygen atom, the

hard-sphere LJ parameter (σ_i) for the silanol oxygen takes into account that of the hydrogen.

Table 3-1: Lennard-Jones and charges for the silica-wall interaction sites.

Wall-Site	ε_i/k_b [K]	σ_i [Å]	q_i [e_o]	Ref
Si	0.0	0.0	1.28050	(Schumacher et al. 2006a)
bO	185.0	2.708	-0.640250	
nbO	185.0	3.000	-0.526125	
H	0.0	0.0	+0.20600	

Both the silicon and the hydrogen atoms have explicit contributions to the Coulombic interactions through their point charges. The real material is neutral, and so must be the unit-cell used for the GCMC simulations. For this reason the GCMC (in house) code checks the neutrality of the cell and makes small adjustments to the charges reported in Table 3-1 if small variations (up to 10 %) are found. The adjustment consists in normalizing the charges by knowing the total positive charges T_p and the total negative charges T_n and using the following equations:

$$T_p = \sum q^+ \quad , \quad T_n = \sum q^- \quad , \quad f = \sqrt{\frac{T_p}{T_n}} \qquad \textbf{(3-16)}$$

$$q^+_{i,new} = \frac{q^+_i}{f}$$

$$q^-_{i,new} = f * q^-_i$$

Further attention is paid in Section 3.8 to check the transferability of the potential depth (ε) for the combined Si/O/H Lennard-Jones model because it has a significant impact in the adsorption within the Henry region (at low pressures) and its value in Table 3-1 (and used for the adsorption calculations presented below) was obtained through optimization for MCM-41(Düren 2002) adsorption predictions.

It has to be noted that the porosity of the model material (the void volume over the total volume of the system) corresponds to that of a perfect structure, i.e. it has no defects. This is unlikely to be the case on the experimental sample, since due to their

amorphous nature they are prone to exhibit structural defects. These defects lead to inaccessible void volumes that reduce experimental adsorption. For this reason when comparing experimental isotherms to those predicted through simulations it is common that the simulated isotherm over-predicts adsorption throughout the pressure range. To make the simulations account for this 'lost-porosity', the capacities of the simulated (N^S) and the experimental (N^E) pores are compared at a point where the adsorption isotherm shows saturation, defining an adjusting or scaling factor:

$$F = \frac{N^E}{N^S} \qquad \textbf{(3-17)}$$

Unless otherwise specified, the scaling factor is determined at the highest available pressure, which allows for a direct comparison between the - now overlapping - simulated and experimental curves.

3.3. Helium isotherms

In Chapter 2 it was mentioned that the pore volume of the material is calculated by helium pycnometry, and details were provided on how this calculations are made. Here we provide details on the helium adsorption simulations, since they are used to characterise the pore models, as well as how V_{He} can be used to compare adsorption results from simulations to those obtained experimentally.

We used T = 263 K since it is in the range of temperatures used for other adsorbates although experimentally this would be carried out at ambient temperature. Since helium is considered an ideal non-adsorbing gas, the temperature thus selected does not have an impact on the final volume calculations. Helium molecules are modelled as a single LJ site (Talu and Myers 2001) with parameters σ = 2.64 Å and ε/k_b = 10.9 K, and its bulk critical properties are taken from the NIST physical

reference data (Linstrom and Mallard 2003) (T_c = 5.1953 K, P_c = 0.22746 MPa and acentric factor -0.382).

Adsorption simulations report what is known as the absolute adsorption, N_{abs} in Equation (3-18). The absolute adsorption is the total amount of adsorbate molecules trapped in the solid either on the porous surface or as part of the bulk fluid occupying the pore volume - as it would normally do at (*T,P*) without being confined in a solid. In order to transform the absolute amount adsorbed into the excess amount adsorbed measured experimentally N_{ex} (which is the adsorbate retained in the solid due to the solid-fluid interactions) Equation (3-18) is used. (Myers and Monson 2002)

$$N_{ex} = N_{abs} - \rho_{bulk} V_{He} N_{av} \qquad \textbf{(3-18)}$$

This equation introduces a correction term that removes the number of adsorbate molecules estimated to be in the gas phase of the unconfined bulk-fluid.

The calculation of the excess amount adsorbed must be standardised so the pore volume is calculated at the same reference conditions for every model, since this calculation depends on the size of the adsorbate molecule, as well as on the temperature and pressure conditions (Myers and Monson 2002). To this end a linear regression of the helium adsorption points passing through the origin (since at *zero* pressure the ideal gas law predicts zero loading) is carried out, and a constant relation between the pressure and helium loading N_{He} is obtained (Figure 3-5). Once this is done, the pressure point at 12 bar was selected to calculate the desired pore volume. The linear regression is necessary because the data points from the simulation are statistical values, and small deviations introduce errors in the void volume estimation.

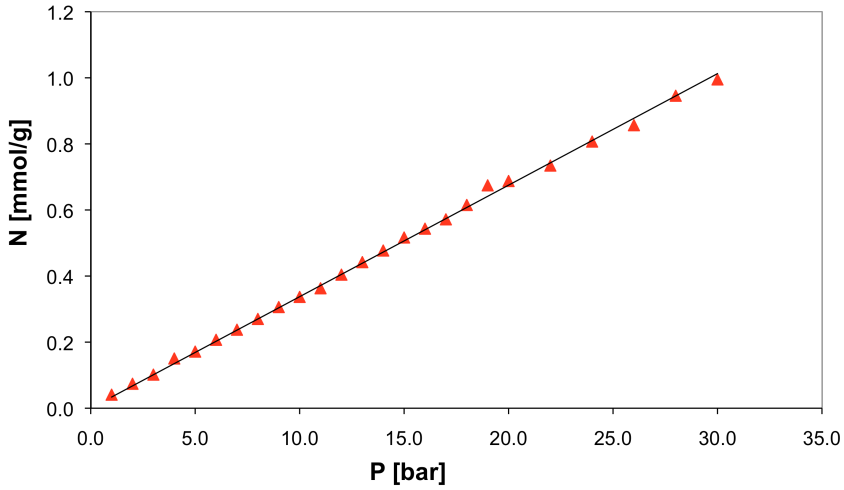

Figure 3-5: Helium isotherm at 263 K for the model STAC-1^E. The red triangles are the absolute adsorption results obtained through GCMC simulations. The black line is the linear fit going through the origin.

3.4. Nitrogen isotherms

Nitrogen isotherms on SBA-2/STAC-1 samples calcined at 550 °C reportedly (Perez-Mendoza et al. 2004a) exhibit a type IV (Figure 3-2) behaviour. In this thesis nitrogen molecules are modelled by two different sets of parameters, see Table 3-2. Since model *A* has no charges and model *B* does, they will help to illustrate the importance of the Coulombic interactions in the materials being studied.

Model *N2-A* is a simplified model that attempts to mimic all the nitrogen interactions through 2LJ sites, while model *N2-B* is more accurate and consists on 2LJ sites with point charges that are balanced by a ghost charge in the centre of mass of the molecule (Q) to account for the nitrogen quadrupole. Nitrogen critical properties are read from NIST (Linstrom and Mallard 2003): T_c = 126.192 K, P_c = 3.3958 MPa and the acentric factor is 0.0372.

Table 3-2: Models for nitrogen used in this work.

Model	Site	σ_i [Å]	ε_i/k_b [K]	q_i [e_o]	Bond length [Å]	Ref
N2-A	N	3.31	37.3	0.0		(Murthy et al. 1980)
	N	3.31	37.3	0.0	1.090	(Schumacher et al. 2006b)
N2-B	Q	0.0	0.0	+1.0950		(Stoll, Vrabec and Hasse 2003)
	N	3.3211	34.897	-0.5475		
	N	3.3211	34.897	-0.5475	1.0464	(Schumacher et al. 2006a)

Figure 3-6 illustrates the predictions for an N_2 isotherm at 77 K for both adsorbate-models confined in one of the STAC-1 model pores (model J). Note that the experimental isotherm looks like a type IV isotherm without hysteresis. The predictions obtained are identical in the Henry region. Since at very low pressures adsorbate molecules are close to the wall and solid-fluid interactions dominate the process and at high pressures it is the fluid-fluid interactions that dominates, it is clear that the N2-A model captures the main physical driving forces of the process well; however, the absence of Coulombic interactions seems to be an important drawback when predicting pore filling (at medium range pressures), where the solid-fluid and fluid-fluid interactions are comparable.

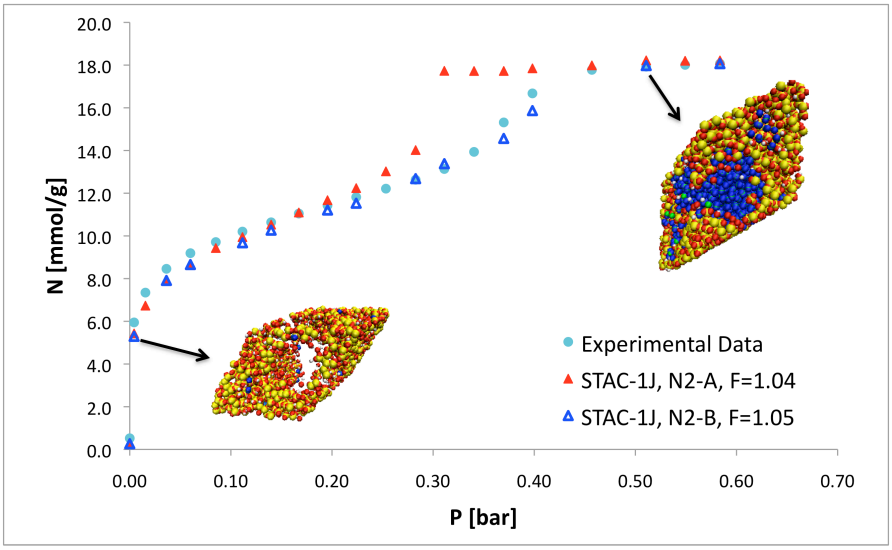

Figure 3-6: N_2 predicted isotherm at 77 K using the model STAC-1^J with the two adsorbate-models proposed above. The snapshots show the trapped nitrogen molecules (blue) in the adsorbent model at low and high pressures.

The remarkable similarity between the simulated and experimental results shown in Figure 3-6 are a good evidence of the realistic nature of the pore model been used, and furthermore, the adjusting factors *F* indicates that the pore size is representative of the experimental sample. Nitrogen adsorption on SBA-2 has been modelled before (Perez-Mendoza et al. 2004b) by means of a pore size distribution model with contributions from smooth spheres and channels. The fitted PSD was capable of representing the experimental data, but in this work we proved that a single pore size with a realistically rough surface (rather than smooth) is a better representation of the material (as it leads to good predictions). Moreover, this also proves that the channels used for the PSD are an artifice, since the pore models provided in this work clearly show that the connections are not channels but window-like.

It is worth mentioning that the adjusting factors are slightly larger than one (~5 %) contrary to the initial expectations. This can be seen as an indication that the model pore is slightly smaller than the pores of the experimental sample. However, using the nitrogen model N2-B the adsorption predictions with the model pore STAC-1^J are very accurate. Despite a 50 % under-prediction for the lowest pressure

point, the average relative error throughout the isotherm is 3.33 %, and for pressures above 4.30×10^{-3} bar the relative error never exceeds 10 %.

It is important to underline at this point that, while for the nitrogen model without charges the silanol groups (-*OH*) on the pore wall were left rigid, for the simulations with the charged nitrogen model they were allowed to move. The impact of this subtlety is mainly at low pressures and, as long as the silanol groups are allowed to move for a sufficiently large number of trials at low pressure points, after that they can be frozen in the interest of simulation speed (this is equivalent to saying that they have found their position of minimum energy respect to the first layer of adsorbed molecules and subsequent layers will not disturb them any more).

As was mentioned at the beginning of the chapter, there is no information in the literature regarding the experimental conditions that would favour the synthesis of SBA-2 over STAC-1 (or the other way around), nor there is any mention on this issue for the sample used to obtain the experimental isotherms (Perez-Mendoza et al. 2004b). From the results provided thus far it follows that the STAC-1 pore model suffices to get good adsorption predictions on that sample, but to further illustrate the point Figure 3-7 is presented.

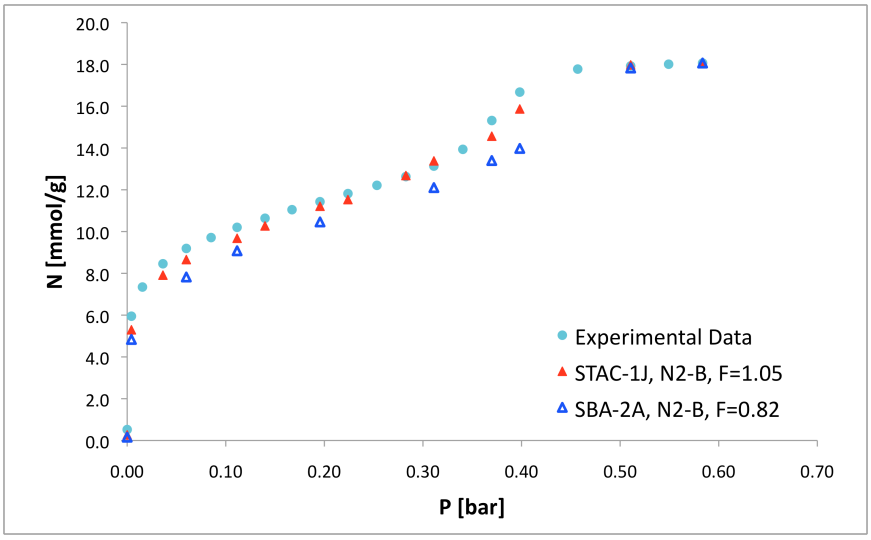

Figure 3-7: Predicted N_2 isotherm at 77 K by means of the models SBA-2^A and STAC-1^J using adsorbate model N2-B.

While the overall shape of the isotherm is consistent for both model pores, it is apparent that the STAC-1^{J} model pore gives better predictions than the SBA-2^{A}. This however is not related to the pore models but rather to their pore size: while the STAC-1^{J} model pore has a mean radius of 22.95 Å the pore sizes on the SBA-2^{A} model pore are 23.81 Å and 24.49 Å. Larger pores means weaker solid-fluid interactions leading to less fluid loading at low pressures and they are also associated to pore filling transitions at higher pressures, both features being evident in Figure 3-7. Further indication of this is provided by the adjusting factor *F*, which is smaller for the SBA-2^{A} model pore.

Since both model pores give good adsorption predictions it does not matter which one is used in the following sections. This was, to some extent, expected given that from the simulated synthesis of the materials it was clear that their main difference is in the pore connectivity: size, number and direction of the connections. The size of the connections is related to the pore size (Gonzalez 2005) and their number and direction are important features on tortuosity and diffusion through the porous media but not in the actual adsorption loading. Moreover, the kMC simulations showed that these connections are like 'windows', that is channels of length zero, which effectively means that their overall contribution to adsorption is negligible compared to that of the spherical cavities.

Thus, most of the adsorption simulation presented in this chapter will be presented for the STAC-1 model pores, since their lower number of wall atoms and their wider range of pore models means they provide flexibility for discussions as well as faster adsorption computational times. Nonetheless, some isotherms achieved with the SBA-2^{A} model pore are presented for comparison purposes.

3.4.1. Pore Size Distribution (PSD) for STAC-1 models

Although silica materials like MCM-41 and SBA-2 show a predominant pore size, in reality this size is the mean of a narrow distribution [(Huo et al. 1996),

(Perez-Mendoza et al. 2004a) and (Kim and Stucky 2000)]. This means that it should be possible to improve adsorption predictions by means of a PSD representation in the same way as it was reported for smooth ideal pores [(Perez-Mendoza et al. 2004a) and (Perez-Mendoza et al. 2004b)].

Using a PSD approach means looking at the isotherm as the sum of the adsorption contribution from all the pores sizes within the adsorbent, where the contribution from the smallest pores is relevant at low pressures and as the pressure increases that of the larger pores becomes predominant (since the smallest ones will be filled). The PSD can be strictly calculated by mathematically solving Equation (3-19), called the 'adsorption integral equation' (AIE) (Davies, Seaton and Vassiliadis 1999). In it, $f_{(w)}$ is the 'weight' distribution to be found, N_a is the experimental amount adsorbed at (T,P), and $\rho_{(T,P,w)}$ is the amount adsorbed by a single pore of size w at the same (T,P) conditions.

$$N_a(T,P) = \int_{}^{\infty} f_{(w)} \rho_{(T,P,w)} dw \qquad \textbf{(3-19)}$$

One method to acquire the PSD is based on a discrete representation of pore sizes (Davies et al. 1999), this requires several steps: first independent GCMC simulations at (T,P) for a significant number of pores in a wide size range must be run to find $\rho_{(T,P,w)}$; then, a system of equations (determined by the number of experimental pressure points) has to be solved to find an adequate PSD for the system being considered. This is a conditional problem where there may or may not be a solution, or there may be an infinite number of solutions depending on the total number of pressure points and the number of pore sizes being considered. Therefore, solving the PSD means using the experimental isotherm as a target function while using the distribution as a pool of fitting parameters.

Since many model pores were created for STAC-1, and the SBA-2 pore model provides itself the contribution of two pore sizes, it is for the STAC-1 models (A through S) for which the PSD approach was applied. Nonetheless the model pores

available are not evenly distributed on a sufficiently wide pore size range, they have different roughness, and even different wall densities. Thus, we called the obtained pore size distribution a quasi-PSD. Also, as a first approach the nitrogen model N2-A was used to avoid using excessive computational time.

For the reasons above mentioned, rather than using a strict solution of Equation (3-19) to find the parameters it was deemed appropriate to use a least-squares numerical optimization (by means of the Excel solver). The solution presented in Figure 3-8 indicates that among the pool of model pores available only three of them were appropriate for the calculation of the fitted nitrogen isotherm. Two of the selected model pores have similar size while the third is considerably smaller, this point towards a bimodal distribution that was not a priori expected from experimental characterisation. The previously reported research on a PSD to describe SBA-2 (Perez-Mendoza et al. 2004a) contemplated a bimodal distribution, but under the artifice of considering the system as spheres connected by cylindrical channels. The peaks for their distribution were around 23.5 Å and 5 Å respectively.

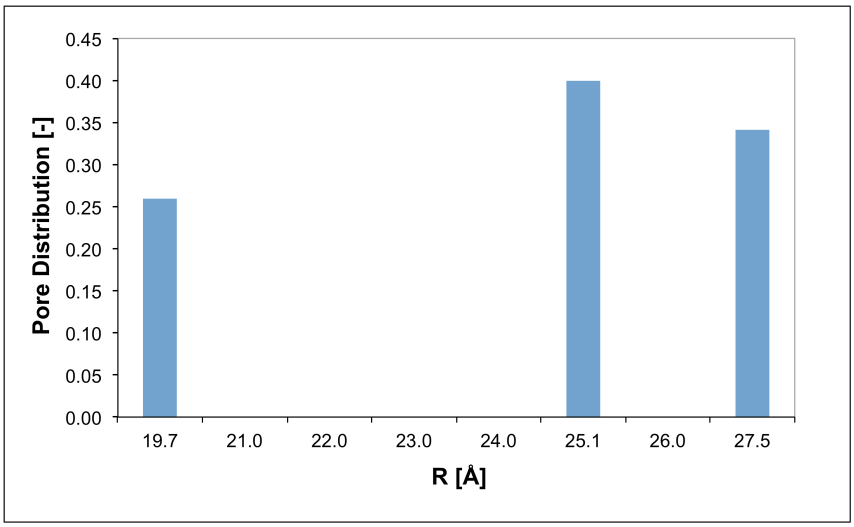

Figure 3-8: PSD calculated for the collection of STAC-1 pore models.

Figure 3-9 shows the predicted isotherm with the PSD found in the way described above. The STAC-1^{O} model pore (with a pore radius of ~25.1 Å) is the main contributor to the final adsorption because its own isotherm is already close to the experimental one. Since this model underestimates nitrogen loading at low

pressures the PSD includes a smaller model pore (STAC-1^D) to compensate (smaller pores, stronger solid-fluid interactions). The smaller pore though leads to earlier pore filling than in the experimental sample, and to minimise this error the larger STAC-1^N model pore is taken into account (pore filling occurs at higher pressures for larger pores).

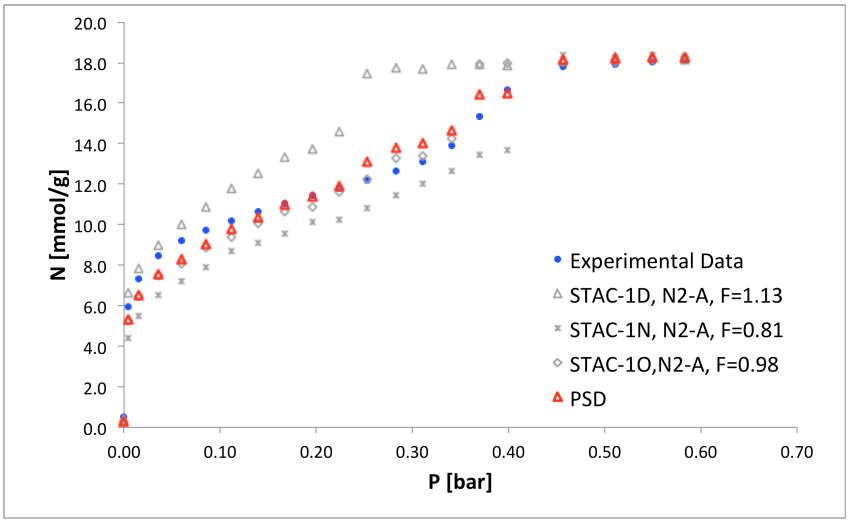

Figure 3-9: N_2 Isotherm predictions with the STAC-1 pore model PSD.

In summary, it can be seen that although an overall minimisation of the errors in the isotherm predictions is achieved (the absolute average relative error now being 2.7 % rather than 9.4 % for the single STAC-1^O model) but on the expense of using an unrealistic bimodal representation of the pore size distribution in the material. For future works it may be that using the adsorbate model N2-B improve the calculated PSD, but then more models with pore sizes evenly spaced around the mean pore size of the sample are needed. Nevertheless, the results presented here are comparable to those presented by Perez-Mendoza and co-workers (Perez-Mendoza et al. 2004b) despite the under-prediction observed at low pressures.

3.5. Methane isotherms

Methane isotherms in STAC-1 and SBA-2 materials are Type-I isotherms (Figure 3-2). Methane is a small molecule for which Lennard-Jones interactions are the ones to be taken into account, since it is a non-polar substance. Due to its size it is sensitive to the nooks and crannies on the pore wall. Methane molecules are simulated with a united-atom force field approximation (in this case, UA-OPLS), which means that the hydrogens are not considered explicitly but rather the whole methane molecule is modelled as one LJ site. The UA-OPLS force field for methane (Jorgensen et al. 1996) uses the following parameters σ = 3.73 Å and ε/k_b = 147.9 K. Methane critical properties as reported in NIST (Linstrom and Mallard 2003) are T_c = 190.5 Å and P_c = 4.61 MPa, and it has an acentric factor of 8.00×10^{-3}.

Experimental adsorption isotherms for methane were available at four temperatures: 263 K, 273 K, 283 K, and 293 K (Perez-Mendoza 2007-2010). Figure 3-10 shows the experimental isotherm at 263 K and predictions by means of the STAC-1^J model pore, which is representative of the predictions obtained with other model pores as well as with the SBA-2 pore model. Although the predictions are very good, there is an evident overprediction at low-medium pressures. The isotherms at other temperatures are not presented here since they exhibit a similar behaviour, noting though that the higher the temperature the lower the loading and less overprediction is seen.

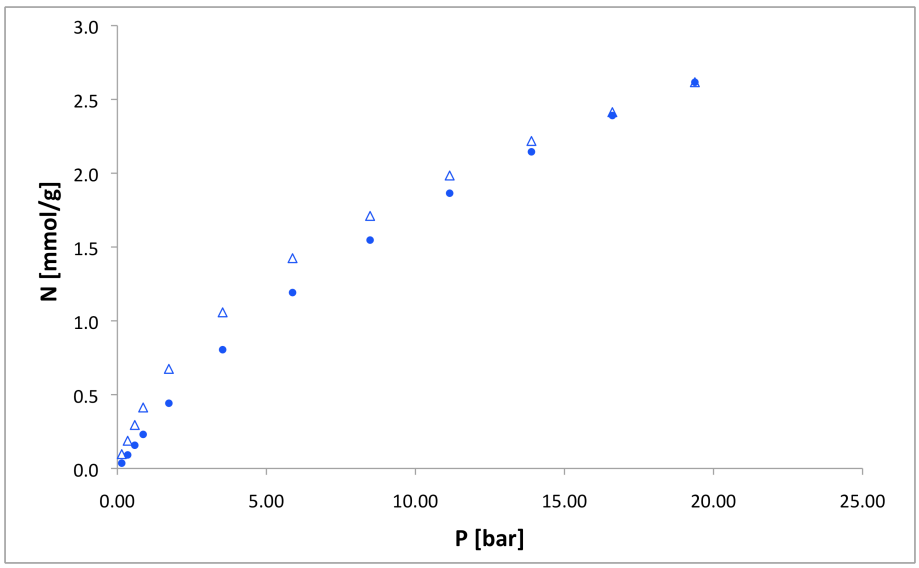

Figure 3-10: Experimental methane isotherms (close circles) and STAC-1^J model pore predictions (open triangles) at 263 K (The adjusting factor is 0.94).

This overprediction at low pressures points towards an excess in the solid-fluid interactions been modelled which may indicate there are more nooks and crannies in the models than in the real material (assuming the LJ parameters for the solid are accurate enough). Note however how in Figure 3-6 nitrogen adsorption is slightly under-predicted. These results are not contradictory but rather complement the information gathered on the realism of the pore models.

Unlike for methane, for nitrogen the contribution of the Coulombic interactions is relevant and the effect of the surface roughness is not as strong since the N_2 molecule is larger (slightly thinner but longer) than the modelled methane molecules. The latter is especially true since the hydrogens linked to the surface oxygens affect the coulombic interaction between the nitrogen and the wall, making the gaps less attractive.

Since the SBA-2^A model has larger pores the scaling factor is lower than that for the STAC-1^J model (Figure 3-11), despite the larger absolute density of the material SBA-2^A (3.29 g/cc versus 3.07 g/cc for STAC-1^J). The fractal dimension (as explained in Chapter 2) is a useful tool to asses this roughness in the model pores and it provides a reasonable explanation for the observed over-predictions. The fractal

dimension for the STAC-1^{J} model is 2.79 while that for the SBA-2^{A} model is 2.70, which means the STAC-1 model pore has rougher walls and thus the slightly larger methane over prediction is with this model pore. Also, from Figure 3-11 it is clear that they are both rougher than the material sample used in the experiments.

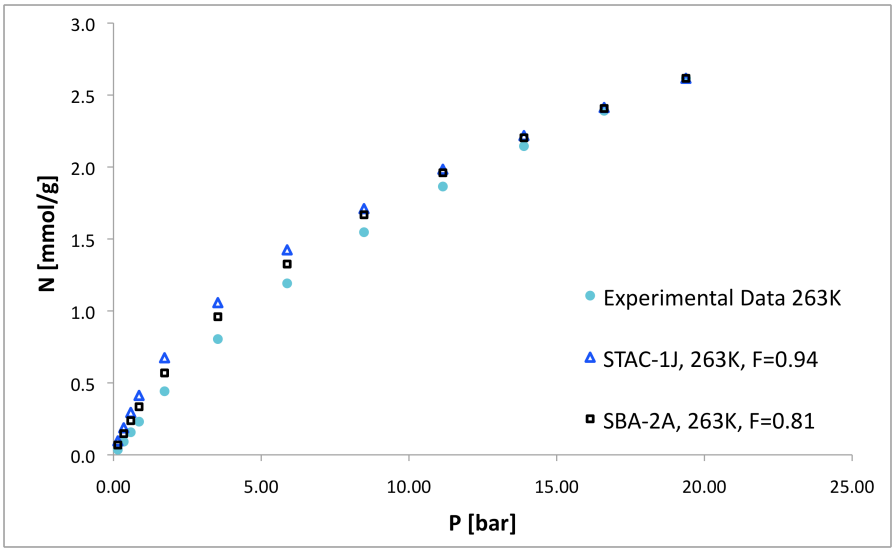

Figure 3-11: Methane adsorption at 263 K. Experimental isotherm and prediction by the model pores STAC-1^{J} and SBA-2^{A}.

Figure 3-12 shows methane molecules trapped in the pore wall nooks and crannies. At low pressures methane molecules are already been lured towards these gaps, which remain a hot spot for methane adsorption throughout the pressure range. These are then preferential adsorption sites.

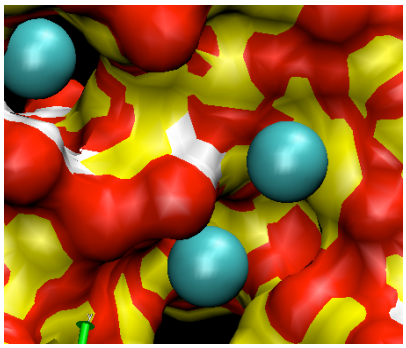

Figure 3-12: Close up of methane molecules (green) encrusted in the pore-wall (oxygen atoms in red, silicon atoms in yellow and hydrogen atoms in white) of model STAC-1^{J} at 263 K.

Figure 3-13 provides further support on the influence of the surface roughness on the over-estimation of methane adsorption. Regardless of the size of the model pores (which is intuitive from the scaling factors reported in the legend) it is evident that there is a variation in the curvature of the predicted isotherms for the STAC-1 models reported. While the fractal dimension of pore J is 2.79 that of pore H is 2.49, and unsurprisingly it is the latter that better predicts methane adsorption (this is true regardless of the adsorption temperature).

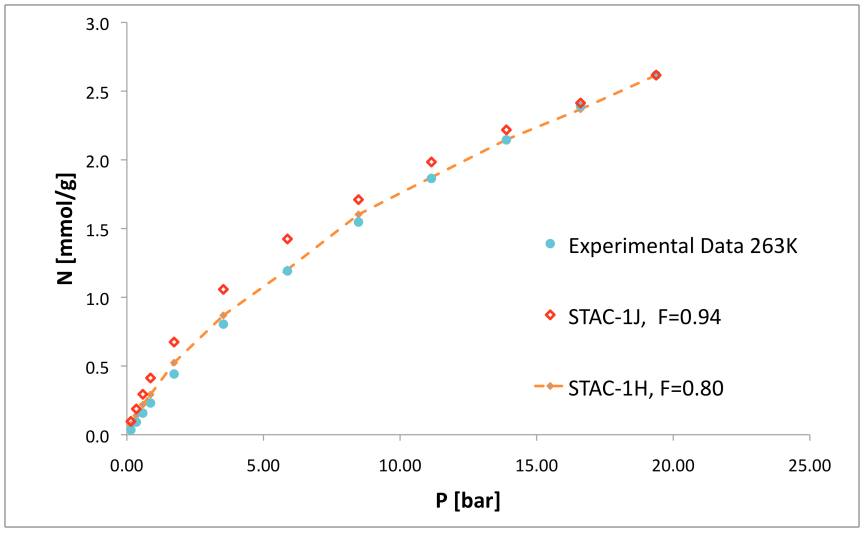

Figure 3-13: Predictions for methane adsorption at 263 K by different STAC-1 model pores (dotted line is a guide to the eye).

The model pore STAC-1^{H} has the largest pore size and the smoothest pore wall of all the models obtained through the kMC simulations. Both factors contribute to weaken the strength of the interactions felt by methane molecules from the pore wall, and this is why the predicted isotherm gets closer to the experimental results. However, it has to be noted that this model has a pore size much larger than that of the experimental sample as can be seen from its high nitrogen under-prediction at low-medium pressures (Figure 3-14).

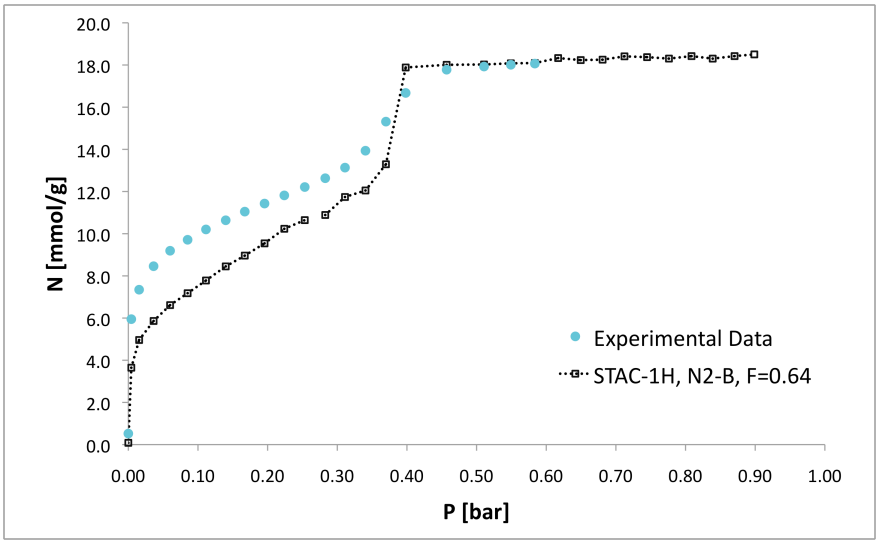

Figure 3-14: Nitrogen isotherm prediction at 77 K with the model pore STAC-1^H (dotted line is a guide to the eye).

3.6. Ethane isotherms

Ethane molecules are simulated as a hydrocarbon chain formed by two CH_3 links separated by a distance of 1.53 Å each one with the same LJ parameters: σ = 3.775 Å and ε = 0.207 kcal/mol (Jorgensen et al. 1996). Its critical properties (from NIST) are T_c = 305.32 K and P_c = 4.872 MPa and it has an acentric factor of 0.099 (Linstrom and Mallard 2003). Although there are experimental data at four temperatures (263 K, 273 K, 283 K and 293 K) available (Perez-Mendoza 2007-2010), the discussions will be based on that for which more experimental points were available (i.e. at 273 K).

It was expected that the predictive capabilities of the models would improve at low pressures since the larger ethane molecules are less likely to be trapped in the gaps on the pore walls, and this is confirmed by looking at Figure 3-15 where low pressures predictions are much better than the ones presented for methane in the previous section. It has to be pointed out that rather than using the final pressure point of the isotherm to calculate the scaling factor the pressure point immediately

before was used; this is because the experimental isotherm at this pressures should be level (the pores should be filled) and the last point seems to indicate otherwise.

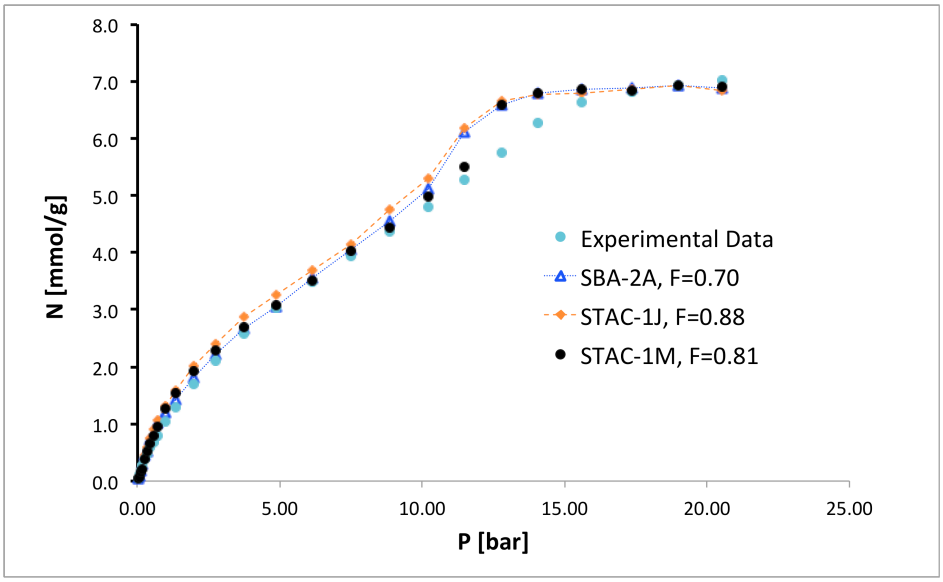

Figure 3-15: Predicting ethane adsorption at 273 K by means of the SBA-2^{A}, STAC-1^{M} and STAC-1^{J} model pores (lines are a guide to the eye).

Predictions with either the STAC-1^{J} or the SBA-2^{A} model pores are equally good, although a slight better representation is achieved with the latter at low-medium pressures probably due its larger pores (evidenced by the presented adjusting factors). It is interesting however that the pore filling point is the same for both pores, showing that this characteristic of the ethane isotherm is not as sensitive as it was for nitrogen (Figure 3-7).

The transition of the adsorbate from the gas-like phase to the liquid-like phase (capillary condensation) occurs at about $P \sim 12$ bar. In this region the predicted loading can differ from experiments up to 15 %, with the pore models predicting pore filling to occur at pressures ~ 3 bar lower than shown experimentally. This point is rather curious given the fact that the pore-models show a very close prediction elsewhere in the pressure range of the isotherm and, furthermore the complex shape of the ethane isotherm (which exhibits an inflexion point around 7 bar) is also appropriately captured. The slightly larger pore size of model STAC-1^{M} (~24.77Å) combined with the lower rugosity (fractal dimension 2.72 rather than 2.79 for STAC-

1^{J}) result in the simulated isotherm been closer to the experimental one at low and medium pressures, though the transition pressure to liquid-like phase is still under-estimated.

The pore walls in the models are again rougher than the ones of the experimental sample and although ethane molecules are less sensitive to this parameter there is still some over-prediction caused by it. The pore size however, besides affecting the total pore capacity it also seems to affect the sharpness in the inflexion exhibited by the modelled isotherms while having a minor impact on the exact pressure where the liquid-like phase is achieved.

Figure 3-16 looks at different ethane isotherms: 263 K and 293 K. The evidence presented supports the models prediction capabilities regardless of the temperature at which adsorption takes place. Slight over-predictions are observed at low pressures for the reasons already explained and, for the isotherm at 263 K, as happened for that at 273 K, the phase transition is under-predicted. The reproducibility of the experimental data by the pore models shows signs of improvement as the temperature increases, just as it did for methane.

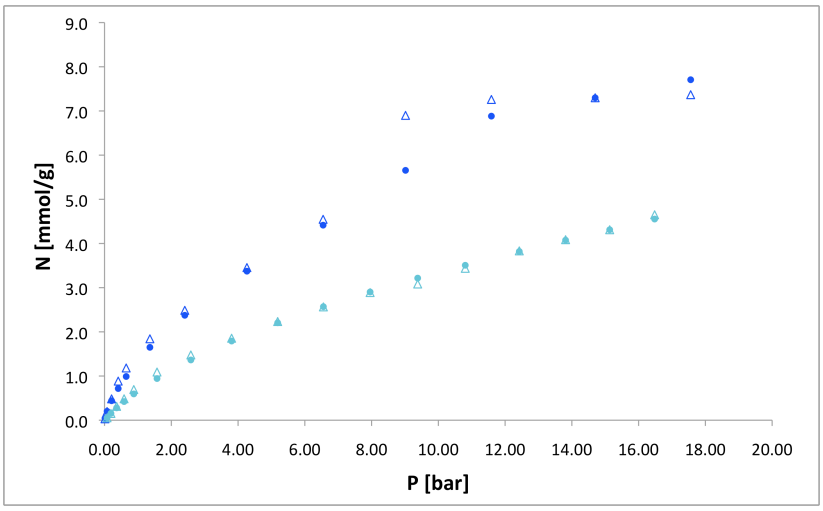

Figure 3-16: Adsorption isotherms of ethane at 263 K (blue) and 293 K (cyan). The closed circles correspond to the experimental data whereas the open triangles are the simulated isotherms (model SBA-2^{A}).

The good predictions achieved by model STAC-1^J for nitrogen adsorption (including the condensation pressure point), and the continuous under-estimation of the phase transition on ethane isotherms are two somewhat contradictory facts. At such high pressures the fluid-fluid interactions are by far more important than the solid-fluid interactions, and the adsorbate model parameters are well documented and tested for. An alternative explanation could be that the equilibration time during the experimental adsorption measurements was not sufficiently long.

Although there is no apparent reason to doubt the experimental data used here, diffusion (which is beyond the scope of this work) in the studied materials is an important parameter to take into account – diffusion normally decrease with loading – as it does with tortuosity and pore network connectivity. A detailed bond percolation analysis of the latter is not possible with the pore models created due to their limited number of pores per unit cell, but these models do give an idea of what might be expected: despite pores being surrounded by 12 other pores in the structure, only about a third are accessible from it.

If we assume that the experimental data is accurate then it is worthwhile attempting to use a pore-size distribution to give better predictions of ethane adsorption. Because there are more experimental points of ethane adsorption at 273 K, this isotherm is selected as the target function for the quasi-PSD.

3.6.1. Using ethane data at 273 K to construct a PSD

Following the same approach described in section 3.4.1 Figure 3-17 presents the PSD achieved by means of the ethane isotherm at 273 K. This time four pores contribute to the final isotherm, STAC-1 models D, E, H and N, although the contribution from model H is minimal. Just as it happened with the nitrogen-PSD a bimodal distribution has been obtained, and for the same reasons stated there this is not a real scenario but rather the result of the mathematical approach to minimise the errors.

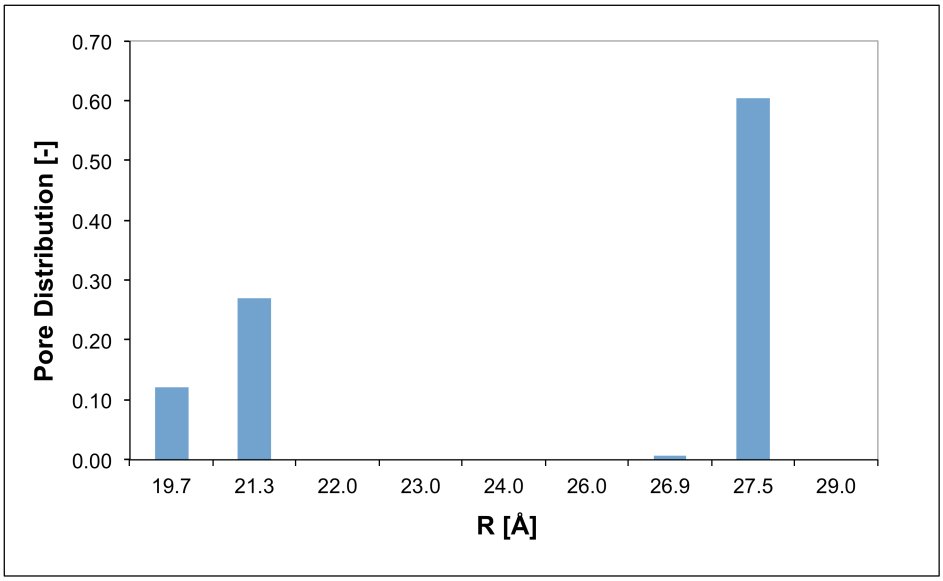

Figure 3-17: PSD calculated based on the ethane isotherm at 273 K.

The fact that this PSD contains different model pores than the PSD obtained with the nitrogen isotherm is hardly relevant since, as it was stated when presenting the PSD approach, the minimisation problem is one that may have infinite solutions. It is remarkable though that both PSD are bimodal as a result of the main contribution from large pores (which under-predict at low/medium pressures) needing to be supported by their smaller counterpart in order to accommodate the shapes of the isotherms – see Figure 3-18.

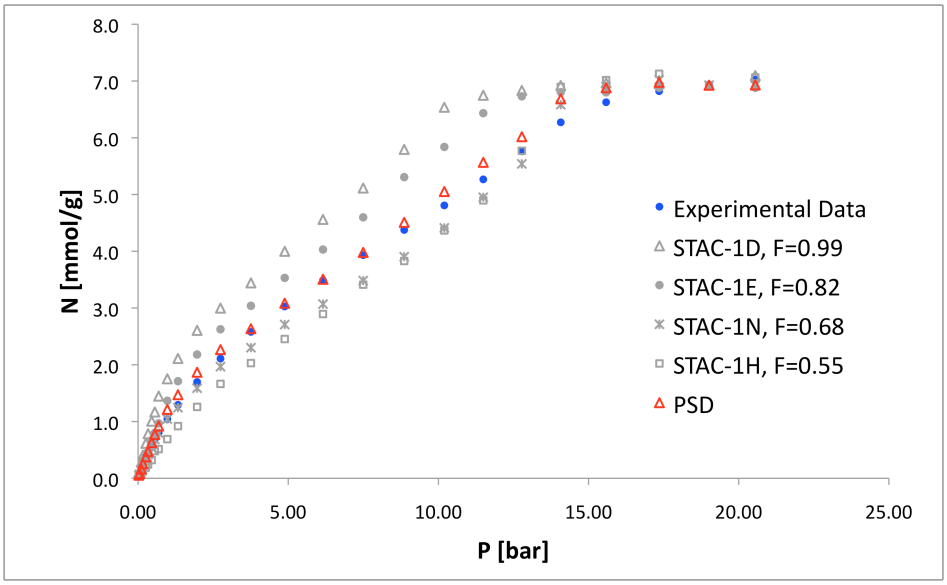

Figure 3-18: PSD predictions for ethane adsorption at 273 K. Shadowed points correspond to the model pores that contribute to the final PSD isotherm.

Figure 3-19 shows the very good agreement achieved by the PSD fitted to the adsorption isotherm of ethane at 273 K and the experimental curve, and more importantly it shows the validity of the PSD for other ethane isotherms: in particular the prediction of ethane adsorption at 293 K is presented as an example and it can be seen that the overall prediction is very good.

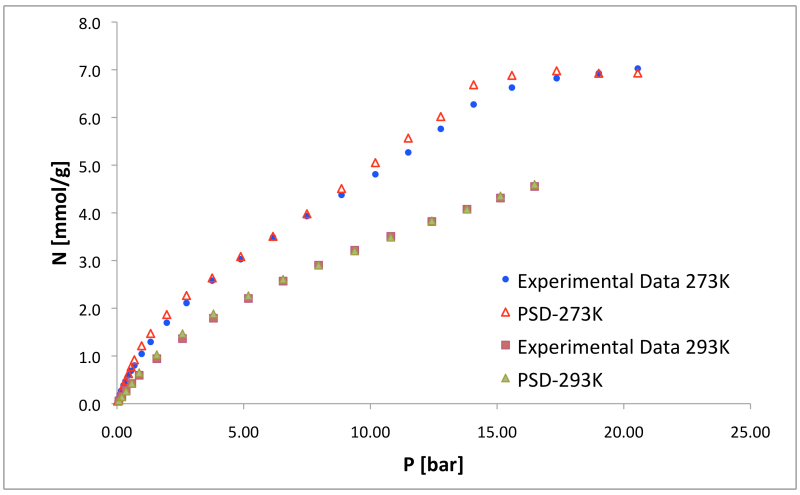

Figure 3-19: Using the calculated PSD by fitting ethane adsorption at 273 K to predict ethane adsorption at 293 K.

Similar improvements were achieved for ethane isotherms at 263 K and 283 K. The fact that the PSD shows cross-isotherm transferability can be linked to the realism of the pore models achieved with the kMC technique. After all, the individual model pores show consistent predictions for adsorbates over the range of temperatures available (for both methane and ethane this has been proved in sections 3.5 and 3.6).

The nitrogen-PSD was calculated using a simplified model for the adsorbate (N2-A), and at that point it was arguable that the choice of the fluid model might have been responsible for the resulting bimodal distribution. However after finding a different bimodal distribution for ethane it is apparent this was not the case. Using the nitrogen-PSD to predict ethane adsorption at 273 K shows that the amount adsorbed predicted by both PSD is similar, with remarkable agreement with the experimental data. The relative errors (Figure 3-20) indicate that both PSD tend to slightly over-predict ethane loading especially at low pressures and close to the phase transition point, and that predictions with the ethane-obtained PSD are slightly better.

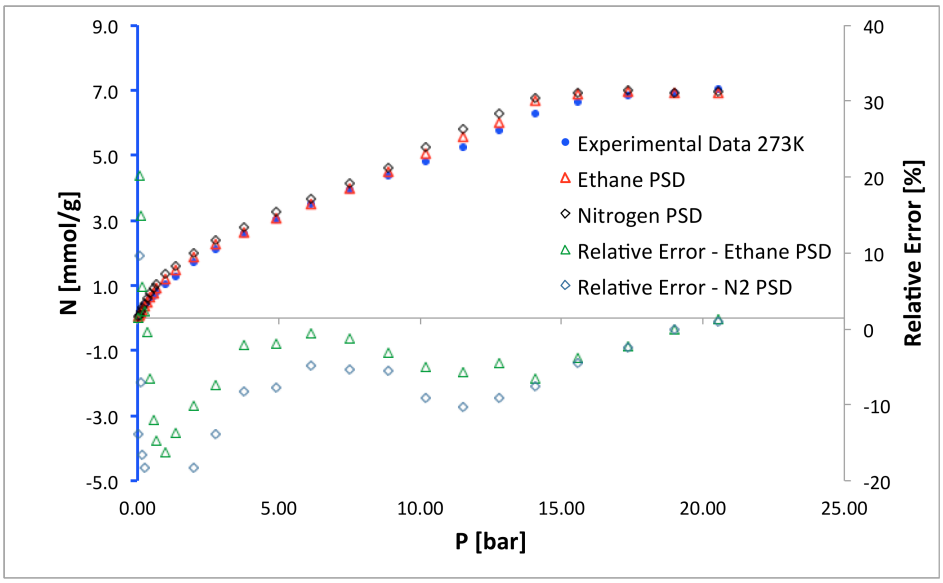

Figure 3-20: Comparison of the predicted ethane isotherm at 273 K by the nitrogen-fitted PSD, and the PSD obtained using the mentioned ethane isotherm as target function.

Since it is true that the pore models are transferable to systems with different adsorbates it follows that the PSD obtained for a given adsorbate should also be valid to others, with one constraint: if the molecules of the adsorbate used to create the PSD are too big, then using that PSD in systems with small adsorbate molecules will result in underpredictions at low pressures since the smaller pores accessible to the latter adsorbate were not so for the original molecules used in the PSD derivation. This constrain is not relevant for the average STAC-1 and SBA-2 pores but it is for their connecting windows as they will limit pore accessibility for larger molecules.

Figure 3-21 shows a comparison between the experimental methane isotherms and the one predicted using the ethane-PSD. The exhibited overprediction is probably a result of the surface roughness of the pore-models used for the PSD. As shown in section 3.5, the model STAC-1^{H} gave the most accurate methane adsorption predictions partly because of the low rugosity of its pore walls compared to other pores. Since the contribution from this model pore to the ethane-PSD is very small this PSD acquires the fractal dimension of the other, rougher, models (D, E and N) instead.

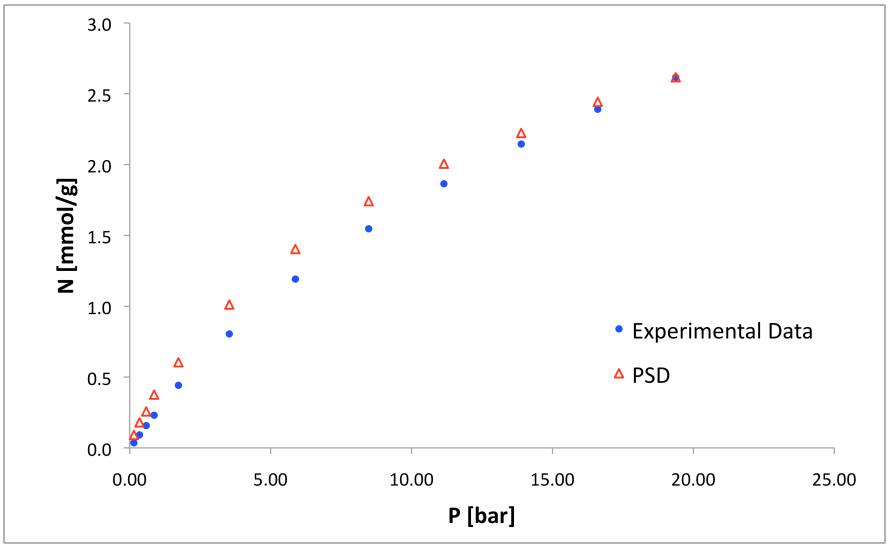

Figure 3-21: Prediction of methane adsorption at 263 K by means of the ethane- calculated PSD.

This result opposes the one presented by Perez-Mendoza and co-workers (Perez-Mendoza et al. 2004a), where their PSD obtained by fitting the ethane data under-

predicts methane adsorption in the entire pressure range, especially at the lower temperatures. In that work they attributed this to the lower accessibility of ethane molecules through the pore network compared to methane (since methane is smaller). Our approach to model the material does not point towards accessibility issues, but rather highlights the relevance of achieving an appropriate representation of the pore roughness in order to get accurate low-pressure predictions. This can be further defended since although ethane molecules are bigger than methane, they are flat and thus their pore network accessibility should be similar.

Figure 3-22 shows the predicted nitrogen isotherm at 77 K using the ethane-PSD, and also presents the isotherms of the individual model pores contributing to the PSD. In general, the low-pressure and high-pressure features are reasonably well captured. This is especially remarkable since a PSD from a system without Coulombic interactions is being used to predict a system where charges are important.

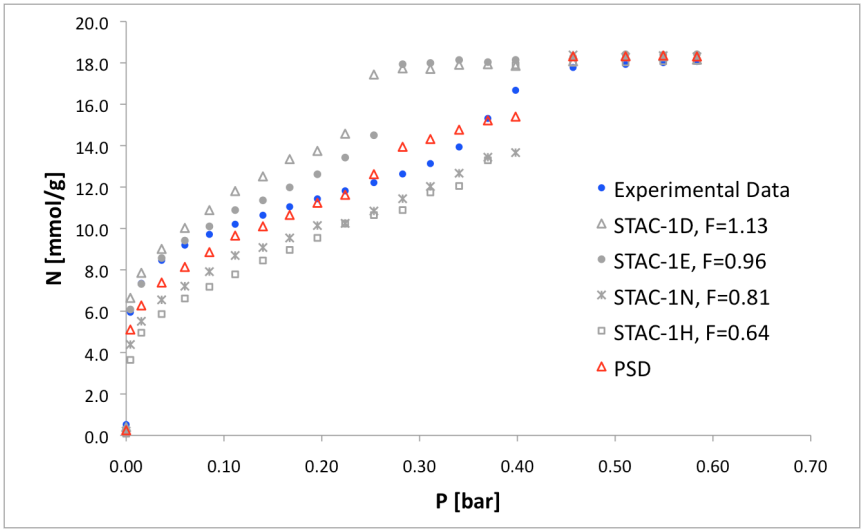

Figure 3-22: Prediction of nitrogen adsorption (model N2-A) at 77 K using the ethane-calculated PSD.

However, the inflexion on the nitrogen adsorption isotherm cannot be captured properly and instead a rather step-like transition is depicted. In the work of Perez-Mendoza and co-workers (Perez-Mendoza et al. 2004a) by using the ethane PSD to predict the nitrogen adsorption they found that although the shape of the isotherm

was captured nitrogen loading was greatly under-predicted throughout the pressure range. Although once again they concluded this was due to accessibility issues, our research indicates that it might also be a case of the PSD not being able to fully capture the interactions in the system.

3.7. Carbon dioxide isotherms

The CO_2 model used for the simulations is presented in Table 3-3. Critical parameters for this fluid were taken from NIST and are: T_c = 304.21 K and P_c = 7.3825 MPa with the acentric factor been 0.224 (Linstrom and Mallard 2003).

In view of a possible application for the materials under study for carbon capture processes it is important that the pore models achieve a high degree of accuracy in the prediction of carbon dioxide adsorption. If this is possible, then the pore models could be used for further material design (i.e. addition of surface groups, see Chapter 4) aiming to enhance the adsorbent-CO_2 interactions and thus tailoring the materials for the desired application.

Table 3-3: CO_2 model used for the simulations.

Site	σ_i [Å]	ε_i/k_b [K]	q_i [e_o]	Bond length [Å]	Ref
C	2.79	29.0	0.6645		(Harris and Yung 1995)
O	3.06	82.0	-0.33225	1.161	
O	3.06	82.0	-0.33225	1.161	

Figure 3-23 presents the experimental CO_2 isotherm at 263 K and predictions using the STAC-1^J and the SBA-2^A models. It can be seen that the predicted isotherms are remarkably close to the experimental data throughout the pressure range indicating that the model pores capture the true nature of the solid-fluid interactions. The scaling factor for the STAC-1^J model indicates that this appears to have a pore-size that matches that of the experimental sample and this relates well to the discussion presented before on the nitrogen adsorption predictions. The SBA-2^A, having slightly larger pores, under-predicts the CO_2 uptake at low/medium pressures

though the condensation pressure is barely distinguishable between the models – as it has been for the predictions of nitrogen and ethane isotherms, clearly indicating that a difference of about 1.2 Å in radius has little impact on this feature regardless of the adsorbate been studied.

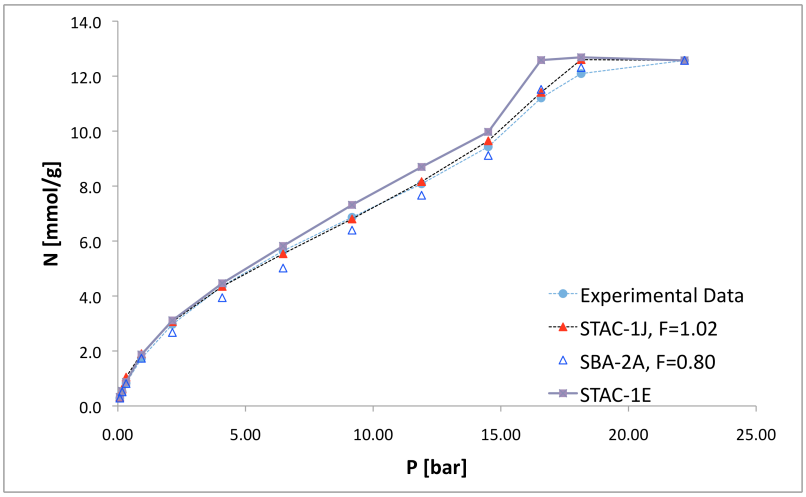

Figure 3-23: Comparison between experimental and predicted CO_2 isotherms at 263 K (lines are a guide to the eye).

A closer look at the relative errors obtained by predictions with both models (Figure 3-24) provides further prove that the STAC-1^J model allows for a very good representation of the experimental isotherm. It is worth noting that although the SBA-2^A pore model slightly underpredicts carbon dioxide uptake at low pressures the STAC-1^J model overpredicts it. This can be related again to the pore roughness, where the less rough model (SBA-2^A) underpredictions extend to medium ranged pressures due to pore-size effects: the larger the pore the weaker solid-fluid interactions that can be felt in the pore.

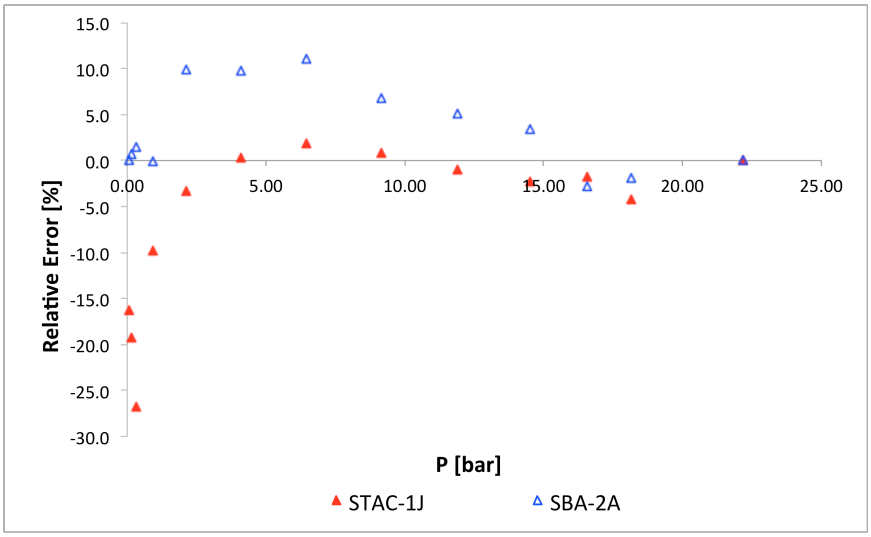

Figure 3-24: Relative errors obtained by comparison to experimental isotherms when predicting CO_2 adsorption with the STAC-1^J and the SBA-2^A models.

As it happens, the predicting capabilities of the individual model pores for carbon dioxide adsorption is remarkably good; this of course, along with the close match found for the other adsorbates investigated, supports the reported experimental PSD for SBA-2 (Kim and Stucky 2000) that typically exhibits a sharp peak: a predominant pore size. Nonetheless, it is worthwhile evaluating if there is anything to be gained from using any of the PSD already calculated.

To that end we turn to Figure 3-25. The predicted isotherms using a PSD, though not as good as the previously reported for STAC-1^J, are still quite reasonable. It is also apparent that the PSD obtained with the nitrogen isotherm has an edge over the one calculated with the ethane isotherm, especially when mimicking the inflexion point around 15 bar (i.e. the ethane-PSD looks rather flat), and this is related to the fact that Coulombic interactions play an important role on CO_2 capture due to its quadrupole, just as they do for nitrogen.

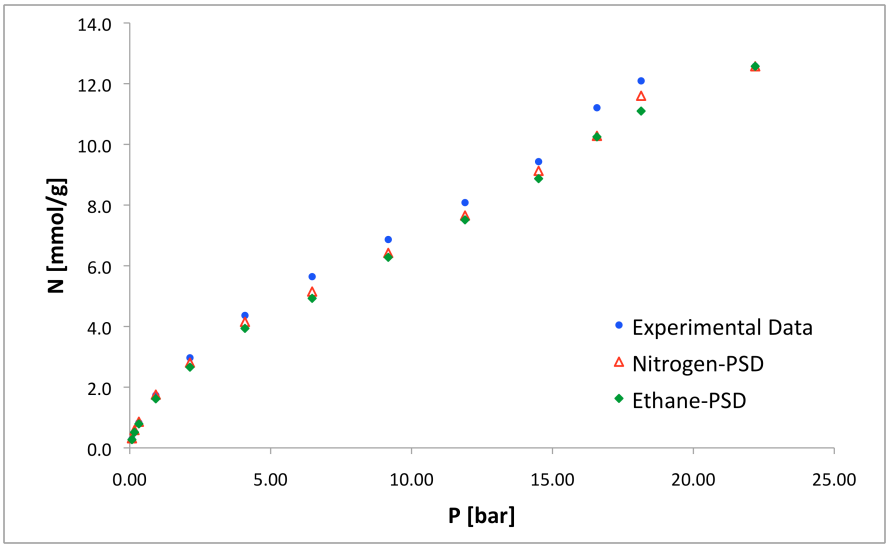

Figure 3-25: Comparison of the prediction of CO_2 adsorption by two PSD: one obtained by fitting nitrogen adsorption at 77 K, and one achieved by fitting ethane adsorption at 273 K.

From Figure 3-26 it can be seen that the relative errors obtained with the nitrogen-PSD are lower than those from the ethane-PSD throughout the pressure range under study. Furthermore, this difference is enhanced in the key areas of the CO_2 isotherm: Henry region, and phase transition; where the nitrogen-PSD predictions are more reliable.

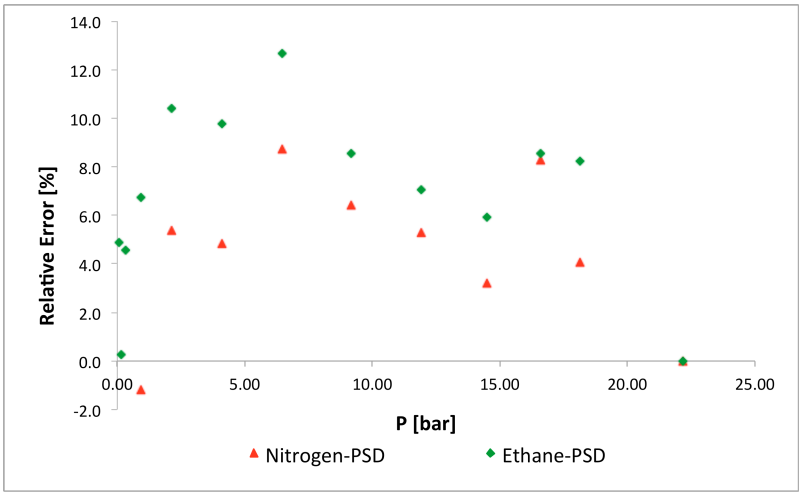

Figure 3-26: Evaluation of the residuals when predicting CO_2 adsorption at 263 K by the proposed PSD.

3.8. Studying the LJ potential parameters for the adsorbents

The LJ parameters for the pore models were taken from the optimization of GCMC predictions for methane on smooth MCM-41 models (Düren 2002), however it is uncertain whether these parameters can be directly transferred to other mesoporous silicas. The LJ diameter (σ) for the oxygen atoms is reported for different molecules (Jorgensen et al. 1996) and agrees well with the values used for the pore models, but the potential depth (ε/k_b) has been reported to vary over a wide range of values (from 152 K to 1313 K) to reproduce experimental data (Düren 2002).

For this study we are using the STAC-1 model pore F, simply because it has the lower number of wall atoms allowing for efficient computational time. It is assumed then that the discussion that follows can be extrapolated to other pore models, with better of worse predictions achieved according to other characteristics of the pores like their size and rugosity.

A reduction/increase of ε/kb for the wall-oxygens will directly affect the solid fluid interactions. Considering the results presented throughout this chapter it makes sense to investigate if its value should be lower for the materials under study since this would, in principle, reduce the overpredictions at low pressures and should not have a great impact on the predicted pore capacity. Figure 3-27 shows the methane isotherms predicted using the model STAC-1^F for potential depths of the wall oxygens varying between 135 K up and 200 K. Note that for the higher values not only methane loading is greater at low pressures than the one predicted with 185 K, but also that within reasonably medium pressures the curvature of the isotherm is greater; while for the lowest value the predicted isotherm is a perfect match of the experimental data.

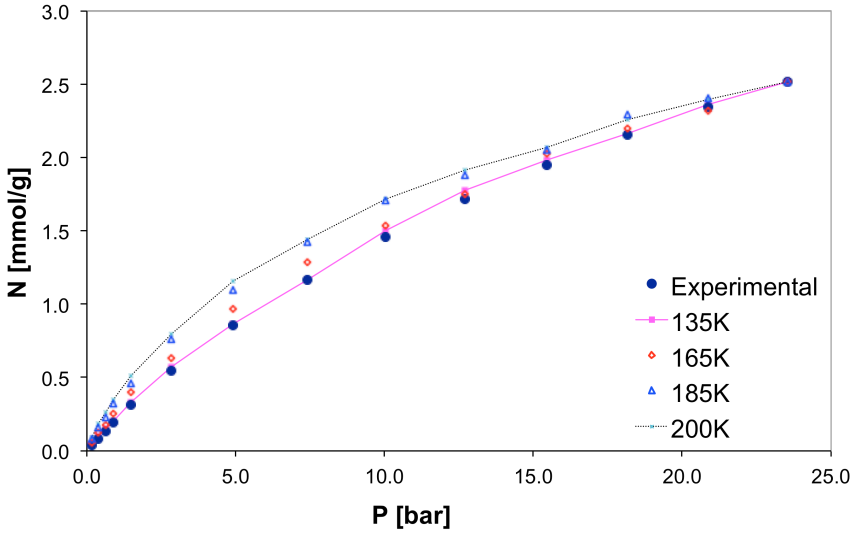

Figure 3-27: Effect of varying ε (reported in $ε/k_b$) on adsorption predictions for methane at T=273 K using the pore-model STAC-1^F (lines are a guide to the eye).

Thus, we examine the effect of this parameter on the prediction of ethane isotherms for values lower than 185 K. Figure 3-28 shows that although the lowest potential depth is suitable for methane predictions it does not really captures the complexity of the ethane isotherm where the best fit is achieved for $ε/k_b$ = 165 K. It seems that this potential depth manages to improve ethane adsorption predictions by compensating for the excess rugosity on the pore surface.

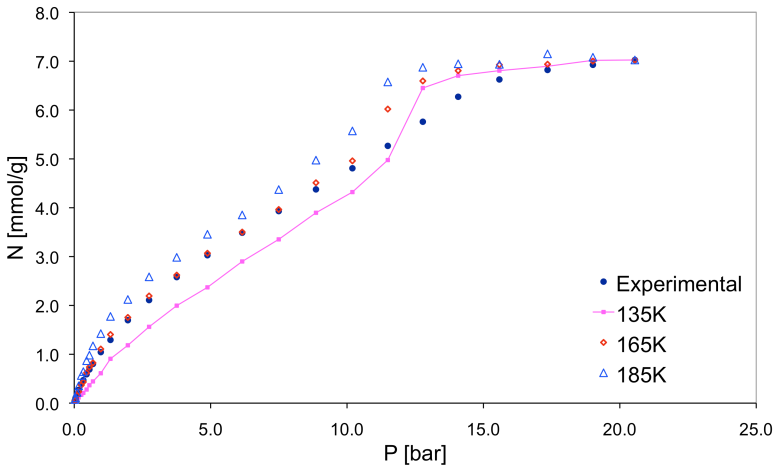

Figure 3-28: Effect of varying ε on adsorption predictions for ethane at T=273 K using the pore-model STAC-1^F (lines are a guide to the eye).

From Figure 3-28 it is apparent that the effect of the LJ parameter ε carries up to medium pressures (~10 bar) so that the slope linking adsorption in the Henry region (low pressures) with the phase transition (condensation) flattens as the potential depth is decreased. This leads towards higher pressures for pore filling and steeper inflexion points (the simulating results eventually crossing the experimental data). Physically what happens is that the phase envelope of the confined fluid is modified so that its critical properties increase towards what they would be for the unconfined fluid – effectively, in the limit when the LJ potential depth approaches zero the fluid-wall interactions disappear and the fluid properties can be predicted through any standard equation of state.

Figure 3-29 shows that as ε increases, the scaling factor does not change for ethane (as expected) but it decreases for methane. The confinement conditions for methane are such that the pressures studied are far from the saturated pore pressure and thus the pores are never filled with methane. This means that solid-fluid interactions prevail over fluid-fluid interactions throughout the pressure range studied for the methane isotherms, whereas that is not the case for ethane.

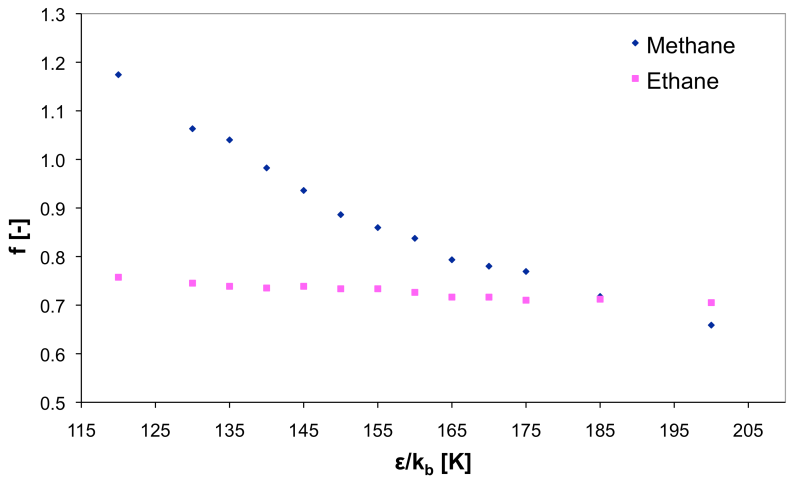

Figure 3-29: Trends for the scaling factor as the LJ potential depth varies.

Figure 3-30 studies the squared errors for the ethane isotherm predictions at 273 K, where an optimum appears around ε/k_b = 165 K. The squared errors are also reported for the methane isotherm at 273 K, but from the discussion above it is clear

that this isotherm does not provide sufficient information on the solid-fluid and fluid-fluid interactions to be used as guidance for this study.

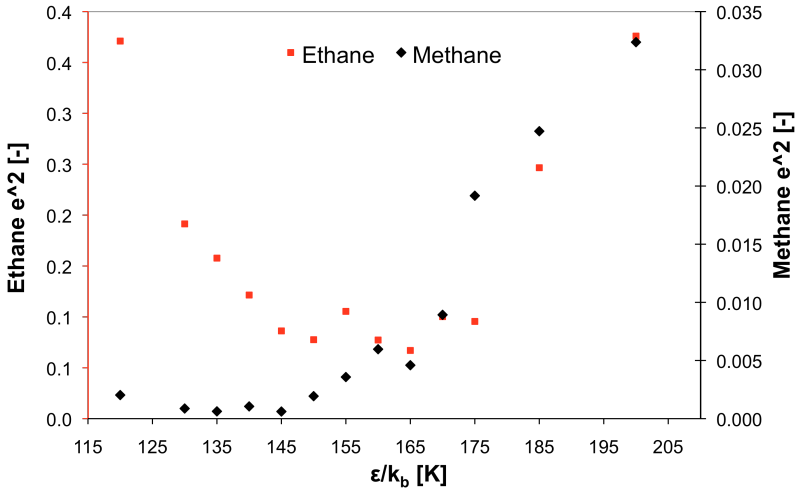

Figure 3-30: Sum of squared errors for methane and ethane isotherms at T=273 K when varying ε. Calculations using the model STAC-1^F.

Although the reduced solid-fluid interaction has improved adsorption predictions of non-charged adsorbates, Figure 3-31 shows it has a negative effect when the adsorbates are polar molecules. The effect of the new LJ parameter for the wall atoms is mostly noticed at pressures below 0.2 bar (low pressures as expected), and rather than improving nitrogen adsorption predictions it hinders them. Overall, it seems to make the inflexion in the nitrogen isotherm less pronounced, and thus the shape of the isotherm is less accurate.

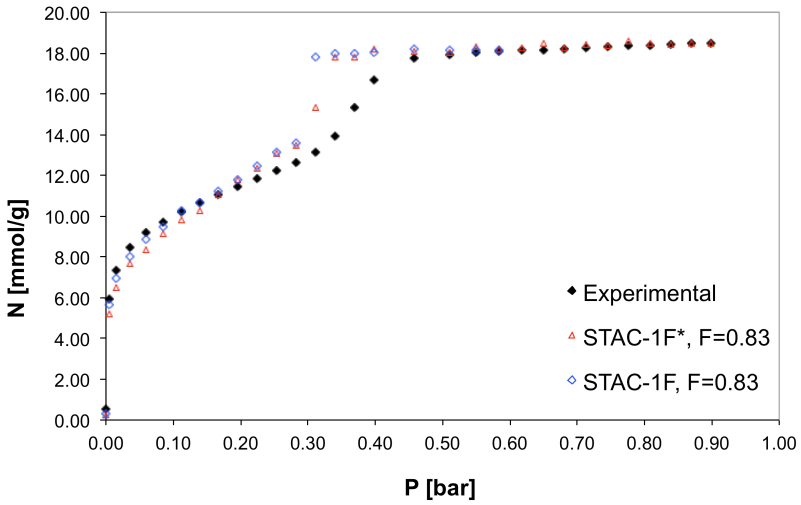

Figure 3-31: Predictions for N_2 adsorption with the STAC-1^F model pore using ε/k_b as 165 K (*) and as 185 K for the wall atoms.

As for nitrogen, when predicting the CO_2 isotherm at 263 K - Figure 3-32, it is observed that carbon dioxide loading is now consistently under predicted throughout the entire range of pressures prior to phase transition. The inflexion of the isotherm is now more pronounced than it should be and loadings at low pressures indicate an under-estimation of the Henry region for the solid-fluid system. This means that the new LJ parameter for the wall is not adequate for either of the polar adsorbates being studied in this thesis.

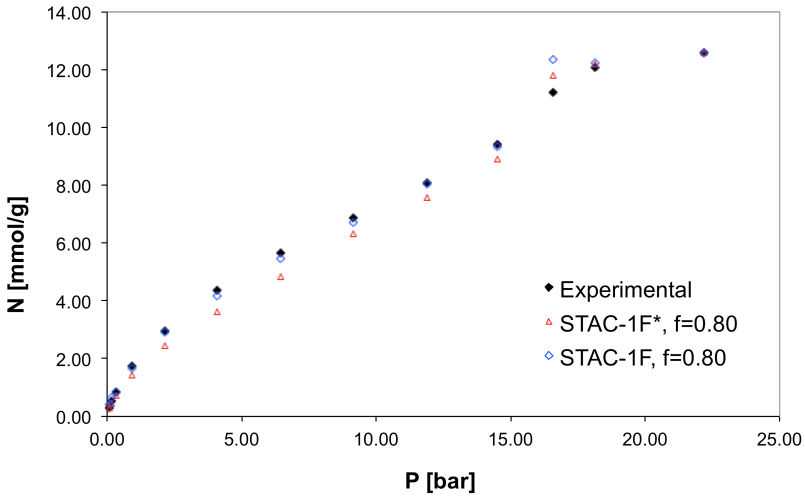

Figure 3-32: Predictions for CO_2 adsorption with the STAC-1^F model pore using ε/k_b as 165 K (*) and as 185 K for the wall atoms.

It could be argued that to compensate for the behaviour shown in the previous plots smaller model pores should be taken into account, but this would be unrealistic, as it would lead to over-estimation of the adsorption of non-polar adsorbates. Moreover, the phase transition pressure for carbon dioxide adsorption is well predicted (Figure 3-32), which means that the pore sizes are close to those of the real sample.

It is concluded then that the initial set of parameters for the wall force field which were originally derived for MCM-41 is transferable to the models of the mesoporous silicas STAC-1 and SBA-2, and the over-predictions of non-polar adsorbates at low pressures (in particular for methane) is a direct result of the roughness of the model pores. This last point agrees well with previously reported comments on MCM-41 pore models produced by the kMC technique [(Schumacher 2005) and (Herdes et al. 2011)], where it was found that they also exhibit excessive solid-fluid interactions at low pressures.

3.9. Concluding remarks

By means of grand-canonical Monte Carlo (GCMC) simulations the adsorption of both polar (nitrogen and carbon dioxide) and non-polar (methane and ethane) fluids in the pore models was investigated and compared to experimental results taken from the literature (Perez-Mendoza et al. 2004a, Perez-Mendoza et al. 2004b). The absolute adsorption calculated by the simulations was transformed into excess adsorption (for its direct comparison to experiments), to this end the porous volume of the models was calculated by simulating the adsorption of helium, which is an adsorbate that weekly interacts with the solid.

The simulated systems exhibit strong solid-fluid interactions as a direct consequence of the rough nature of the pore walls, which correlates well to experimental observations. In general, the agreement between experiments and simulations with either STAC-1 or SBA-2 model pores was very good, since their

connecting windows have little contribution to the final amount adsorbed. Model pores that closely match the pore size of the experimental sample (as determined by comparing the capillary condensation pressure and pore capacity) were found to overpredict methane uptake specially at low pressures, which was also observed (though to a much lesser degree) for ethane. It is thought that this overprediction is the consequence of excessive roughness on the pore wall. Ethane molecules are less sensitive to the surface roughness because they are longer than methane molecules, thus the latter find it easier to move into nooks and crannies.

Nitrogen adsorption was studied with two potential models: one without charges (N2-A), and another with charges (N2-B) explicitly accounting for the molecule's quadrupole. Although in the Henry region both models showed a similar behaviour, the more complex model (N2-B) proved more accurate for adsorption predictions elsewhere, specially regarding both capillary condensation and the shape of the isotherm that leads to the phase transition.

To improve the simulation results, a quasi pore-size distribution (PSD) was derived using the non-charged N_2 model. The PSD thus obtained is bimodal, contrary with what was expected from experimental characterisation presented in the literature (Huo et al. 1995). While this approach lead to better results (than those obtained by individual pores with the N2-A potential) its overall predictions are comparable to those observed when using individual pore models with the more thorough nitrogen potential (N2-B). Furthermore, the quasi-PSD when applied to other adsorbates exhibits little improvement respect to the predictions achieved with the individual adsorbent pore models, as was particularly shown for carbon dioxide adsorption (section 3.7).

Overall, using a PSD is not necessary when predicting adsorption in either SBA-2 or STAC-1 materials as the individual pore models show good predicting capabilities. In particular, for the sample used to measure adsorption isotherms (Perez-Mendoza et al. 2004a, Perez-Mendoza et al. 2004b) the models STAC-1^J and SBA-2^A gave the best results. Nonetheless, the pore roughness, the pore size, and

choosing the correct adsorbate potential are important parameters to achieve a good representation of the adsorption system. Fine-tuning the pore models for low-pressure adsorption is difficult because it implies adjusting the pore roughness. Since it is not clear how this could be achieved in the simulated synthesis of the materials, the Lennard-Jones potential depth parameter of the wall atoms provide a viable alternative. It was shown that by decreasing this parameter in 10 %, both ethane and methane adsorption predictions were visibly improved.

Given the success of the model pores in predicting adsorption, specially for carbon dioxide, in the next chapter we take them a step forward and focus on improving CO_2 uptake at low pressures (which is desired for certain carbon capture applications such as from flue gases). To that end the model pore surface is modified by grafting using surface groups with different functional groups and chain rigidity.

4. Engineering Materials for CO_2 Capture

In the previous chapter was shown that the pore models can be used to predict adsorption for both polar and non-polar adsorbates. In particular, the good agreement between the experimental isotherms and simulations without using a fitting procedure is a clear indication of the potential of these pore models to be used in designing materials towards specific applications such as CO_2 capture, for which it is desirable to maximise adsorption at low pressures (i.e. pressures near atmospheric conditions). Because CO_2 has a significant quadrupole its Coulombic interactions with the material are very important, therefore the pore surface should be designed to make it more attractive to polar substances. This can be achieved by inserting electronegative functional groups (amines, acids, among others), which introduce a significant contribution to the solid-fluid polar interactions.

Experimentally PMS functionalisation can be achieved by using a silica source (i.e. TEOS) where the desired surface group had replaced one of the ethyl groups. This substituted silica can be introduced either as silica source during the synthesis (in-situ) or by post-synthesis modification, which involves refluxing the as-synthesised material with a solution of the substituted silica species. In the first case the degree to which the surface is functionalised is related to the ratio of substituted/un-substituted silica source used. In the post-synthesis process the degree of functionalisation depends on the concentration of the substituted silica in the solution.

This chapter is a design exercise where, by evaluating prospective surface modifications, suitable surface-group characteristics for CO_2 capture are identified which can be used to guide future experimental research. Since no comparison to experiments will be made in this work, we have selected a model pore with a low number of atoms to favour the speed of the computations. Specifically, the simulations have been carried out in the unmodified and functionalised STAC-1^E

model pores, which by means of the random walk (section 2.4.4) has been found to have 304 silanol groups on the pore surface (using a probe molecule of 3.3 Å). The force field and geometry of the different surface groups presented here can be found in the Appendix, Table A-1 to Table A-4.

4.1. Grafting of model pores

Using an in-house grand-canonical Monte Carlo (GCMC) code grafting of the surface in the model pores is achieved by replacing the silanol groups on the pore surface by the desired surface group (see Figure 4-1). Any number of surface groups can be introduced in the model up to the total number of surface silanol groups present, determined by the random walk method described in section 2.4.5. This substitution method cannot compare to post-synthesis grafting where substituted silica monomers attach to the surface by linking its three silicon-oxygens to suitable silanol sites on the wall, but it is fairly representative of in-situ functionalisation. Furthermore, for SBA-2 and STAC-1 this is the appropriate grafting method since the small size of the connecting windows would make it almost impossible for the substituted silica monomers to reach into the pore cavities and percolate through the material.

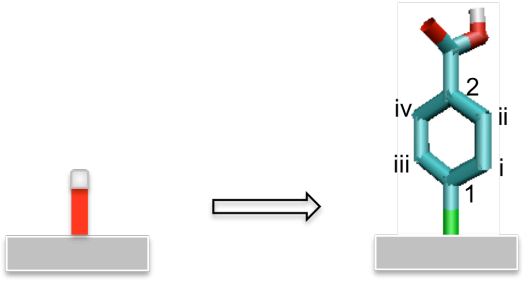

Figure 4-1: Example of grafting on the pore model: a silanol group (left) is replaced by a benzoic acid (right).

After all the surface groups had been placed on the pore surface their location can be changed by swapping with a - non-substituted - silanol surface group, and then the energy of the obtained configuration is minimized by allowing the surface groups to

move. After many swapping trials (i.e. fifty different configurations) the best configuration is chosen based on the energy stability criterion (the most stable configuration being that with the lowest energy).

The degree of functionalisation in the model pores is defined as the percentage of the number of substitutions over the total number of original silanol groups on the pore surface. During the adsorption simulations the surface groups are allowed to move. However, adsorption equilibrium in a substituted system takes time and to avoid large simulation times the probability of selecting a surface group is set to 5 %, thus each conventional GCMC trial has a 95 % probability of modifying the adsorbate configuration in the model pore.

4.2. Enhancing surface-CO_2 interactions

Carbon dioxide molecules have a strong quadrupole and thus are polar in nature. Therefore, increasing the polarity of the pore surface enhances its interactions with CO_2 molecules. The surface groups selected for this study have distinctive functional groups, whose electronegativity contributes to the desired increase in the surface polarity. Some of these surface groups are known to have an affinity for CO_2 since they are currently used in CO_2 absorption processes (amines, tetrahydrofuran, polyethylene glycol) while the others (ketone, ester, acid) are included to test if such affinity is present.

Adsorption at 263 K and 0.134 bar is presented for the selected model pores. The simulation conditions were chosen because solid-fluid interactions are predominant at low pressures, and because carbon dioxide normally found in flue gases is at partial pressures lower than 0.15 bar (Desideri and Paolucci 1999) as is further explained in Chapter 5. The lower than ambient temperature was used in order to increase the number of CO_2 molecules adsorbed in the unit cells (lower temperatures lead to higher adsorbate loading), and thus improve the quality of the statistical

results. Nonetheless, the effect of the contribution of the surface groups to the solid-fluid interactions is bound to be consistent for any temperature chosen.

4.2.1. Surface groups and CO_2 adsorption

Amines are used in absorption processes, for example, for the CO_2 removal from flue gases in power plants [(Desideri and Paolucci 1999), (Fiaschi and Lombardi 2002) and (Ebenezer 2005)]. Since amines work well as absorbents, attempts have been made in using them to enhance the CO_2 uptake by adsorbents. Chang et al. (Chang et al. 2003) reported that carbon dioxide adsorption on SBA-15 grafted with (aminopropyl)triethoxysilane (ATPS) occurred in the form of carbonates and bicarbonates (through chemical reaction) that could later be desorbed as pure CO_2. Knöfel *et al.* (Knofel et al. 2009) report chemical reaction between carbon dioxide and the amine sites when adsorbing the latter on aminopropylsilane (APS) grafted silica supports; and there are other works [(Bacsik et al. 2010a) and (Serna-Guerrero, Belmabkhout and Sayari 2010)] supporting that using amines for adsorption leads to chemisorption. These chemisorption processes cannot be simulated using classical simulation as GCMC simulations only reproduce physisorption processes.

However, Schumacher *et al.* in 2006 (Schumacher et al. 2006a) compared simulations on amino-propyl functionalised MCM-41 (assuming physisorption) to experimental isotherms obtaining remarkable agreements. Furthermore, it has been reported that in amino functionalised silicas carbon dioxide sorbs by a combination of physisorption and chemisorption, the latter being predominant at low pressures (Bacsik et al. 2010b). Further evidence sustaining the physisorption mechanism of carbon dioxide in amino-modified silicas is given by Zelenak *et al.* (Zelenak et al. 2008). They studied adsorption/desorption of CO_2 in SBA-12 mesoporous silicas functionalised with different amino surface groups and showed that the materials could be regenerated without heating by purge with an inert gas.

Bearing that in mind, Figure 4-2 presents the amount adsorbed of carbon dioxide predicted at 263 K and 0.134 bar for the unmodified and functionalised model pores,

where three amino surface groups are included: methyl amine, propyl amine and diamino-phenyl amine. It can be seen that placing amino groups on the pore surface increases the CO_2 uptake in the model pores, as expected.

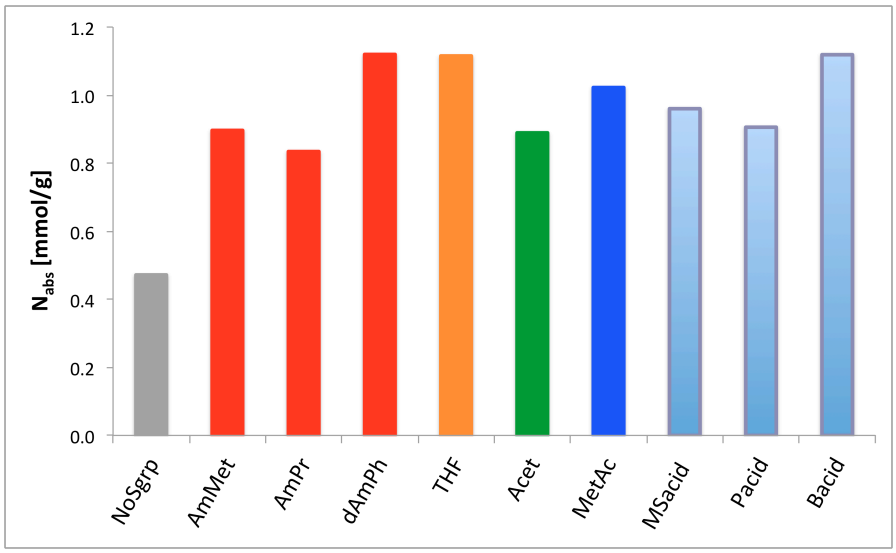

Figure 4-2: Carbon dioxide absolute adsorption at 263 K and 0.134 bar in an unmodified STAC-1^E model pore (NoSgrp), as well as functionalised with: amino-methyl groups (AmMet, 8 %), amino-propyl groups (AmPr, 8 %), diamino-phenyl groups (dAmPh, 8 %), THF (9.8 %), acetone (8 %), methyl acetate (8 %), methyl-sulfonic acid (8 %), propanoic acid (8 %), and benzoic acid (8 %).

The idea behind using amino-methyl and amino-propyl groups is to project the amino heads farther to the centre of the pore and in doing so increase their interaction with the CO_2 molecules being adsorbed. Since the propyl chain is larger it was expected that this would be more effective by increasing the CO_2 contact with the amino heads and so would lead to higher carbon dioxide uptake. This however is not seen in Figure 4-2. Rather, this figure indicates that adsorption with either alkyl chain is rather similar and although this was not the obvious result, it was partially expected since the same behaviour had been previously reported for amino-methyl and amino-propyl substituted MCM-41 materials [(Schumacher et al. 2006a) and (Williams et al. 2010a)].

For MCM-41 it was shown that amino groups with large alkyl chains tend to bend so that the functional group points to the wall rather than to the centre of the

pore. As it is shown in the snapshot presented in Figure 4-3 this is also the case for the STAC-1 pore model. This means that the amino group becomes partially shielded from the adsorbate molecules, and thus the increase in uptake is not as expected, and not least due to the higher molecular weight of the functionalised model (due the longer alkyl chain). The shorter alkyl chain of the amino-methyl group has the advantage of avoiding the bending problem seen for amino-propyl molecules (since it is too short), but at the same time it keeps the amino heads close to the pore wall and are therefore unable to reach adsorbate molecules near the centre of the pore.

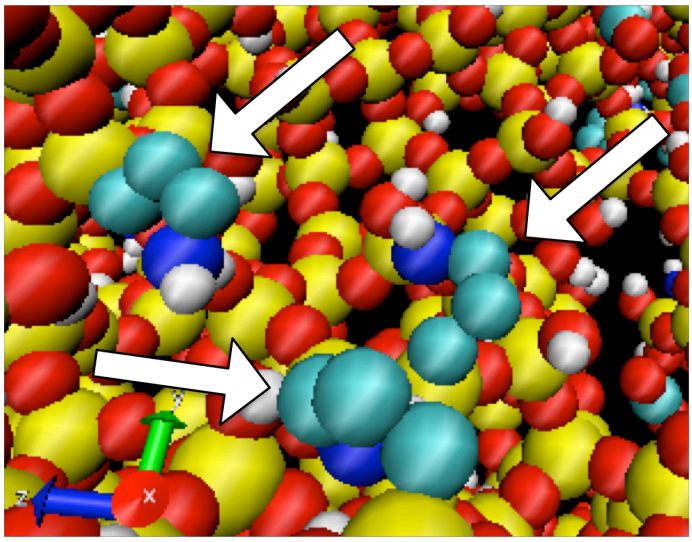

Figure 4-3: Snapshot from CO_2 adsorption in the amino-propyl modified STAC-1^E model pore. The white arrows indicate the surface groups bending so that the amino groups face the pore wall. [Si atoms in yellow, oxygen atoms in red, hydrogen atoms in white, nitrogen atoms in blue and CH_2 links (UA force field) in green].

One way to understand the fluid-solid interactions better is to look at the energy histograms of the GCMC simulations [(Düren and Snurr 2007) and (Düren, Bae and Snurr 2009)]. Figure 4-4(a) presents these energy distributions for the three surface groups with amino functional heads. Each of the functionalised model pores exhibits stronger interactions with the fluid than the unmodified pore – as expected. This is clearly indicated by the disappearance of the right-hand shoulder present in the distribution of the unmodified pore, which results from weak CO_2-wall interactions from molecules wandering near the centre of the pores where the least favourable

adsorption energies can be found. Also, the mean energy of interaction for all functionalised materials is similar.

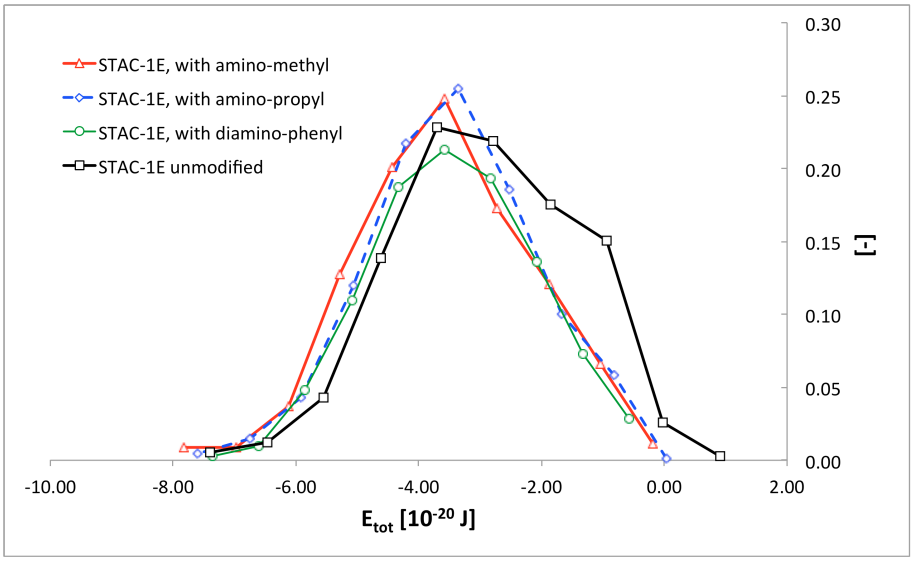

(a)

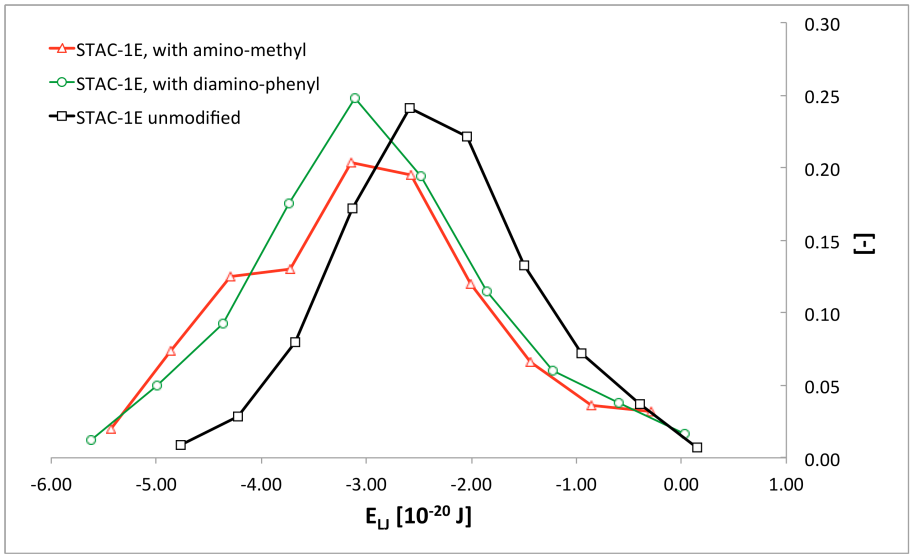

(b)

Figure 4-4: (a) Energy histogram for the unmodified STAC-1^E model pore and those functionalised with: amino-methyl (8 %), amino-propyl (8 %) and diamino-phenyl (8 %). (b) Energy histogram for LJ fluid-solid interactions for the unmodified model pore and those functionalised with amino-methyl (8 %) and diamino-phenyl (8 %).

It can also be seen in the figure above (Figure 4-4(a)) that the amino-methyl substituted model pore has a larger tail (towards larger negative energies) than the amino-propyl and diamino-phenyl functionalised pores. The latter two surface groups are much larger volume wise than the former. This means that it is more

likely for them to block the nooks and crannies that would normally be accessible to CO_2, which are highly attractive as was shown on Chapter 3, thus restricting access to sites with large interaction energies.

The latter point is corroborated in Figure 4-4(b), which shows the energy histogram for the dispersive solid-fluid interactions (i.e. without the contribution from the electrostatic interactions). It can be seen that the LJ histogram for the amino-methyl substituted model has a shoulder towards negative, i.e. favourable, energies that is absent from the diamino-phenyl modified model. In general, the LJ interactions are stronger than they are for the unmodified case since both the functional group and the organic members of the surface groups enhance LJ interactions and CO_2 molecules are less likely to move towards the centre of the pore, which is also a factor that helps improve the amount of CO_2 adsorbed.

The acid functional group is the most electronegative among the ones considered in Figure 4-2, and as happened with the amino groups, adsorption with propanoic acid suffered from the 'back bending' effect described above. Nonetheless, the amount adsorbed by this model pore is larger than that reported with the amino-propyl functionalised model (Figure 4-2) as expected due to the higher electronegativity of the acid group. This can be seen in Figure 4-5, where it is clear that the model pore functionalised with propanoic acid provides more favourable sites (negative energies) for CO_2 to adsorb.

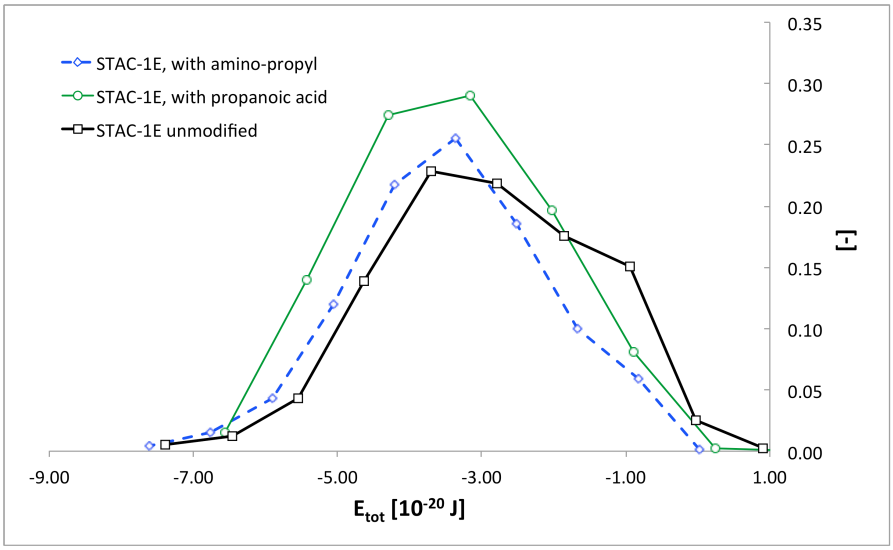

Figure 4-5: Energy histogram for the unmodified STAC-1^E model pore and for the amino-propyl (8 %) and propanoic acid (8 %) functionalised pores.

Recently (Dacquin et al. 2010) propyl-sulfonic molecules were placed experimentally as surface groups on MCM-41 surfaces. In our work, to avoid the 'back bending' effect observed with the long alkyl chains methyl-sulfonic groups were used instead. The model with this surface group adsorbs 0.960 mmol/g of carbon dioxide (Figure 4-2), which is comparable (and slightly larger) to the amount adsorbed by the amino-methyl functionalised model (0.890 mmol/g), both outperforming the use of amino-propyl and propanoic acid surface groups.

Figure 4-2 shows that methyl-acetate functionalisation is more effective (1.022 mmol/g) than any of the other surface groups used here, save those with phenyl rings or heterocycles. This is interesting since the acid, ketone and amino groups are more electronegative than the ester group in this molecule. It appears then that the key factor is the projection of the methyl-acetate molecule towards the pore centre and that despite the terminal CH_3 in the molecule its oxygen atoms are exposed to interact with the adsorbate molecules. Figure 4-6 confirms that methyl-acetate surface groups do not bend back towards the pore wall, most likely because the functional group is not located at the end of the molecule.

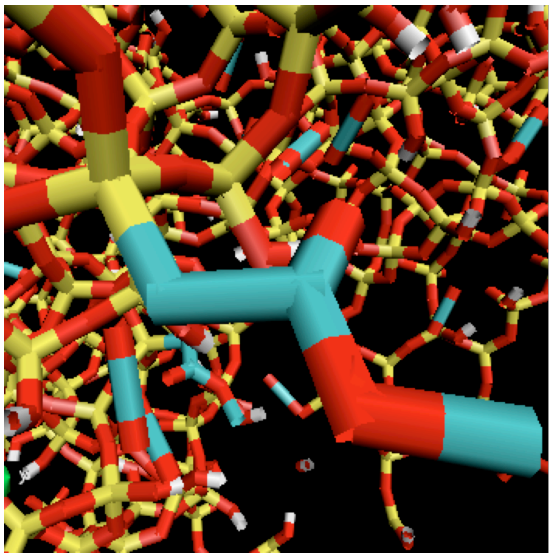

Figure 4-6: Snapshot showing a close-up of a methyl-acetate surface group projecting towards the cavity centre. Taken from the methyl-acetate functionalised (8 %) model pore.

The positive effect of projecting the surface group towards the centre of the pore is further corroborated by the model pores functionalised with rigid diamino-phenyl and benzoic acid molecules. These exhibit the highest amount adsorbed of carbon dioxide (1.120 mmol/g, and 1.118 mmol/g). Furthermore, the phenyl ring is likely to have a charge density induced by the proximity of the solid surface and the functional group, which makes the molecules more attractive to polar adsorbates. Note though that the diamino-phenyl molecules have twice the number of functional groups per molecule than the benzoic acid, which is an indication that the greater electronegativity of the acid is more effective in trapping carbon dioxide molecules.

Despite better CO_2 uptake with both the diamino-phenyl and the benzoic acid modified model pores respect to the other functionalised pores being considered, they have the drawback of blocking the pore connections even at the low degree of functionalisation of 8 %. In other words, they are too bulky and are likely to reduce adsorption by either partially or totally obstructing the connecting windows. Tetrahydrofurane (oxolane) is used as an organic physical absorbent and under ambient conditions has great affinity towards CO_2 (Sweatman 2010). This heterocycle molecule is smaller than those of diamino-phenyl and benzoic acid, and by being attached to the pore surface through one of the carbon atoms not

neighbouring the oxygen in the ring (Figure 4-7) the amount of CO_2 adsorbed is significant (1.115 mmol/g).

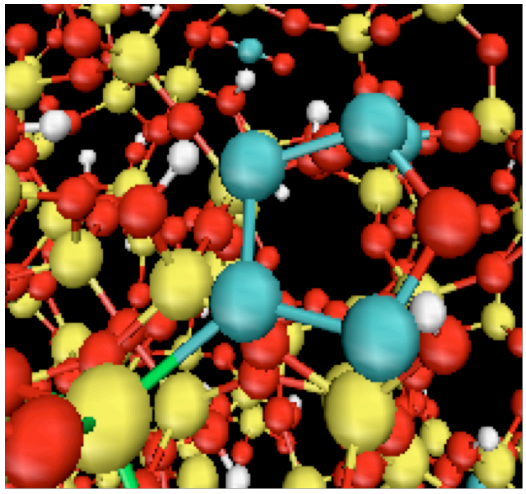

Figure 4-7: Snapshot of a THF molecule attached to a Si wall atom. The five-member ring is visible with its four carbon links and the oxygen exposed towards the pore centre.

Certainly, the degree of functionalisation in the THF modified pore is slightly larger (9.8 %) than the 8 % used for the other models, and so THF is not as effective as the diamino-phenyl and benzoic acid molecules. However, the energy histogram in Figure 4-8 shows that this functionalised model pore provides good adsorption sites for CO_2, possibly due to the – unobstructed – oxygen atom pointing towards the centre of the pore and the fixed charge distribution on the THF surface groups induced by its own oxygen and the proximity of the pore wall. Furthermore, this model pore exhibits open connecting windows, so the pores in the material remain accessible to the adsorbate molecules. Thus, this surface group seems like a good candidate for CO_2 capture applications.

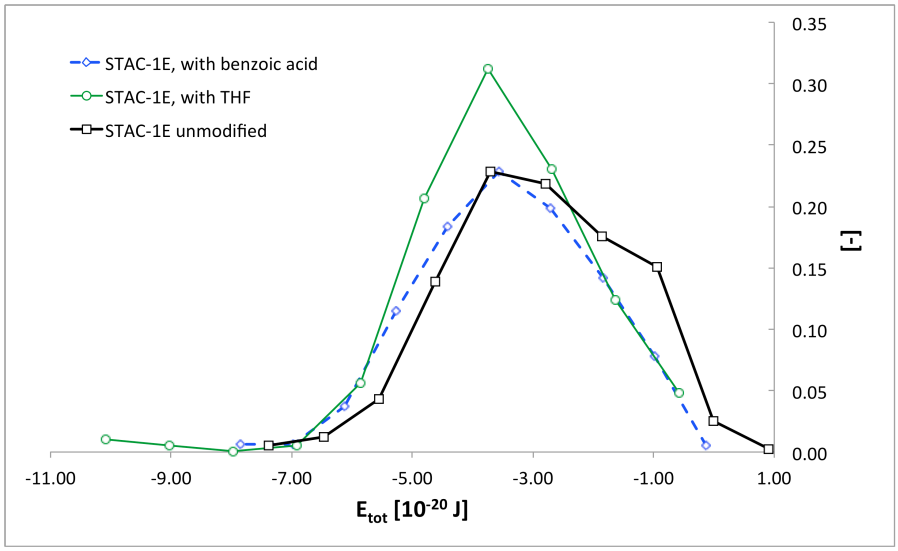

Figure 4-8: Energy distribution for the unmodified model pore STAC-1^E and for the functionalised model pores with: benzoic acid (8 %) and THF (9.8 %).

Figure 4-9 presents the snapshot of CO_2 molecules trapped in two grafted adsorbents: with THF (a), and with methyl acetate (b). It can be seen that although most of the carbon dioxide molecules are close to where the surface groups are placed, they are not preferentially located next to them. It appears then that the long ranged interaction forces of the surface groups lure the carbon dioxide molecules from the centre of the pore to the surface, and once there these molecules are attracted by the stronger adsorption sites which are provided by the nooks that arise from surface roughness.

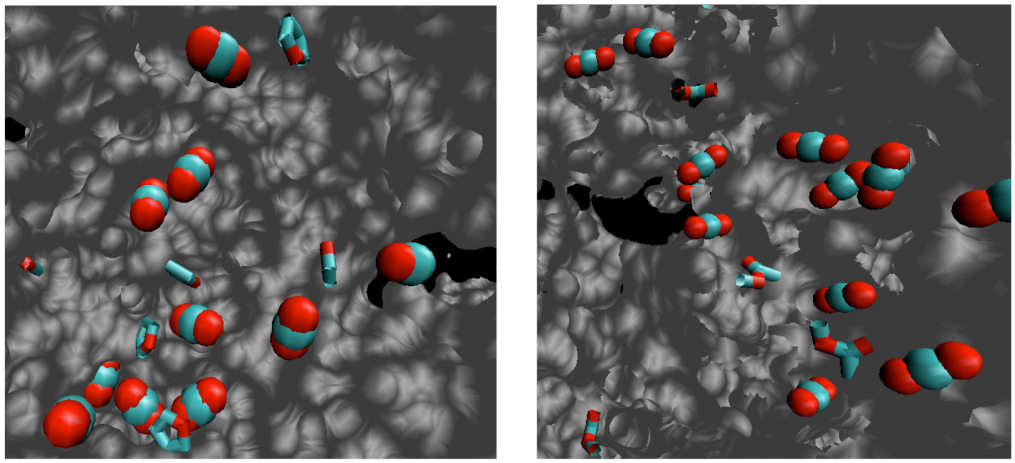

(a) (b)

Figure 4-9: Snapshot for CO_2 adsorption at 263 K and 0.134 bar: for the THF grafted pore (a) and that grafted with methyl acetate (b). CO_2 molecules are represented by spheres, surface groups by bonds, and the STAC-1 silica surface is depicted in grey.

4.2.2. Acetonitrile surface group

The nitrile group ($R-C\equiv N$) is flat and has a very short CN bond length whose strength make it unlikely to react with the carbon dioxide molecules. Thus, the idea of using a molecule like acetonitrile as a potential surface group is rather appealing since it would swiftly move through the pore network during post-synthesis functionalisation in spite of the small size of the pore connections, and it would protrude from the wall surface like sticks since it cannot bend. Figure 4-10 presents CO_2 adsorption in model pores with increasing degree of acetonitrile functionalisation, each produced by modifying the original STAC-1^E model pore. It can be seen that just a few substitution (1.6 %) are enough to nearly double the CO_2 uptake from 0.472 mmol/g to 0.865 mmol/g. As the number of substitutions increases so does the absolute amount adsorbed slowly up to 1.28mmol/g for a fully covered surface.

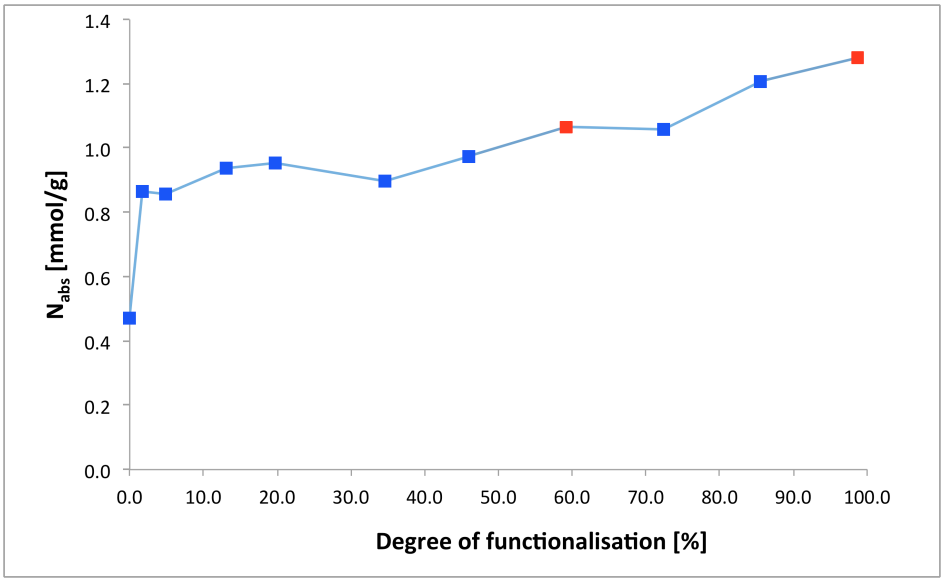

Figure 4-10: CO_2 adsorption for acetonitrile functionalised model pores with different degree of functionalisation (0 % to 99 %). Temperature 263 K and pressure 0.134 bar. Those pores without connections are depicted in red.

Although the tendency of the absolute adsorption is to increase with increased degree of functionalisation, from Figure 4-10 it is apparent that this may not always be the case. It is possible that this phenomenon is related to the positions of the replaced silanol groups, and this may indicate that for each degree of functionalisation there might be an optimum configuration that would maximise the CO_2 adsorption, although it is unrealistic to think of it as being experimentally feasible.

On a side note though, it might not always be desirable to modify STAC-1 or SBA-2 materials until its surface is fully, or nearly fully covered with surface groups since this may lead to the isolation of pores from the pore network. For example, in Figure 4-10 the model pores functionalised at ~60 % and ~99 % lost connectivity to neighbouring pores. It is apparent then that the model pores can lose connectivity due to surface groups being placed by chance in the vicinity of the connecting windows, and the probability of this to occur increases with increasing degree of functionalisation.

In Figure 4-10 the slow increase in the amount of carbon dioxide adsorbed with increasing functionalisation is because the acetonitrile molecule is small and thus it is too close to the pore wall to reach far into the pore. For model pores modified with surface groups that reach further into the centre of the pore such as methyl-sulfonic acid groups it is likely that the increase in carbon dioxide uptake will be more significant. This can be seen from Figure 4-11, where the increase in the amount of CO_2 adsorbed as function of degree of functionalisation is steeper, and the amount of fluid adsorbed is greater.

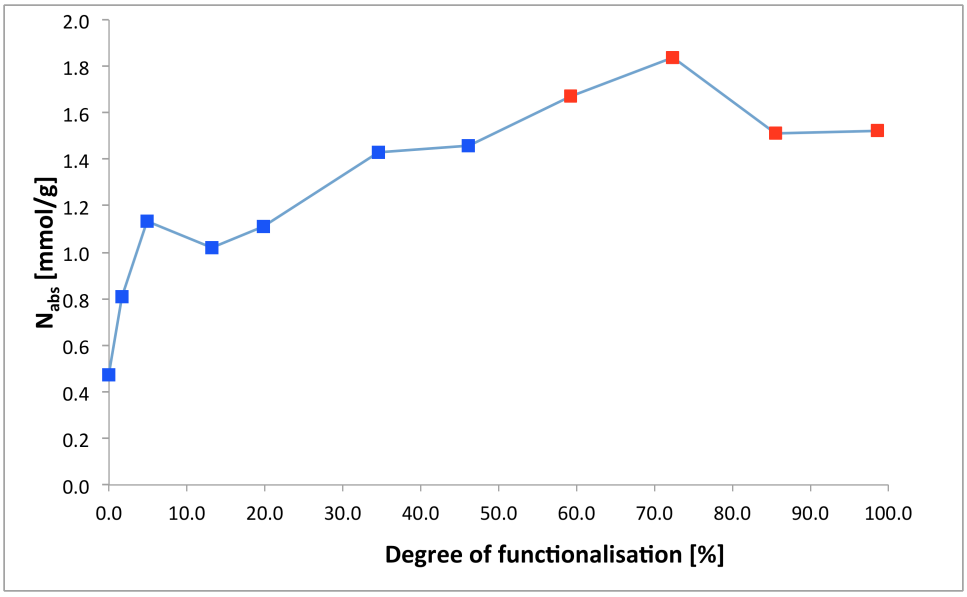

Figure 4-11: CO_2 adsorption at 263 K and 0.134 bar for model pores with different degree of methyl-sulfonic acid functionalisation. Those pores without connections are depicted in red.

However, when the model pore is functionalised with methyl-sulfonic acid molecules, after ~60 % functionalisation it was found that the connections to neighbouring pores were blocked, indicating that this issue is more important for this surface group than it was for the acetonitrile case. This was to be expected since the methyl-sulfonic acid group occupies a larger volume than the acetonitrile molecules, and as we approach full surface coverage the silanol groups near or in the connecting windows are likely to be replaced, thus leading to pore blocking.

4.2.3. Polyethylene glycol (PEG)

Polyethylene glycol is used in a physical absorption process called Selexol. These types of processes remove CO_2 based on its solubility in organic solvents rather than by chemical reactions. The polyethylene glycol surface group studied here has the formula $CH_3CH_2O(CH_2CH_2O)_2H$. It is computationally expensive to simulate due to the large number of atoms that it adds to the surface and the flexibility of the molecule chain, and therefore only a model pore with 1.6 % of functionalisation was created.

The CO_2 uptake was increased significantly 0.91 mmol/g versus the 0.47 mmol/g of the unmodified pore considering the low degree of functionalisation. The increase in the amount adsorbed is also interesting since the polyethylene glycol (PEG) chains are not pointing towards the centre of the pores. As the functional group is at the end of the molecule it bends towards the wall and as it does so the other oxygen atoms in the chain become attracted by the pore surface. The overall effect leads to PEG molecules crawling on the pore surface as shown in Figure 4-12.

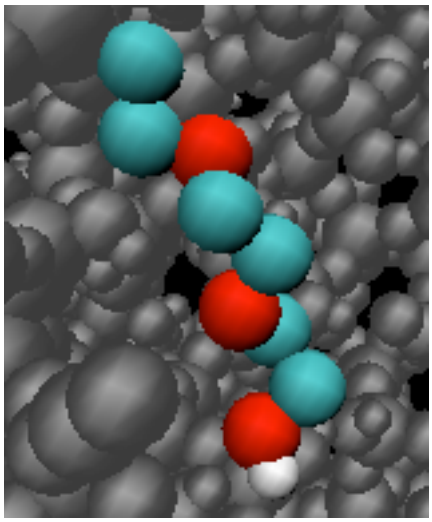

Figure 4-12: Screen shot of a PEG surface group (oxygen atoms in red, hydrogen atoms in white, and CH_2 united atoms in green). The solid wall is depicted in grey for visualisation purposes.

The increased adsorption comes as the result of the fixed charge distribution in the long chain, which adds many sites to the Coulombic interactions in the simulation cell. From the energy histogram in Figure 4-13, it can be seen that the effect of adding PEG molecules (1.6 %) is very similar to that of adding a much larger number of diamino-phenyl surface groups (8 %). Nonetheless, by protruding from the wall the diamino-phenyl molecule provides more favourable adsorption sites (the tail of the distribution edging on -7×10^{-20} J).

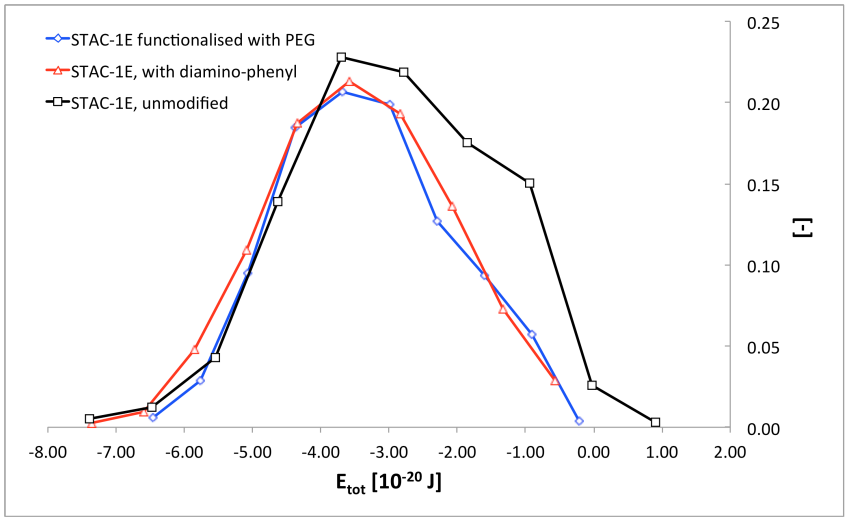

Figure 4-13: Comparison of the energy histogram for the PEG substituted model pore with that of the diamino-phenyl functionalised and unmodified model pores.

Overall, PEG also looks promising as a surface group for CO_2 capture even if the length of the PEG chains might be a drawback during the actual experimental post-synthesis process. As they percolate through the pore network and attach to the pore walls the PEG molecules could obstruct the connecting windows between the pores, making the diffusion of other PEG molecules through the material difficult. This means that it may be difficult to obtain a homogeneously modified material.

4.3. Effect of the degree of functionalisation on pore capacity

Although larger surface groups may enhance adsorption by adding many interaction sites to the pore, they may have undesired effects on the pore capacity and the pore network connectivity. For example, while the unmodified STAC-1^{E} model pore as well as the amino-methyl and amino-propyl model pores are connected to neighbouring pores, the diamino-phenyl modified pore lacks such connections. Similarly, the negative effect on the pore capacity can be seen in Figure 4-14 where an eight percent substitution of the pore surface leads to a 2-3 % decrease in the average pore radius.

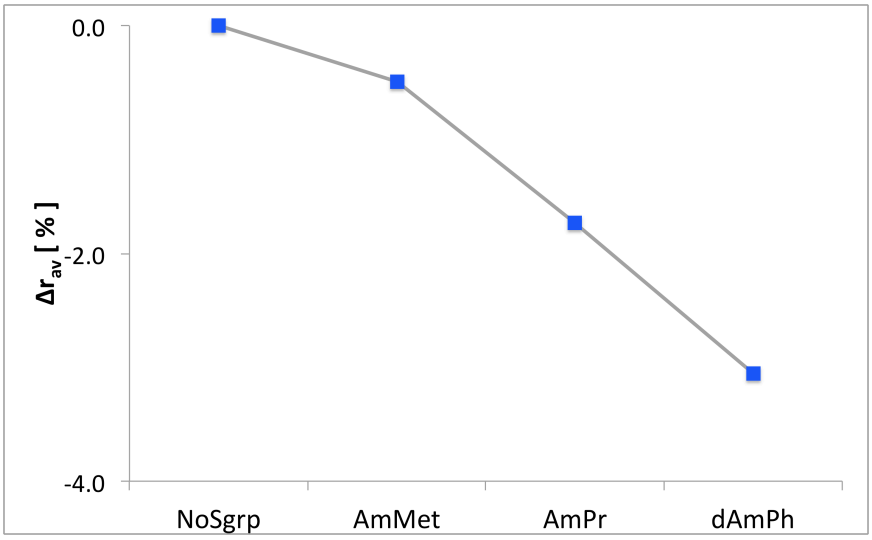

Figure 4-14: Effect of the size of the surface groups used for functionalisation on the average pore radius: STAC-1^{E} unmodified model pore (NoSgrp), amino-methyl (AmMet), amino-propyl (AmPr) and diamino-phenyl (dAmPh) modified pores.

As the degree of functionalisation is increased the reduction on the average pore size affects the pore capacity as shown by Figure 4-15. Lower degrees of functionalisation have little consequence on the total amount adsorbed at high pressures, but even for the small acetonitrile molecules as the degree of

functionalisation increases the amount of CO_2 adsorbed at pore filling is clearly diminished.

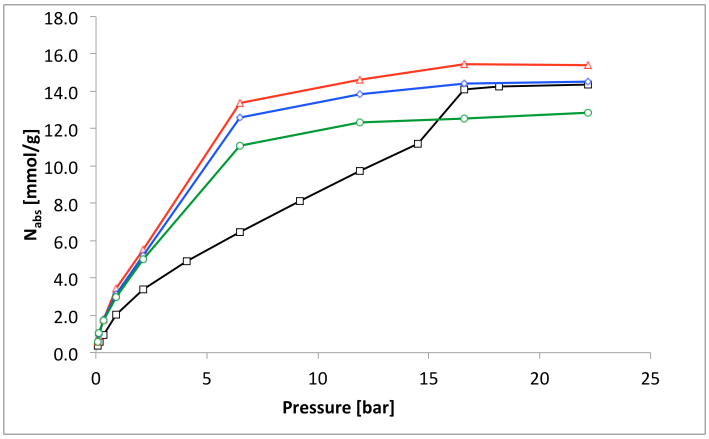

Figure 4-15: Calculated CO_2 isotherms with the STAC-1^E model pore. Isotherms are for the unmodified model pore –black, and for the functionalised pores with acetonitrile (degrees of functionalisation: 5 %–red, 13 % –blue, and 46 % –green).

The same study was repeated with pores functionalised with methyl-sulfonic acid surface groups (Figure 4-16). For the case with the lowest degree of functionalisation again the capacity of the pore is barely affected, but as further functionalisation is introduced the effect on the capacity becomes more apparent and is stronger than it was in the acetonitrile functionalised pores. In fact, by comparing the capacity at 46 % functionalisation in Figure 4-16 (~10 mmol/g) with Figure 4-15 (~12 mmol/g) it is clear that the larger the surface group the greater the reduction on the adsorption capacity in the pore models.

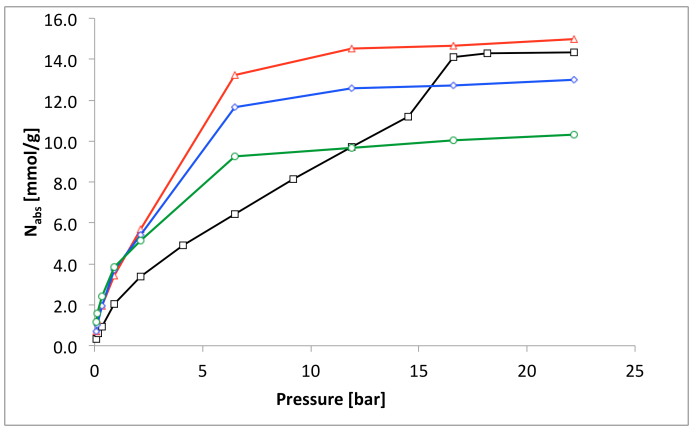

Figure 4-16: Predicted CO_2 isotherms with the STAC-1^E model pore. Isotherms are for the unmodified model pore –black, and for the functionalised pores with methyl-sulfonic acid (degree of functionalisation: 5 % –red, 13 % –blue, and 46 % –green).

4.4. Concluding remarks

The strong quadrupole of carbon dioxide molecules means that increasing the charge on the adsorbent surface is likely to favour its adsorption, especially at low pressures where the solid-fluid interactions prevail. In fact, by grafting the pore models with surface groups of different electronegativity (from ketones to acids) CO_2 uptake at 263 K and 0.134 bar was at the very least doubled when compared to that of the unmodified pore.

Benzoic acid and diamino-phenyl groups were the most effective in trapping CO_2 molecules, followed closely by THF and methyl acetate. It is reasoned that the success of these groups in capturing carbon dioxide is based on their projection into the pore cavity rather than on the strength of their electronegative functional groups. This is supported by the fact that small surface groups (such as amino methyl and methyl sulfonic acid) which remain close to the pore surface are not as effective in capturing adsorbate molecules. Furthermore, for the surface groups to be projected into the pores they need a sufficiently rigid backbone, since flexible chains (such as amino propyl, propanoic acid, and PEG) show a tendency to bend back so that their functional groups face the pore wall thus concealing them from the adsorbate.

Unfortunately, large surface groups such as benzoic acid and diamino-phenyl molecules are likely to have a negative effect in pore connectivity by blocking the connecting windows, and moreover they may also affect the pore capacity. Thus, smaller surface groups are desired when grafting these materials. From the surface groups evaluated in this chapter methyl acetate, THF and PEG showed promising results, the latter two being successful species when used independently in physical absorption processes (such as Selexol). The rigid THF molecule successfully exposes the oxygen heteroatom to the adsorbate in the pore, while the PEG molecule, despite crawling on the pore wall, provides multiple active adsorption sites. In fact, it would be valuable to find a way to project the PEG molecules further into the pore as this would most certainly increase CO_2 adsorption.

Since by pore grafting CO_2 adsorption was improved, in the next chapter potential applications for SBA-2 and STAC-1 in different carbon capture applications are studied. In particular we look at mixtures from flue and landfill gases since they have very different compositions and the desired operational conditions for carbon capture differ. Additionally we present the study of the separation of butane isomers, which can be an interesting area of application given the possibility of using these materials in molecular sieving.

5. Potential applications: adsorption of mixtures

This chapter provides further insight into the potential use of SBA-2 / STAC-1 materials for industrial separation processes. Two examples have been selected. The first application being studied is the capture of carbon dioxide. To this end two mixtures at real operating conditions have been selected, one regarding carbon capture from landfill natural gas production, and the second aiming at CO_2 capture from flue gases – the exhaust gases produced by coal power plants.

The second relates to the separation of the n-butane and iso-butane isomers, which is important for the petroleum industry to get high n-butane purity (to be sold as fuel for cigarette lighters, or as a propellant in aerosol sprays, or to be used in the production of base petrochemicals in steam cracking) and to increase the iso-butane feedstock needed for alkylation processes. SBA-2 and STAC-1 are likely to favour such separation by means of molecular sieving: the small size of the connections between pores is likely to favour n-butane diffusion over that of iso-butane.

5.1. Purification of natural gas from landfills

Mixtures of hydrocarbons with CO_2 are common in gas reservoirs from different sources. CO_2 is separated not only to meet environmental standards, but also to improve the calorific content of the hydrocarbon products (Nicholson and Gubbins 1996) and to avoid corrosion damage to the transporting pipes, as CO_2 is a highly acidic gas. For this separation process, ambient temperatures over a wide pressure range are relevant, and thus in this section adsorption isotherms at 298 K for pressures up to 22 bar are presented.

Natural gas from landfills is mostly composed of methane and carbon dioxide with some impurities (Delgado et al. 2007), as opposed to that from reservoirs where

the composition is mostly methane (>80 %) (Cavenati, Grande and Rodrigues 2006). For this reason predictions are made for an equimolar CH_4 / CO_2 mixture (molar composition, y=0.5), where the Peng-Robinson binary interaction parameter for the mixture is 0.095 (Lin 1984). Since there are no experimental data available for this case study, the same model pore as in Chapter 4 was used. All simulations herein are the results obtained for adsorption in either unmodified or functionalised STAC-1^E.

Figure 5-1 presents adsorption of the mixture in the model pore functionalised with different surface groups. The surface groups used, which have already been shown to improve CO_2 uptake in Chapter 4, clearly increase carbon capture with respect to the unmodified STAC-1 model pore. There is a slight increase in methane uptake as well, which is more significant for the acetone modified model pore. This is an indication that the electronegativity of this surface group is not as effective as that of the other surface groups.

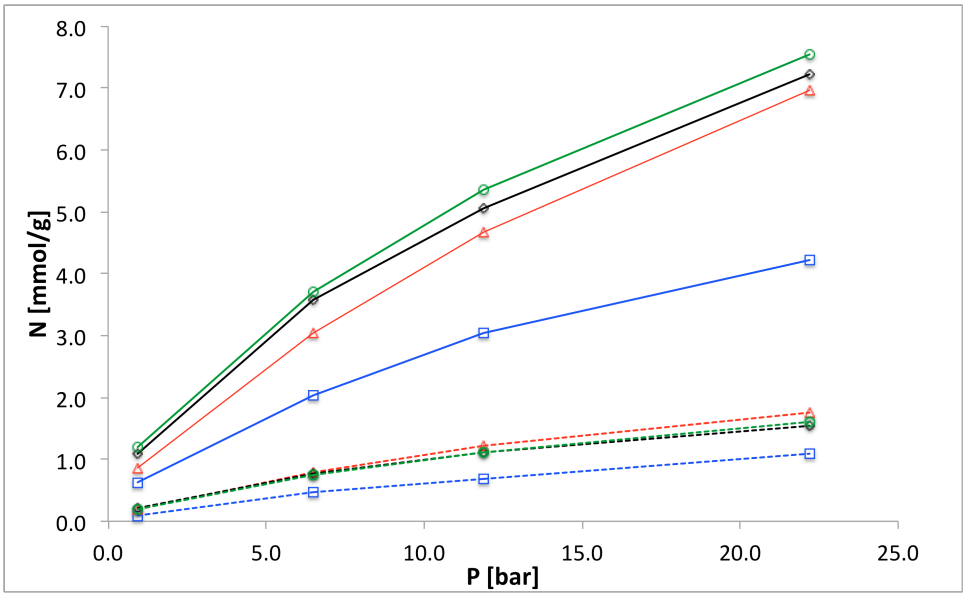

Figure 5-1: Predicted adsorption isotherms for binary CO_2 (solid lines)/ CH_4 (dotted lines) mixtures (y=0.5) for the unmodified STAC-1^E model pore (blue) and acetone (8 %, red), diamino-phenyl (8 %, black), and THF (9.8 %, green) functionalised model pores. Lines are a guide to the eye.

For pressures beyond 6 bar the reduced pore capacity favours those models with less bulky surface groups as it can be seen by the curvature of the isotherms in Figure 5-1. On that last point, it is significant that using THF as a surface group, with

slightly more substitutions than the case with diamino-phenyl groups, can provide more CO_2 adsorption throughout the entire pressure range than any of the other models used, without the risk of having CO_2 reacting with THF (since this is a physical adsorbent, as explained in Chapter 4). These reasons, plus the fact that this surface group at 9.8 % degree of functionalisation does not block the pore connectivity (as diamino-phenyl does at 8 %), make THF a potential surface group likely to be tried experimentally.

In any case, it is clear that although the unmodified model pore already favours CO_2 adsorption over CH_4, due to the silanol groups on its surface, using surface groups to promote carbon dioxide capture is desirable, as can be further evidenced from the selectivity, Equation (5-1), in Figure 5-2 (where the error bars were calculated by error propagation analysis).

$$S_{CO_2} = \left(\frac{x_{CO_2}}{y_{CO_2}}\right)\left(\frac{1 - y_{CO_2}}{1 - x_{CO_2}}\right) \quad \textbf{(5-1)}$$

For the lowest pressure the selectivity is highest in the unmodified model pore, which means that on the functionalised models although the CO_2 uptake has increased, methane uptake has increased more. This is likely related to the increased LJ interactions felt by methane molecules due to the additional atoms on the pore surface.

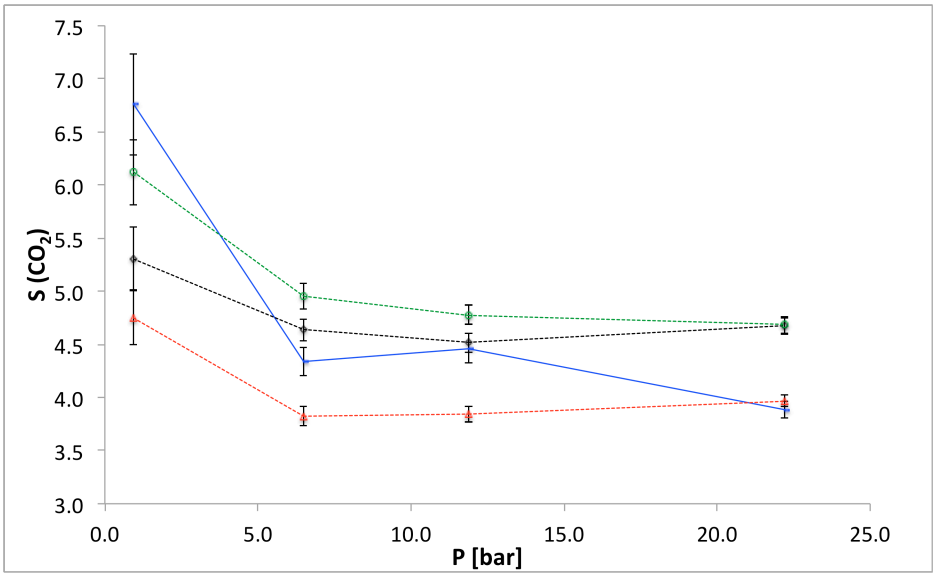

Figure 5-2: Selectivity for CO_2 / CH_4 binary mixtures: unmodified STAC-1^E (blue) and functionalised model pores, with acetone (8 %, red), with diamino-phenyl (8 %, black), and with THF (9.8 %, green). Lines are a guide to the eye.

As the pressure increases the selectivity of the unmodified model pore drops, an indication that the silanol groups, being so close to the pore wall, are not able to affect a great fraction of the pore cavity as it is evident in Figure 5-1 by the lower carbon dioxide uptake compared to the functionalised models. Also, Figure 5-2 shows the THF functionalised pore gives the best selectivity.

It is apparent that the selectivity could also be improved by further functionalisation of the pore surface. This is a reasonable statement since the more surface groups present the greater the Coulombic solid-fluid interactions. These interactions reach further into the pore than the dispersion forces, thus preferentially attracting the polar CO_2 molecules over methane.

For this particular mixture, STAC-1 shows a better behaviour for CO_2 separation than the model micropores with slit (mimicking graphitic materials) and cylindrical (mimicking zeolitic materials) geometries used by Nicholson *et al.* (Nicholson and Gubbins 1996), which exhibit a selectivity of 2-3, and that the MFI zeolite models which exhibit a selectivity of 2-3 as well, as reported by Garcia-Perez et al. (García-

Pérez et al. 2007) and Barbarao *et al.* (Babarao et al. 2006) at 300 K. The latter work also reports the selectivity of IRMOF-1 (metal organic framework, MOF) and the C_{168} schwarzite adsorbent for the same equimolar CH_4 / CO_2 mixture giving a selectivity of 2-3 and 4.5-5 respectively for pressures below 20 bar. However, whereas the maximum CO_2 absolute adsorption predicted in this work is about 8 mmol/g at 20 bar (with the THF model pore), which exceeds that of MFI (~2.2 mmol/g) and of the C_{168} schwarzite (~6 mmol/g), it is lower than the uptake predicted for IRMOF-1 (~14 mmol/g) (Babarao et al. 2006).

Nonetheless surface modified STAC-1 is a promising material for CO_2 recovery from natural gas from landfills for two reasons: high CO_2 uptake, and good CO_2 selectivity on a wide range of pressures. Although, caution most be taken as to the type and number of surface groups being introduced to avoid pore blocking.

5.2. Power plants: CO_2 capture from flue gases

Coal and natural gas based power plants greatly contribute to the greenhouse effect by releasing significant amounts of CO_2 to the atmosphere. Although alternative energy sources (solar panels, wind farms, etc.) are at an advanced state of research, for the foreseeable future coal and natural gas power plants remain as the main source of electricity. For this reason resources are expended on finding a way to capture the CO_2 produced by these plants, and later store it in, for example, depleted oil reservoirs at deep seawater depths.

The composition of flue gases is mainly nitrogen (Desideri and Paolucci 1999) and carbon dioxide with some impurities. We study a simplified case by using a flue gas mixture consisting only of nitrogen and CO_2. From Desideri *et al.* (Desideri and Paolucci 1999) it can be seen that this is a reasonable assumption, since the nitrogen / carbon dioxide molar composition for dry flue gases (assuming water is fully removed) is 81 % / 14 % from coal power plants, and 87 % / 11 % from natural gas power plants. Thus, for the present section the mixture to be simulated is arbitrarily

composed of 85 % nitrogen and 15 % carbon dioxide. The Peng-Robinson binary interaction parameter for this mixture was taken as -0.013 (Al-Sahhaf 1990).

It is desirable that the adsorption process take place at ambient temperature (298 K) and pressures as close as possible to atmospheric conditions (around 1 bar), so these are the chosen simulation conditions. Adsorption predictions at these conditions are presented in Figure 5-3. Both CO_2 and N_2 are polar substances with the former having a stronger quadrupole. This fact coupled with the silanol groups covering the surface of the unmodified pore, and its nooks and crannies, which carbon dioxide can reach but nitrogen cannot due to its slightly larger size, are the factors responsible for the larger CO_2 uptake even in the unmodified model pore.

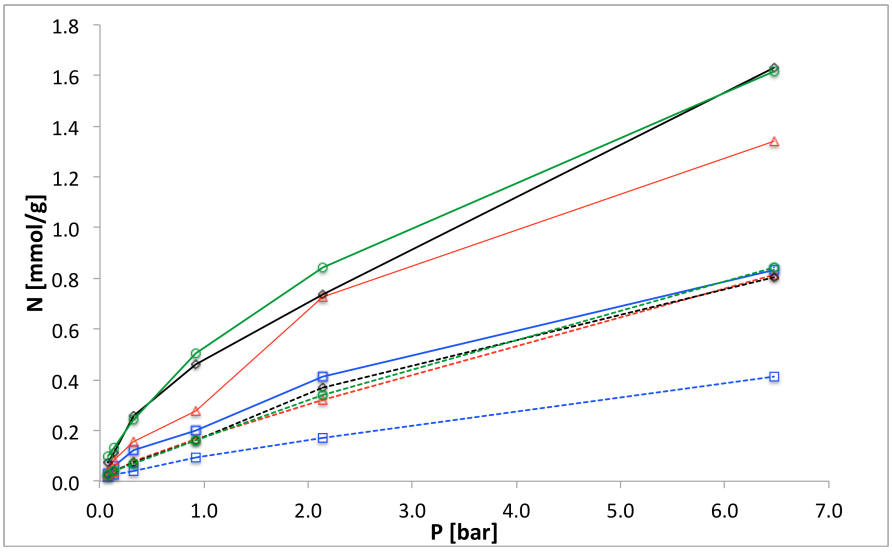

Figure 5-3: Adsorption predictions for binary CO_2 (solid lines) / N_2 (dotted lines, model N2-B) mixtures (y_{co2} = 0.15), using the unmodified STAC-1^E model (blue), and functionalised with: acetone (8 %, red), diamino-phenyl (8 %, black), and THF (9.8 %, green). Lines are a guide to the eye.

The carbon dioxide isotherm on the unmodified pore shows an inflexion step not shown by its nitrogen partner at pressures slightly larger that 1 bar, which may be a useful design parameter to look for enhanced selectivity. This inflexion is accentuated in the acetone functionalised model pore, but it is not present in the other functionalised pores. It seems that surface groups with stronger affinity for CO_2 smooth out the inflexion as a consequence of the increased CO_2 uptake at low

pressures. It can also be seen that nitrogen adsorption is enhanced by the presence of surface groups.

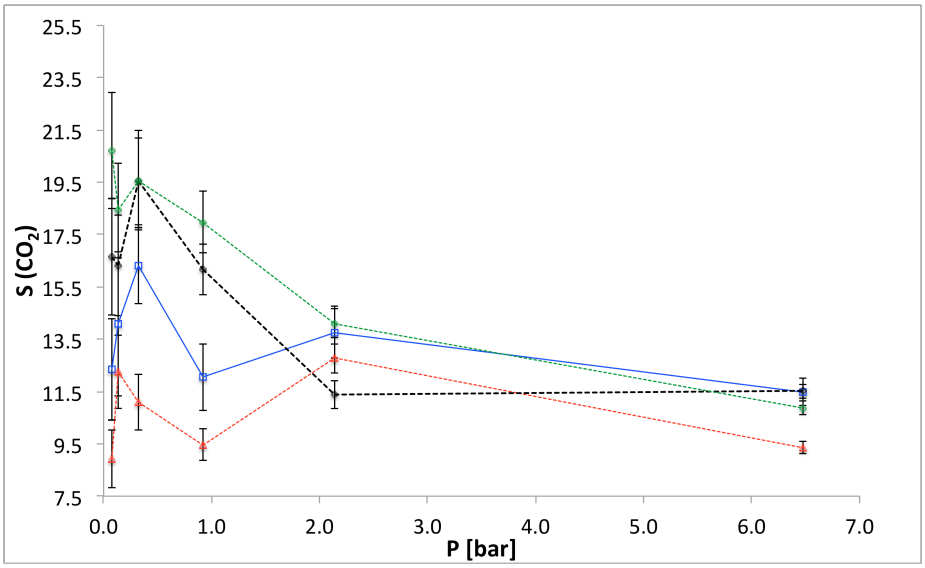

Figure 5-4: Selectivity predictions for binary CO_2 / N_2 mixtures (y_{co2} = 0.15). Using the unmodified STAC-1^E model pore (blue), and functionalised with: acetone (8 %, red), diamino-phenyl (8 %, black), and with THF (9.8 %, green). Lines are a guide to the eye.

Figure 5-4 shows the corresponding selectivity. At the lowest pressures, well below 1 bar, the surface groups present favour carbon dioxide adsorption over nitrogen, although this should be regarded with caution because the small number of adsorbate molecules at this pressures means these results are susceptible to statistical error (as seen by studying the error bars).

As the pressure increases the selectivity decreases. Both the diamino-phenyl and THF substituted model pores (8 % and 9.8 % respectively) provide greater affinity towards carbon dioxide at pressures bellow 1 bar, but for larger pressures it is apparent that only the THF substituted model pore can achieve a selectivity to match that of the unmodified pore. This means that the THF surface group introduces an effective polarity on the adsorbent surface greater than that of the original silanol groups, as does the diamino-phenyl groups, whether the small acetone molecules are unsuccessful on that regard. Even more, although acetone groups increase CO_2 uptake in the model pore as shown in Figure 5-3, it is clear that by also increasing the

N_2 uptake the selectivity is hindered and therefore this surface group, at this degree of functionalisation, does not improve the behaviour of the original silanol groups on the pore surface.

So far only ketone, amine, and ether-like (THF) groups have been used for comparison, but it is also worthwhile to see the effect of using a stronger electronegative group (like an acid). Figure 5-5 presents adsorption results on methyl-sulfonic acid functionalised model pores with different degree of functionalisation (1.6 %, 4.9 %, and 13.1 %). The most functionalised pore (13.1 %) exhibits a carbon dioxide uptake similar to the one obtained by the THF substituted model pore, and it can be seen that as the degree of functionalisation decreases so does the adsorption of carbon dioxide (the isotherm slope decreases), while the nitrogen uptake increases slightly. In other words, higher functionalised pores favour carbon dioxide selectivity (Figure 5-6).

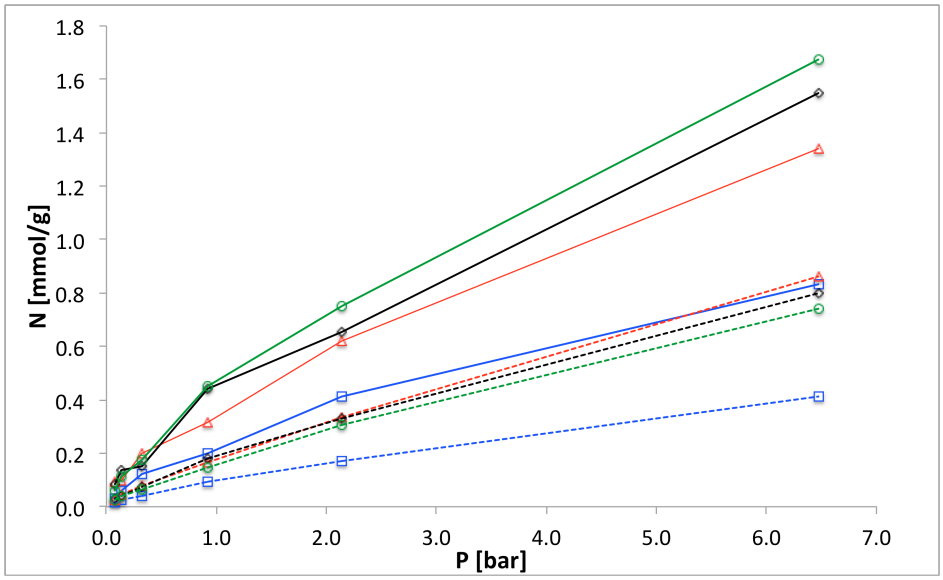

Figure 5-5: Study of the effect of surface group loading on the adsorption of CO_2 (solid lines) from a CO_2 / N_2 (dotted lines) mixture (y_{co2} = 0.15). Unmodified STAC-1^E model pore (blue), and methyl-sulfonic acid modified model pores: 1.6 % (red), 4.9 % (black), and 13.1 % (green). Lines are a guide to the eye.

At very low pressures the small amount adsorbed may introduce amplified oscillations on the selectivity calculations (due to statistical error), but at pressures

beyond 1 bar it is apparent that the selectivity increases with increasing degree of functionalisation. Note that for a small number of substitutions the selectivity is hindered respect to that of the unmodified model pore. Although the surface groups promote carbon dioxide uptake they also attract nitrogen molecules, and furthermore they may block CO_2 access to nooks and crannies on the pore wall originally out of reach for nitrogen.

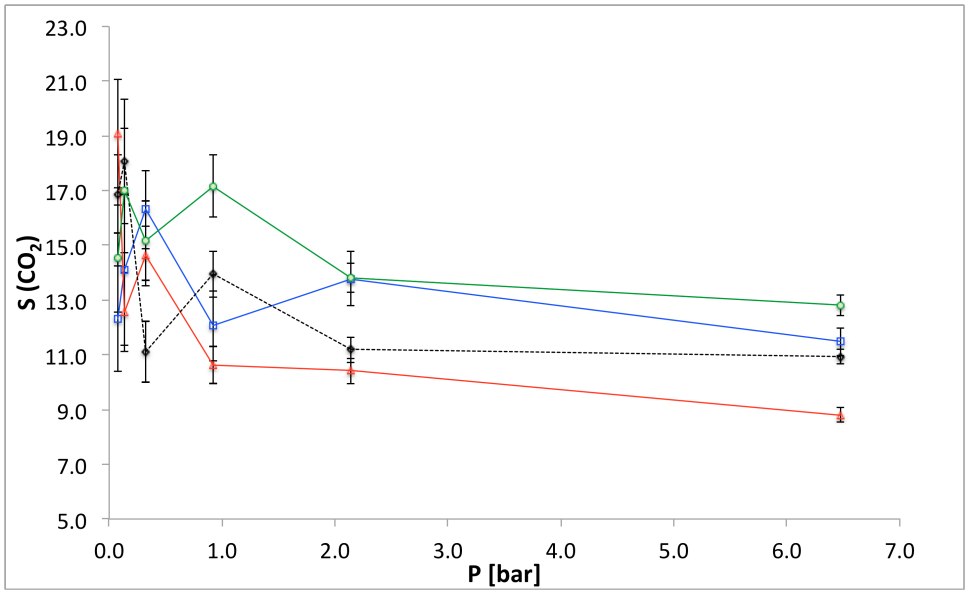

Figure 5-6: Selectivity predicted for the unmodified STAC-1^E model (blue) and for methyl-sulfonic modified model pores: 1.6 % (red), 4.9 % (black), and 13.1 % (green); for a CO_2 / N_2 mixture with y_{co2} = 0.15. Lines are a guide to the eye.

Although these results are specific for the surface group used, it would seem that there is a lower boundary for the degree of functionalisation of the pores, below which carbon dioxide selectivity over nitrogen is actually lower than for the unmodified material. However, their selectivity is still comparable to that of the unmodified pore, and the CO_2 uptake is greater (Figure 5-5), so overall they are still better than the unmodified pore for the desired application.

Once chosen a potential surface group to enhance carbon capture in these materials, it is then advisable to study the effect of its different degrees of functionalisation on the final selectivity at different pressures before moving to the experimental stage. Nonetheless, due to the nature of the pore connectivity in the

material the greater the degree of functionalisation the more likely for the pore connectivity to be negatively affected by pore blocking (closed connecting windows, as mentioned on Chapter 4), which is why a compromise between a high degree of functionalisation (leading to better selectivity and higher CO_2 loading) and high pore accessibility (favoured by lower degrees of functionalisation) has to be achieved.

5.2.1. Effect of the CO_2 / N_2 mixture composition

As was stated before the composition of the flue gases is related to its origin i.e. the type of fuel used to generate power. Flue gases from coal and natural gas fired power stations have a molar composition of carbon dioxide that is between 10 and 20 % (Desideri and Paolucci 1999). So, adsorption for three mixtures with carbon dioxide molar compositions of 10 %, 15 % and 20 % are presented in Figure 5-7 for the STAC-1^E model modified with methyl-sulfonic acid and 4.9 % degree of functionalisation (chosen arbitrarily as an example case).

As the carbon dioxide composition increases so does its adsorption on the material, while nitrogen uptake slowly decreases. Considering the small changes in composition the effect on adsorption is important, and there is an effect as well on the shape of the adsorption isotherms where there is an inflexion point at low pressures that accentuates with increasing carbon dioxide composition.

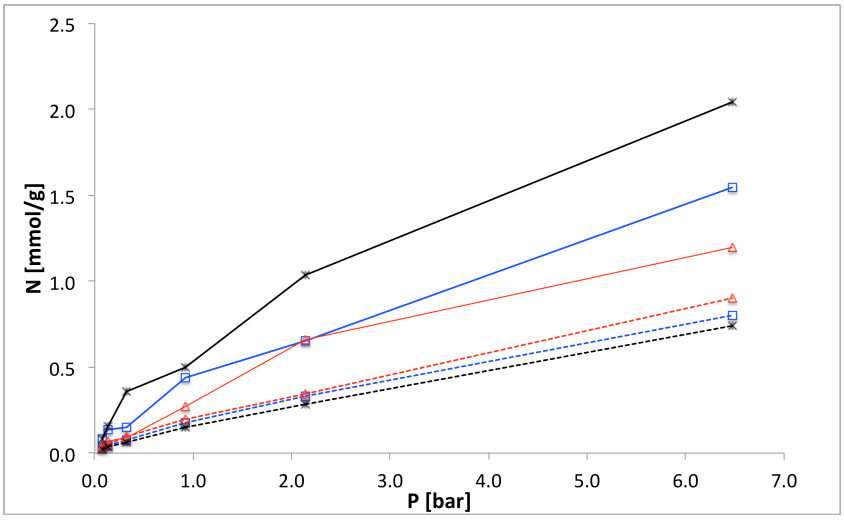

Figure 5-7: Effect of the CO_2 / N_2 mixture composition on adsorption. STAC-1^E model pore with methyl-sulfonic acid (4.9 %). y_{co2} = 0.1 (red), y_{co2} = 0.15, (blue), y_{co2} = 0.2 (black). Solid lines - CO_2 adsorption, dotted lines - N_2.

Figure 5-8 presents the corresponding selectivity. Again, selectivity oscillations at low pressures should be regarded with caution, but for pressures beyond 1 bar it appears as though there is a minimum for the selectivity within the range of compositions used. Further study of adsorption selectivity with varying carbon dioxide composition is then required to have more accurate information for potential industrial applications.

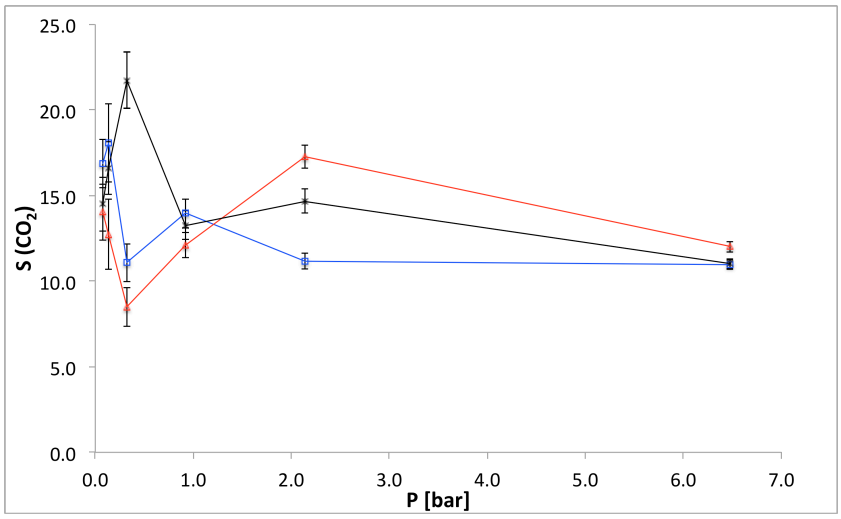

Figure 5-8: Predicted selectivity for CO_2 / N_2 mixtures with different CO_2 composition: 0.1 (red), 0.15 (blue), and 0.2 (black). STAC-1^E modified model pore with methyl-sulfonic acid (4.9 %).

5.3. Separation of isomers: n-butane and iso-butane

Synthesised SBA-2 from the same synthesis batch as the one used to obtain the experimental adsorption isotherms presented in Chapter 2 was used by Perez-Mendoza to produce the experimental isotherms of n-butane and iso-butane at 268 K (Perez-Mendoza 2007-2010). Figure 5-9 presents the experimental isotherm for n-butane and compares it to predictions using the PSD from a simple model (Perez-Mendoza 2007-2010) of smooth spheres interconnected by smooth cylinders, and to predictions by means of the SBA-2^{A} model pore (the STAC-1^{J} model would have also been a suitable choice for this study given its good predictions of adsorption for other adsorbates, as shown in Chapter 3). In both cases the adsorbates are represented by the UA-FF of Jorgensen *et al.* (Jorgensen et al. 1996), where n-butane molecules are flexible.

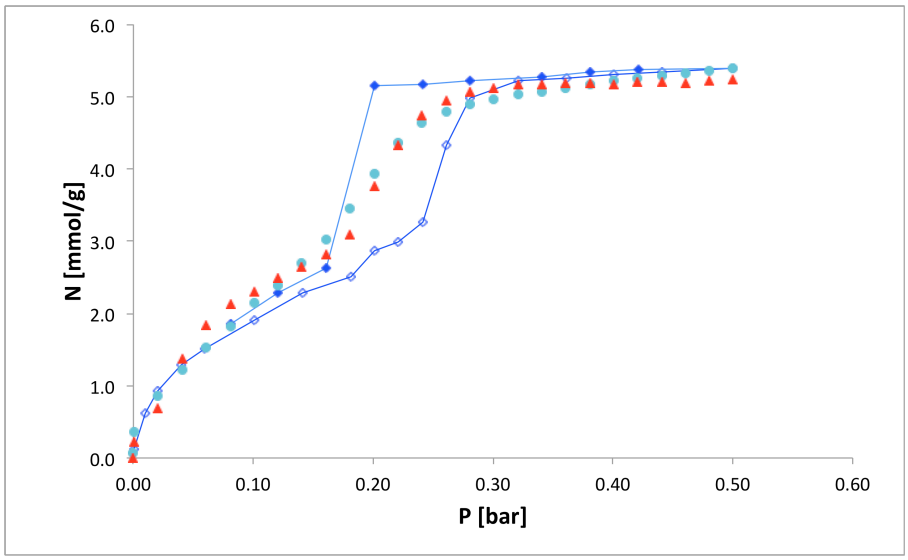

Figure 5-9: Experimental n-butane adsorption (cyan) compared to simulations: smooth model (red) PSD (Perez-Mendoza 2007-2010) and model SBA-2^{A} (F=0.77, adsorption in open blue diamonds, desorption in closed blue diamonds). The lines are a guide to the eye so that the hysteresis is clearly visible.

There is a good match between the predicted amounts adsorbed at low pressure and the experimental curve, but as the pressure reaches the transition range (from

0.15 bar up to 0.3 bar) the simulations predict a hysteresis loop that is not reported experimentally. The simulation of long chains (such as n-butane) is difficult and computationally intensive using GCMC simulation because of the difficulty in placing the molecules in a confined space as their number increases [a method called configurational biased Monte Carlo is used to enhance the simulation efficiency (Frenkel and Smit 2001)]. This makes attaining the true equilibration point difficult and thus the hysteresis observed is likely to be a product of the simulations rather than a real representation of the system.

The system can be further equilibrated by increasing the number of simulation steps, which is already high (7.5×10^6 equilibration steps and 3.25×10^6 sampling steps), but for the purpose of this work it suffices to note that the experimental transition from low to high adsorption pressures lies within the simulated hysteresis loop. Furthermore, it is remarkable that a single-pore model obtained with the kMC method gives predictions comparable to those of the PSD model and, safe for the hysteresis, closely mimics the shape of the experimental isotherm. This is an indication that the model pore correctly captures the solid-fluid interactions taking place in the system.

Iso-butane is modelled as a rigid molecule, and by looking at Figure 5-10 a similar conclusion can be reached. Figure 5-10 shows a close resemblance between the simulated amount adsorbed (model SBA-2^A) and the experimental results for iso-butane at low pressures, better even than the PSD model, which overpredicts the iso-butane loading. The SBA-2^A model pore is expected to overpredict the pore capacity as it happened for n-butane, but it turned out that the effect for this fluid is larger, the adjusting factor (F) being 0.53 as opposed to 0.77 found for n-butane. Since both the model pore and the material sample are the same, the remaining explanation is that the pore network in the experimental sample is less accessible to iso-butane than to n-butane, which supports the theory of using SBA-2 for molecular sieving.

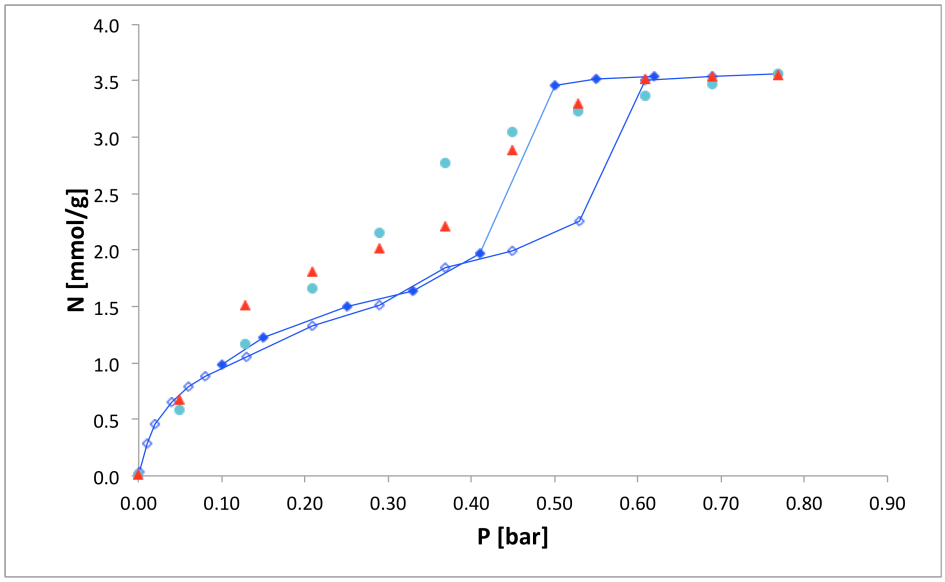

Figure 5-10: Experimental iso-butane adsorption (magenta) compared to simulations: smooth model (red) PSD (Perez-Mendoza 2007-2010), and model SBA-2^{A} (F=0.53, adsorption open diamonds, desorption closed diamonds). The lines are a guide to the eye so that the hysteresis is clearly visible.

From Figure 5-10 it is evident that both the PSD and the SBA-2^{A} models fail to give a good representation of iso-butane adsorption at pressures between 0.2 and 0.5 bar. The PSD model introduces a non-existent step in the isotherm, while the SBA-2^{A} model pore shows a hysteresis loop at pressures between 0.45 bar and 0.6 bar and clearly underpredicts iso-butane uptake between 0.2 bar and 0.45 bar, so that overall there is an indication that some feature of the experimental system is not being captured by the models. At these pressures the solid-fluid and fluid-fluid interactions are equally important. Judging by the different isotherms presented here it might be worth considering in future work whether the LJ parameters of the adsorbate, or its rigid representation are appropriate for the system being studied.

A binary mixture of these isomers is hard to separate by distillation. For the specific purpose of this example, at 268 K the saturation pressure for n-butane is 0.84586 bar while for iso-butane it is 1.3025 bar (Linstrom and Mallard 2003). This means the relative volatility is 0.6494 (<1.5), and thus adsorption is preferred over distillation.

Figure 5-11 presents the simulated adsorption of a binary n-butane / iso-butane mixture (y=0.5) in SBA-2^{A}. Clearly n-butane adsorption is favoured over iso-butane, which was expected due to the larger dispersion forces exerted by the linear chain as opposed to the symmetric isomer (where one carbon is shielded by the other three). Also, the higher flexibility of the n-butane molecules increases their probability of accommodating to the interaction sites offered by the solid, while the rigid iso-butane molecules cannot do this. The latter effect becomes more apparent as the number of molecules in the simulation cell increases. Thus, as the pressure rises n-butane molecules find it easier to squeeze their way in than the bulky iso-butane molecules. This results in a steeper slope for n-butane uptake than that of its isomer.

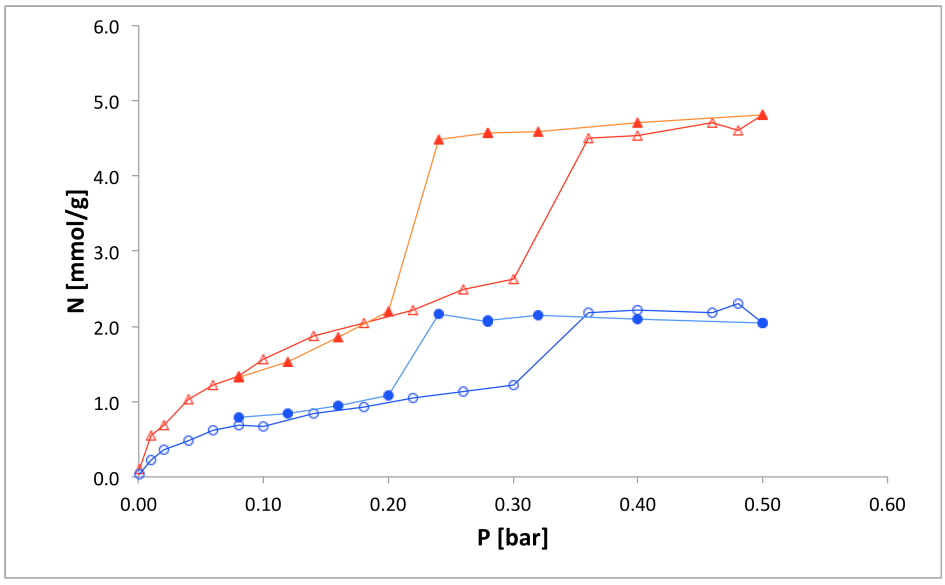

Figure 5-11: Predicted equimolar mixture adsorption of n-butane (red) and iso-butane (blue) at 268 K. Open symbols indicate adsorption while closed symbols are for desorption. The lines are meant as a guide to the eye only.

The hysteresis loop depicted in Figure 5-11 might be a feature of the simulations, as was seen for pure fluids adsorption, indicating that for GCMC simulations it is difficult to achieve the true system equilibration despite the large number of simulation steps (22.5×10^{6} equilibration steps and 7.5×10^{6} sampling steps).

In Figure 5-12 the selectivity (S_{nC4}) of n-butane is presented. The selectivity is calculated by Equation (5-2), where *x* and y are the mole fractions for n-butane in the

adsorbed and bulk phase respectively. Selectivity higher than one shows the adsorbent preferential adsorption of n-butane over the other mixture component.

$$S_{nC4} = \left(\frac{x_{nC4}}{y_{nC4}}\right)\left(\frac{1-y_{nC4}}{1-x_{nC4}}\right) \quad \textbf{(5-2)}$$

Thus, in Figure 5-12 the selectivity, which throughout the pressure range is rather constant, clearly indicates n-butane is the preferred adsorbed component in the model pore SBA-2^{A} (as expected from the adsorption isotherms discussed before). A selectivity of ~2.2 however is low for an efficient separation application.

In fact, rates of diffusion in the adsorbent have not been taken into account and it has already been shown from the pure fluid adsorption isotherms that n-butane has more access to the pore network than iso-butane. This feature should work in favour of increasing the selectivity presented here. Moreover, since the size and number of connections between the pores seem to be related to the calcination temperature [as indicated in Chapter 2, and also by (Gonzalez 2005) and (Prof. Wright 2007-2010)], this could be used as a design parameter for SBA-2 materials to improve n-butane selectivity by steric impediment.

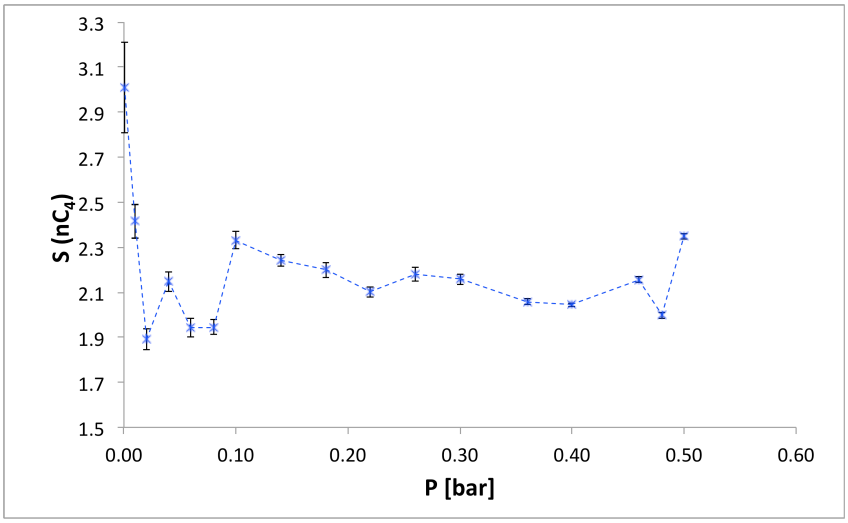

Figure 5-12: Expected selectivity for the n-butane iso-butane (y=0.5) mixture on SBA-2 at 268 K.

5.4. Concluding remarks

Non-grafted SBA-2 and STAC-1 materials show good carbon dioxide selectivity whether for flue gas or landfill gas carbon capture applications. Nonetheless CO_2 uptake is not high, especially when compared to materials grafted with either acetone, diamino-phenyl or THF. Overall it may be worth to consider these grafted materials for carbon capture from landfill gas since it takes place at high pressures and thus the large pore capacity of these materials can be advantageous.

However, it is unlikely that SBA-2 and STAC-1 can be successfully applied for carbon capture from flue gases where its CO_2 uptake at room temperature and atmospheric pressure is lower than that of the reference zeolite-13 (Konduru, Lindner and Assaf-Anid 2007), even for the grafted models considered here. Furthermore, it has been shown that both the selectivity and the CO_2 uptake in these materials are sensitive to small changes in the mixture composition which means the operational conditions for large scale applications would need to be carefully monitored.

For butane isomers separation, it has been shown that the non-grafted materials are n-butane selective, although the selectivity reported here is not the one to be observed experimentally. This is because adsorption simulations by GCMC do not take into account percolation, which by comparing our adsorption predictions to experimental measurements (Perez-Mendoza 2007-2010) clearly favours n-butane. In fact, by tailoring the size of the connecting windows the selectivity towards n-butane can be - theoretically - taken to infinity when molecular sieving takes place. Finally it has to be mentioned that the pure isotherm predictions for n-butane and iso-butane are not as accurate as those obtained for other species in previous chapters, particularly so for iso-butane, and this may indicate that there is a feature of the experimental system that is not being properly captured or that the potential model for the adsorbates are not adequate.

6. General Conclusions and Future Work

By means of the extended kMC technique realistic pore models for the complex periodic mesoporous silicas SBA-2 and STAC-1 were obtained. One of the most important features achieved was the simulated formation of the connections between spherical cavities as a direct result of the synthesis process without external intervention. Such windows match closely – in both size and direction – those presented by the experimentally synthesised materials, and were shown to be window-like rather than channel-like as previously assumed [(Perez-Mendoza et al. 2004a) and (Zhou et al. 1998)]. The nature of these connections is related to the spherical packing of the micelles, since they arise from model micelles touching during the aggregation stage of the synthesis. The presence of unbound oxygens near the micelle surface at this stage may play a role in the windows formation.

It is known from experimental studies that the size of the connections is somewhat related to the pore size obtained at a given calcination temperature (Gonzalez 2005). Investigating the size of these connections through simulations is not easy since other parameters (such as the number of silica monomers and the resulting pore wall density) need to be taken into account, but the kMC technique has confirmed that greater calcination temperatures contribute to a decrease in the number of connections between pores.

The effect of the calcination temperature on the pore size was assessed by calcining the same model pore at different temperatures (from 800K up to 2000K). Similarly to what happens experimentally (Prof. Wright 2007-2010) the pore size was shown to decrease with increasing temperature. For the highest temperature the reduction of the pore size is not as significant as the increase in the pore-wall density. In other words, the rate of contraction of the unit cell exceeds that of the pore radius and thus makes the walls more compact. Moreover, higher calcination temperatures also affect the pore connectivity (as stated above), and so by choosing the

appropriate calcination temperature these structural parameters can be tailored to favour the selectivity towards smaller adsorbates. This could prove very useful to, for example, increase selectivity towards n-butane by blocking iso-butane access to the pore network.

Overall, the kMC technique transferability to model the synthesis of mesoporous silicas with different structural characteristics is a remarkable achievement on its own. It may be interesting then to consider producing realistic models for other mesoporous materials (such as MCM-48 or SBA-15) by means of this technique, which will lead to a better understanding of their synthesis process as well as to better assess their potential for adsorption applications.

Adsorption predictions with either STAC-1 or SBA-2 model pores provided excellent agreement with experimental results. This is very important since experimentally both STAC-1 and SBA-2 materials are likely to co-exist within the same sample after synthesis. Since their pore network is different, this result supports that the connections are windows, since as such their contribution to the final amount adsorbed is very small compared to that of the spherical cavities.

The agreement obtained between the predicted and experimental nitrogen, methane, ethane and carbon dioxide isotherms is excellent by means of single pore models, better than other models presented in the literature (Perez-Mendoza et al. 2004a). Though it can be further improved by means of a pore size distribution (PSD), the improvement is negligible and the PSD shows an unrealistic bimodal distribution (when it is well known (Huo et al. 1996) that these materials have one preferential pore size, with a very sharp distribution). Also, by studying the LJ potential depth of the silica wall it was concluded that its value of 185 K originally derived for MCM-41 is suitable for use in the SBA-2 and STAC-1 pore models, although (if desired) it can be used as a fitting parameter: by lowering it to counteract the effect of the excessive roughness presented by some models, thus decreasing the solid-fluid interactions.

It has also been shown that the pore models are valuable tools in adsorbent design, since they provide model-locations for the silanol groups in the wall, and thus a means to substitute them by surface groups in a similar way as it happens experimentally during post-synthesis modification. Using ether, ester, acids, nitrile and amine groups in turn the uptake of CO_2 (specially at low pressures) was significantly improved.

Large surface groups, and higher degree of functionalisation of the pore model were shown to have a negative effect on the pore capacity and on its connectivity – in some cases blocking the pore connections (i.e. diamino-phenyl at 8 %). Therefore, despite big, rigid surface groups being desirable to project the functional groups further into the pore and enhance adsorption at low pressures, they are not necessarily the best choice. Also, since reactions can take place between the amine groups and carbon dioxide making the regeneration of the adsorbent difficult, it would be very valuable for these materials if it were possible to take physical CO_2 absorbent molecules (such as polyethylene glycol –PEG, or tetrahydrofuran -THF) and use them as surface groups.

Mixture separation applications were presented to predict the scope of applicability for these materials. Simulation of carbon capture applications showed that CO_2 uptake at low pressures is good for the unmodified materials, but can be further improved by introducing surface groups, though care must be taken as to their type and the degree of functionalisation used, since these parameters greatly affect the selectivity. In the case of carbon capture from flue gas, where the CO_2 composition may vary depending on its origin (roughly between 10 and 20 %), a sensibility study on this composition showed that it has an important effect on both the final carbon dioxide uptake and the selectivity of the adsorbent. Using THF molecules as surface groups at 9.8 % degree of functionalisation gave the best results for this separation. In general, it is not the electronegativity of the surface groups but rather their projection into the pore cavity and the exposure of their functional groups what had the most impact on CO_2 uptake and selectivity.

The simulation of the separation of n-butane and iso-butane isomers was also presented. The pure fluid n-butane isotherm showed good agreement with experimental results. The iso-butane isotherm however showed good agreement at low and high pressures, but was unable to properly predict the amount adsorbed in the pressure range between 0.2 and 0.5 bar. The mixture predictions indicated n-butane selectivity between 2 and 3 for a large range of pressures. This is a good indication of what might be expected, but by closer inspection of the pure fluid isotherms it was seen that the accessibility of n-butane within the material is larger than that of iso-butane. This indicates that there is a larger fraction of the porous material capable of trapping n-butane molecules and thus it is likely that the experimental mixture selectivity will be larger than the one predicted by the model pore, where it is assumed that both n-butane and iso-butane have the same accessibility within the material. Furthermore, this is a clear indication that if the size of the connections could be further tailored for this mixture to exclude accessibility for iso-butane, the selectivity of this material towards n-butane could be greatly increased.

The main goal of this work of obtaining realistic pore models for SBA-2 has been achieved, and it exceeded expectations by providing valuable insight into the formation of pore connections. In addition, it lead to a better understanding of their synthesis process and their use as adsorbents. However, there are many aspects that are worth considering for future work, some that were not studied here and some that emerged as a consequence of this thesis.

For instance, during the polymerisation of silica in the kMC simulations it was found that the contribution of the resulting unbound oxygens was significant to promote the reaction, thus indicating that they should not be assumed to diffuse rapidly as was done for MCM-41 (Schumacher et al. 2006b). Nonetheless in the true reaction water molecules are produced, and thus their explicit inclusion in the simulation should be the subject of future study to better understand their effect on both the size of the connecting windows and on the pore topology (since they move towards the surface of the micelles). This relates well with observations in other

mesoporous materials with cubic symmetry (Atluri et al. 2010) where it is indicated that the windows formation is related to the hydration layer formed at the surfactant-silica interface.

However, for a study at this level of detail the charge density synthesis mechanism (Corma 1997) might be more adequate, specially since the charge density at the surfactant heads may be an important parameter in determining the windows size (Atluri et al. 2010) if the effect of the water molecules at the silica-micelle interface is found to be important.

The roughness of the pore surface varies between model pores and it greatly affects adsorption at low pressures, especially for small non-polar adsorbates like methane. There is a need then to find a simulation tool that helps tailoring the final roughness in the models, as it may be correlating it to the initial model micelle parameters, or to the final model pore size and/or number of silica monomers.

On the other hand further research is needed to study bond-percolation in both STAC-1 and SBA-2 materials, as well as to better identify the impact of the synthesis conditions on the final number and size of connections. This may lead to important information of how to improve the behaviour of these materials as molecular sieve adsorbents. Although this is bound to be computationally expensive, alternative ways may be presented to tackle the problem, as for example finding a distribution of connection sizes for different model pores of similar pore size and using it as an input for the bond percolation problem.

Making experimental work on SBA-2 post-synthesis functionalisation using surface groups such as the ones presented in this work will provide useful information to validate results, as well as to better understand the extent to which the pore connectivity is affected by the size of the surface group molecules and the degree of functionalisation of the sample. It is also recommended to measure the extent to which experimental mixture adsorptions compares to predictions, since it would be advantageous to assess the impact of these pore models as design tools for

potential applications such as the ones mentioned in this work. Finally, further investigating the use of SBA-2 on the separation of other isomers may provide a valuable base for comparison with the already studied n-butane / iso-butane separation and its perspective for molecular sieving.

7. References

Al-Sahhaf, T. A. (1990) Vapor--liquid equilibria for the ternary system N2 + CO2 + CH4 at 230 and 250 K. *Fluid Phase Equilibria,* 55**,** 159-172.

Arfken, G. 1985. *The Method of Steepest Descents*. Orlando: Academic Press.

Atluri, R., Z. Bacsik, N. Hedin & A. E. Garcia-Bennett (2010) Structural variations in mesoporous materials with cubic Pmn symmetry. *Microporous and Mesoporous Materials,* 133**,** 27-35.

Atluri, R., N. Hedin & A. E. Garcia-Bennett (2008) Hydrothermal Phase Transformation of Bicontinuous Cubic Mesoporous Material AMS-6. *Chemistry of Materials,* 20**,** 3857-3866.

Babarao, R., Z. Hu, J. Jiang, S. Chempath & S. I. Sandler (2006) Storage and Separation of CO_2 and CH_4 in Silicalite, C_{168} Schwarzite, and IRMOF-1: A Comparative Study from Monte Carlo Simulation. *Langmuir,* 23**,** 659-666.

Bacsik, Z., R. Atluri, A. E. Garcia-Bennett & N. Hedin (2010a) Temperature-Induced Uptake of CO2 and Formation of Carbamates in Mesocaged Silica Modified with n-Propylamines. *Langmuir,* 26**,** 10013-10024.

Bacsik, Z. n., R. Atluri, A. E. Garcia-Bennett & N. Hedin (2010b) Temperature-Induced Uptake of CO2 and Formation of Carbamates in Mesocaged Silica Modified with n-Propylamines. *Langmuir,* 26**,** 10013-10024.

Battaile, C. C. (2008) The Kinetic Monte Carlo method: Foundation, implementation, and application. *Computer Methods in Applied Mechanics and Engineering,* 197**,** 3386-3398.

Battaile, C. C. & D. J. Srolovitz (2002) KINETIC MONTE CARLO SIMULATION OF CHEMICAL VAPOR DEPOSITION. *Annual Review of Materials Research,* 32**,** 297-319.

Bera, S. & I. Manna (2006) Hexagonal close packed to face centered cubic polymorphic transformation in nanocrystalline titanium-zirconium system by mechanical alloying. *Journal of Alloys and Compounds,* 417**,** 104-108.

Bezus, A. G., A. V. Kiselev, A. A. Lopatkin & P. Q. Du (1978) Molecular statistical calculation of the thermodynamic adsorption characteristics of zeolites using the atom-atom approximation. Part 1.-Adsorption of methane by zeolite NaX. *Journal of the Chemical Society, Faraday Transactions 2: Molecular and Chemical Physics,* 74**,** 367-379.

Blanc, E. & et al. (1996) X-ray diffraction study of the stacking faults in hexagonal C 70 single crystals. *EPL (Europhysics Letters),* 33**,** 205.

Briggs, J. M., T. B. Nguyen & W. L. Jorgensen (1991) Monte Carlo simulations of liquid acetic acid and methyl acetate with the OPLS potential functions. *The Journal of Physical Chemistry,* 95**,** 3315-3322.

Catlow, C. R. A., L. Ackermann, R. G. Bell, F. Cora, D. H. Gay, M. A. Nygren, J. C. Pereira, G. Sastre, B. Slater & P. E. Sinclair (1997) Computer modelling as a technique in solid state chemistry - Introductory lecture. *Faraday Discussions***,** 1-40.

Cavenati, S., C. A. Grande & A. r. E. Rodrigues (2006) Removal of Carbon Dioxide from Natural Gas by Vacuum Pressure Swing Adsorption. *Energy & Fuels,* 20**,** 2648-2659.

CECAM. 2010. Centre Europeen de Calcule Atomique et Moleculaire. ed. E. P. F. d. Lausanne. Lausanne.

Chang, A. C. C., S. S. C. Chuang, M. Gray & Y. Soong (2003) In-Situ Infrared Study of CO2 Adsorption on SBA-15 Grafted with Î³-(Aminopropyl)triethoxysilane. *Energy & Fuels,* 17**,** 468-473.

Corma, A. (1997) From microporous to mesoporous molecular sieve materials and their use in catalysis. *Chemical Reviews,* 97**,** 2373-2419.

Dacquin, J.-P., H. E. Cross, D. R. Brown, T. Duren, J. J. Williams, A. F. Lee & K. Wilson (2010) Interdependent lateral interactions, hydrophobicity and acid strength and their influence on the catalytic activity of nanoporous sulfonic acid silicas. *Green Chemistry,* 12**,** 1383-1391.

Davies, G. M., N. A. Seaton & V. S. Vassiliadis (1999) Calculation of pore size distributions of activated carbons from adsorption isotherms. *Langmuir,* 15**,** 8235-8245.

Delgado, J., M. Uguina, J. Sotelo, B. Ruíz & M. Rosário (2007) Separation of carbon dioxide/methane mixtures by adsorption on a basic resin. *Adsorption,* 13**,** 373-383.

Desideri, U. & A. Paolucci (1999) Performance modelling of a carbon dioxide removal system for power plants. *Energy Conversion and Management,* 40**,** 1899-1915.

Düren, T. 2002. Molecular modelling of equilibrium adsorption and transport diffusion in microporous solids. Hamburg: Technischen Universitat Hamburgh.

Düren, T., Y. S. Bae & R. Q. Snurr (2009) Using molecular simulation to characterise metal-organic frameworks for adsorption applications. *Chemical Society Reviews,* 38**,** 1237-1247.

Düren, T., F. Millange, G. Férey, K. S. Walton & R. Q. Snurr (2007) Calculating Geometric Surface Areas as a Characterization Tool for Metal−Organic Frameworks. *The Journal of Physical Chemistry C,* 111**,** 15350-15356.

Düren, T. & R. Q. Snurr (2007) Using molecular simulation to characterise metal-organic frameworks and judge their performance as adsorbents. *Characterisation of porous solids VII, Studies in Surface Science and Catalysis,* 160-161.

Ebenezer, S. A. 2005. Removal of Carbon Dioxide from Natural Gas for LNG Production. Trondheim, Norway: Institute of Petroleum Technology, Norwegian University of Science and Technology.

Fiaschi, D. & L. Lombardi (2002) Integrated Gasifier Combined Cycle Plant with Integrated CO2-H2S Removal: Performance Analysis, Life Cycle Assessment and Exergtic Life Cycle Assessment. *International Journal of Applied Thermodynamics,* 5**,** 13-24.

Firouzi, A., D. Kumar, L. Bull, T. Besier, P. Sieger, Q. Huo, S. Walker, J. Zasadzinski, C. Glinka & J. Nicol (1995) Cooperative organization of inorganic-surfactant and biomimetic assemblies. *Science,* 267**,** 1138-1143.

Frenkel, D. & B. Smit. 2001. *Understanding Molecular Simulation, Second Edition: From Algorithms to Applications (Computational Science Series, Vol 1)*. Academic Press.

Gadelmawla, E. S., M. M. Koura, T. M. A. Maksoud, I. M. Elewa & H. H. Soliman (2002) Roughness parameters. *Journal of Materials Processing Technology,* 123**,** 133-145.

García-Pérez, E., J. Parra, C. Ania, A. García-Sánchez, J. van Baten, R. Krishna, D. Dubbeldam & S. Calero (2007) A computational study of CO2, N2, and CH4 adsorption in zeolites. *Adsorption,* 13**,** 469-476.

Garofalini, S. H. & G. Martin (1994) Molecular Simulations of the Polymerization of Silicic Acid Molecules and Network Formation. *The Journal of Physical Chemistry,* 98**,** 1311-1316.

Girard, S. & F. Müller-Plathe (2003) Molecular dynamics simulation of liquid tetrahydrofuran: on the uniqueness of force fields. *Molecular Physics: An International Journal at the Interface Between Chemistry and Physics,* 101**,** 779-787.

Girard, S. e. a. (2003) Molecular dynamics simulation of liquid tetrahydrofuran: on the uniqueness of force fields. *Molecular Physics: An International Journal at the Interface Between Chemistry and Physics,* 101**,** 779-787.

Gonzalez, J. 2005. Adsorption properties of organically functionalised mesoporous solids and dynamics of adsorbed molecules in miroporous organic-inorganic hybrid solids. In *Chemistry*. St. Andrews, UK: University of St. Andrews.

Harris, J. G. & K. H. Yung (1995) Carbon Dioxide's Liquid-Vapor Coexistence Curve And Critical Properties as Predicted by a Simple Molecular Model. *The Journal of Physical Chemistry,* 99**,** 12021-12024.

Herdes, C., C. Ferreiro & T. Duren. 2011. Predicting neopentane isosteric enthalpy of adsorption at zero coverage in MCM-41. In *Langmuir (in revision)*.

Hill, T. L. 1956. *Statistical Mechanics: Principles and Selected Applications*. USA: McGraw-Hill.

Hunter, H. M. & P. A. Wright (2001) Synthesis and characterisation of the mesoporous silicate SBA-2 and its performance as an acid catalyst. *Microporous and Mesoporous Materials,* 43**,** 361-373.

Huo, Q., D. I. Margolese, U. Ciesla, D. G. Demuth, P. Feng, T. E. Gier, P. Sieger, A. Firouzi & B. F. Chmelka (1994a) Organization of Organic Molecules with Inorganic Molecular Species into Nanocomposite Biphase Arrays. *Chemistry of Materials,* 6**,** 1176-1191.

Huo, Q. S., R. Leon, P. M. Petroff & G. D. Stucky (1995) Mesostructure Design with Gemini Surfactants - Supercage Formation in a 3-Dimensional Hexagonal Array. *Science,* 268**,** 1324-1327.

Huo, Q. S., D. I. Margolese, U. Ciesla, P. Y. Feng, T. E. Gier, P. Sieger, R. Leon, P. M. Petroff, F. Schuth & G. D. Stucky (1994b) Generalized Synthesis of Periodic Surfactant Inorganic Composite-Materials. *Nature,* 368**,** 317-321.

Huo, Q. S., D. I. Margolese & G. D. Stucky (1996) Surfactant control of phases in the synthesis of mesoporous silica-based materials. *Chemistry of Materials,* 8**,** 1147-1160.

Jorgensen, W. L., J. M. Briggs & M. L. Contreras (1990) Relative partition coefficients for organic solutes from fluid simulations. *The Journal of Physical Chemistry,* 94**,** 1683-1686.

Jorgensen, W. L., J. D. Madura & C. J. Swenson (1984) Optimized Intermolecular Potential Functions for Liquid Hydrocarbons. *Journal of the American Chemical Society,* 106**,** 6638-6646.

Jorgensen, W. L., D. S. Maxwell & J. TiradoRives (1996) Development and testing of the OPLS all-atom force field on conformational energetics and properties of organic liquids. *Journal of the American Chemical Society,* 118**,** 11225-11236.

Kalke, M. & D. V. Baxter (2001) A kinetic Monte Carlo simulation of chemical vapor deposition: non-monotonic variation of surface roughness with growth temperature. *Surface Science,* 477**,** 95-101.

Kamath, G., G. Georgiev & J. J. Potoff (2005) Molecular Modeling of Phase Behavior and Microstructure of Acetoneâˆ'Chloroformâˆ'Methanol Binary Mixtures. *The Journal of Physical Chemistry B,* 109**,** 19463-19473.

Kim, J. M. & G. D. Stucky (2000) Synthesis of highly ordered mesoporous silica materials using sodium silicate and amphiphilic block copolymers. *Chemical Communications***,** 1159-1160.

Knofel, C., C. Martin, V. Hornebecq & P. L. Llewellyn (2009) Study of Carbon Dioxide Adsorption on Mesoporous Aminopropylsilane-Functionalized Silica and Titania Combining Microcalorimetry and in Situ Infrared Spectroscopy. *The Journal of Physical Chemistry C,* 113**,** 21726-21734.

Konduru, N., P. Lindner & N. M. Assaf-Anid (2007) Curbing the greenhouse effect by carbon dioxide adsorption with Zeolite 13X. *AIChE Journal,* 53**,** 3137-3143.

Kratzer, P. (2009) Monte Carlo and Kinetic Monte Carlo Methods - A Tutorial. *Multiscale Simulation Methods in Molecular Sciences,* 42**,** 51-76.

Kresge, C. T., M. E. Leonowicz, W. J. Roth, J. C. Vartuli & J. S. Beck (1992) Ordered Mesoporous Molecular-Sieves Synthesized by a Liquid-Crystal Template Mechanism. *Nature,* 359**,** 710-712.

Lanza, G. & C. Minichino (2009) How an Inert-Gas Matrix Can Modify the Molecular Properties of Lanthanide Trifluoride. *ChemPhysChem,* 10**,** 507-511.

Lin, H.-m. (1984) Peng-Robinson equation of state for vapor-liquid equilibrium calculations for carbon dioxide + hydrocarbon mixtures. *Fluid Phase Equilibria,* 16**,** 151-169.

Linstrom, P. J. & W. G. Mallard. 2003. *Thermophysical Properties of Fluid Systems in NIST Chemistry WebBook*. Gaithersburgh MC: National Institute of Standards and Technology.

Lu, G. Q. & X. S. Zhao. 2004. *Nanoporous Materials - Science and Engineering*. London: World Scientific.

Murthy, C. S., K. Singer, M. L. Klein & I. R. McDonald (1980) Pairwise additive effective potentials for nitrogen. *Molecular Physics: An International Journal at the Interface Between Chemistry and Physics,* 41**,** 1387 - 1399.

Myers, A. L. & P. A. Monson (2002) Adsorption in Porous Materials at High Pressure: Theory and Experiment. *Langmuir,* 18**,** 10261-10273.

Ng, L. V. & A. V. McCormick (1996) Acidic sol-gel polymerization of TEOS: Effect of solution composition on cyclization and bimolecular condensation rates. *Journal of Physical Chemistry,* 100**,** 12517-12531.

Nicholson, D. & E. Gubbins (1996) Separation of carbon dioxide-methane mixtures by adsorption: Effects of geometry and energetics on selectivity. *J. Chem. Phys,* 104**,** 8126-8134.
Perez-Mendoza, M., J. Gonzalez, P. A. Wright & N. A. Seaton (2004a) Elucidation of the pore structure of SBA-2 using Monte Carlo simulation to interpret experimental data for the adsorption of light hydrocarbons. *Langmuir,* 20**,** 7653-7658.
--- (2004b) Structure of the mesoporous silica SBA-2, determined by a percolation analysis of adsorption. *Langmuir,* 20**,** 9856-9860.
Perez-Mendoza, M. J. 2007-2010. personal reference. Universidad de Granada, Spain.
Press, W. H., B. P. Flannery, S. A. Teukolsky & W. T. Vetterling. 1992. *Numerical Recipes in FORTRAN: The Art of Scientific Computing*. Cambridge, England: Cambridge University Press.
Prof. Wright, r. g. 2007-2010. personal reference. University of St. Andrews.
Reuter, K. & M. Scheffler (2006) First-principles kinetic Monte Carlo simulations for heterogeneous catalysis: Application to the CO oxidation at RuO_{2}(110). *Physical Review B,* 73**,** 045433.
Richardi, J., P. H. Fries, R. Fischer, S. Rast & H. Krienke (1997) Structure and thermodynamic of liquid acetonitrile via Monte Carlo simulation and Ornstein-Zernike theories. *Journal of Molecular Liquids,* 74,74**,** 465-485.
Rouquerol, F., J. Rouquerol & K. Sing. 1999. *Adsorption by Powder & Porous Solid*. London: Academic Press.
Sandler, S. I. 1999. *Chemical and Engineering Thermodynamics*. USA: Wiley.
Sarnthein, J., A. Pasquarello & R. Car (1995) Model of Vitreous Sio2 Generated by an Ab-Initio Molecular-Dynamics Quench from the Melt. *Physical Review B,* 52**,** 12690-12695.
Schumacher, C. 2005. Design of Hybrid Organic/Inorganic Adsorbents for Gas Separation. In *Institute for Materials and Processes*. Edinburgh: The University of Edinburgh.
Schumacher, C., J. Gonzalez, M. Perez-Mendoza, P. A. Wright & N. A. Seaton (2006a) Design of hybrid organic/inorganic adsorbents based on periodic mesoporous silica. *Industrial & Engineering Chemistry Research,* 45**,** 5586-5597.
Schumacher, C., J. Gonzalez, P. A. Wright & N. A. Seaton (2006b) Generation of atomistic models of periodic mesoporous silica by kinetic Monte Carlo simulation of the synthesis of the material. *Journal of Physical Chemistry B,* 110**,** 319-333.
Serna-Guerrero, R., Y. Belmabkhout & A. Sayari (2010) Modeling CO2 adsorption on amine-functionalized mesoporous silica: 1. A semi-empirical equilibrium model. *Chemical Engineering Journal,* 161**,** 173-181.
Stoll, J., J. Vrabec & H. Hasse (2003) Vapor-liquid equilibria of mixtures containing nitrogen, oxygen, carbon dioxide, and ethane. *Aiche Journal,* 49**,** 2187-2198.
Sweatman, M. B. (2010) Equilibrium behaviour of a novel gas separation process, with application to carbon capture. *Chemical Engineering Science,* 65**,** 3907-3913.
Talu, O. & A. L. Myers (2001) Molecular simulation of adsorption: Gibbs dividing surface and comparison with experiment. *Aiche Journal,* 47**,** 1160-1168.

Torrens, F. & G. Castellano (2006) Fractal Dimension of Active-Site Models of Zeolite Catalysts. *Journal of Nanomaterials,* 2006**,** 17052.
Tu, Y. & J. Tersoff (2000) Structure and energetics of the Si-SiO2 interface. *Physical Review Letters,* 84**,** 4393-4396.
UK Research Council, U. (2011) Carbon Capture and Storage. http://www.co2storage.org.uk/ (last accessed.
van Wylen, G. J. & R. E. Sonntag. 1986. *Fundamentals of Classical Thermodynamics*. John Wiley & Sons Inc.
Varn, D. P., G. S. Canright & J. P. Crutchfield (2002) Discovering planar disorder in close-packed structures from x-ray diffraction: Beyond the fault model. *Physical Review B,* 66**,** 174110.
Voter, A. F. (2005) Introduction to the Kinetic Monte Carlo Method.
Williams, J. J., A. D. Wiersum, N. A. Seaton & T. DuÌˆren (2010a) Effect of Surface Group Functionalization on the CO2/N2 Separation Properties of MCM-41: A Grand-Canonical Monte Carlo Simulation Study. *The Journal of Physical Chemistry C,* 114**,** 18538-18547.
Williams, J. J., A. D. Wiersum, N. A. Seaton & T. Düren (2010b) Effect of Surface Group Functionalization on the CO2/N2 Separation Properties of MCM-41: A Grand-Canonical Monte Carlo Simulation Study. *The Journal of Physical Chemistry C,* 114**,** 18538-18547.
Wu, M. G. & M. W. Deem (2002) Monte Carlo study of the nucleation process during zeolite synthesis. *Journal of Chemical Physics,* 116**,** 2125-2137.
Yang, R. T. 1997. *Gas separation by adsorption processes*. Singapore.
Yun, J.-H., T. Düren, F. J. Keil & N. A. Seaton (2002) Adsorption of Methane, Ethane, and Their Binary Mixtures on MCM-41: Experimental Evaluation of Methods for the Prediction of Adsorption Equilibrium. *Langmuir,* 18**,** 2693-2701.
Zelenak, V., D. Halamova, L. Gaberova, E. Bloch & P. Llewellyn (2008) Amine-modified SBA-12 mesoporous silica for carbon dioxide capture: Effect of amine basicity on sorption properties. *Microporous and Mesoporous Materials,* 116**,** 358-364.
Zhao, D. Y., Q. S. Huo, J. L. Feng, B. F. Chmelka & G. D. Stucky (1998) Nonionic triblock and star diblock copolymer and oligomeric surfactant syntheses of highly ordered, hydrothermally stable, mesoporous silica structures. *Journal of the American Chemical Society,* 120**,** 6024-6036.
Zhou, W. Z., H. M. A. Hunter, P. A. Wright, Q. F. Ge & J. M. Thomas (1998) Imaging the pore structure and polytypic intergrowths in mesoporous silica. *Journal of Physical Chemistry B,* 102**,** 6933-6936.

8. Appendices

8.1. Force field data for the surface groups

Table A-1: LJ sites and charges for the surface groups (the charges may differ from the references since they have been adjusted to keep cell neutrality).*

Group	Bids	Sites	ε_{ii}/k_B [kcal/mol]	σ_{ii} [Å]	q_i [e0] *	Ref **
Amino-methyl	CH_2	UA	0.118	3.905	-0.14	(Schumacher et al. 2006a)
	NH_2	N	0.170	3.300	-0.90	
		H	-	-	+0.36	
		H	-	-	+0.36	
Amino-propyl	CH_2	UA	0.118	3.905	-0.32	(Schumacher et al. 2006a)
	CH_2	UA	0.118	3.905	0.12	
	CH_2	UA	0.118	3.905	0.06	
	NH_2	N	0.170	3.300	-0.90	
		H	-	-	0.36	
		H	-	-	0.36	
Diamino-phenyl	C_6H_3 (UA)	C^a	0.11	3.75	-0.12	(Williams et al. 2010a)
		CH^i	0.11	3.75	-0.10	
		C^b	0.07	3.55	0.18	
		CH^{ii}	0.11	3.75	-	
		C^c	0.07	3.55	0.18	
		CH^{iii}	0.11	3.75	-0.10	
	NH_2	N	0.17	3.30	-0.90	
		H	-	-	0.36	
		H	-	-	0.36	
Aceto-nitrile	CH_2	UA	0.118	3.905	-0.14	(Richardi et al. 1997)
	C		0.15	3.650	0.28	
	N		0.17	3.200	-0.43	

PEG	CH_2^a	UA	0.118	3.905	-0.320	(Jorgensen et al. 1984)
	CH_2^b	UA	0.118	3.905	0.200	(Jorgensen et al. 1996)
	O		0.140	2.900	-0.400	(Schumacher et al.
	CH_2^c	UA	0.118	3.905	0.265	2006a)
	OH	O	0.17	3.120	-0.683	
		H	-	-	0.418	
THF ****	THF	CH^2	0.118	3.850	-0.32	(Girard 2003)
	(UA)	CH_2^3	0.118	3.850	0.10	
		CH_2^4	0.118	3.850	0.15	
		CH_2^1	0.118	3.850	0.25	
		O	0.170	3.000	-0.50	
Acetone	CH_2	UA	0.118	3.905	-0.32	(Kamath, Georgiev and
	C		0.105	3.750	0.300	Potoff 2005)
	O		0.210	2.960	-0.424	(Jorgensen et al. 1996)
	CH_3	UA	0.16	3.910	0.062	
Methyl-	CH_2	UA	0.118	3.905	-0.320	(Briggs, Nguyen and
acetate						Jorgensen 1991)
	C		0.105	3.750	0.550	
	O=		0.210	2.960	-0.450	
	O-		0.170	3.000	-0.400	
	CH_3	UA	0.170	3.800	0.250	
Propanoic	CH_2^a	UA	0.118	3.905	-0.320	(Briggs et al. 1991)
acid	CH_2^b	UA	0.118	3.905	-	
	CH_2^c	UA	0.118	3.905	0.080	
	C		0.105	3.750	0.550	
	O=		0.210	2.960	-0.500	
	O-		0.170	3.000	-0.580	
	H		-	-	0.450	

Benzoic	C_6H_3	C^1	0.11	3.75	-0.120	(Williams et al. 2010b)
acid	(UA)	CH^i	0.11	3.75	-0.100	(Jorgensen et al. 1996)
		CH^{ii}	0.11	3.75	0.180	
		C^2	0.07	3.55	-	
		CH^{iii}	0.11	3.75	0.180	
		CH^{iv}	0.11	3.75	-0.100	
	COOH	C	0.105	3.75	0.520	
		O=	0.21	2.96	-0.440	
		O-	0.17	3.00	-0.530	
		H	-	-	0.450	
Methyl-	CH_2	UA	0.118	3.905	-0.375	(Dacquin et al. 2010)
sulfonic						
acid						
	SO_3H	S	0.250	3.550	1.3901	
		O=	0.170	2.960	-0.568	
		O=	0.170	2.960	-0.568	
		O-	0.170	3.120	-0.707	
		H	-	-	0.507	

Table A-2: Bond lengths data for the surface groups.

Group	**Bond**	***l* [Å]**	**K/k_B *****	**[kcal/mol/Å^2]**
Amino-methyl	Si-C	1.880		-
	C-N	1.448		383
Amino-Propyl	Si-C	1.880		-
	C-C	1.526		310
	C-N	1.448		383
Diamino-phenyl	Si-C_6H_3	1.865		-
	C-N	1.340		-
Aceto-nitrile	Si-C	1.880		-
	C-C	1.460		-
	CN	1.170		-

PEG	Si-C	1.880	-
	C-C	1.526	310
	C-O	1.430	310
	O-H	0.950	-
THF	Si-C	1.880	-
	C-C	1.530	-
	C-O	1.410	-
Acetone	Si-C	1.880	-
	C=O	1.229	
	C-C	1.520	310
Methyl-acetate	Si-C	1.880	-
	C=O	1.200	-
	C-O	1.344	-
	C-C	1.520	310
	CH_3-O	1.437	-
Propanoic acid	Si-C	1.880	-
	C-C	1.526	310
	C=O	1.214	-
	C-O	1.364	-
	O-H	0.970	-
Benzoic acid	C_6H_3-C	1.520	-
	C=O	1.214	-
	C-O	1.364	-
	O-H	0.970	-
Methyl-sulfonic acid	Si-C	1.880	-
	C-S	1.770	340
	S-O	1.567	-
	S=O	1.427	-
	O-H	0.959	-

Table A-3: Bond angles data for the surface groups.

Group	Bonds	Angle [°]	K [K/rad^2] ***
Amino-methyl	Si-C-N	112.0	31250
Amino-propyl	Si-C-C	112.0	31250
	C-C-C	112.0	31250
	C-C-N	112.0	31250
Diamino-phenyl	C-C-N	120.0	-
Aceto-nitrile	Si-C-C	112.0	-
PEG	Si-C-C	112.0	31250
	C-C-O	108.0	31250
	C-O-C	108.0	31250
	C-O-H	107.0	-
THF	C^2-C^3-C^4 and	105.1	-
	C^3-C^2-C^1		
	C^2-C^1-O and	109.4	-
	C^3-C^4-O		
	C^1-O-C^4	111.0	-
Acetone	C-C-O	121.4	31250
	C-C-C	117.2	31250
Methyl-acetate	C-O-C	115.0	31250
	O=C-C	125.0	31250
	C-C-O	110.0	31250
Propanoic acid	C-C-C	112.0	31250
	O-C=O	123.0	-
	C-C-O	111.0	-
	C-O-H	107.0	-
Benzoic acid	C_6H_3-C-O	111.0	-
	O-C-O	123.0	-
	C-O-H	107.0	-

Methyl-sulfonic acid	Si-C-S	108.6	-
	O=S=O	122.8	-
	S-O-H	109.1	-

Table A-4: Torsional data for the surface groups. In most cases the torsion parameters for the molecules were not reported, and thus are approximated to that of OPLS-AA for a simple alkyl chain (C-C-C-C).

Group	**Dihedral**	**V_o [kcal/mol]**	**V_1 [kcal/mol]**	**V_2 [kcal/mol]**	**V_3 [kcal/mol]**
Amino-propyl	C-C-C-C (AA)	-	1.411	-0.271	3.145
PEG	C-C-C(O)-C (AA)	-	-	0.820	-
Acetone	C-C-C-C (AA)	-	1.411	-0.271	3.145
Methyl-acetate	C-C-O-C (AA for ketones)	-	1454	-0.144	-0.775
Propanoic acid	C-C-C-C (AA)	-	1.411	-0.271	3.145

** Some references refer to the simulation of the molecules as bulk fluids. In such cases slight modifications were made in order to account for the Si-molecule bond besides adjusting the charges to keep the simulation cell neutral.

*** The bond bending and stretching parameters (Jorgensen et al. 1996) were used to add realism to the surface group mobility, rather than unrealistically allow it to move without constraints. However, in those cases where this was hardly possible to do the bond lengths and angles were fixed.

**** THF as presented by Girard *et al.* (Girard and Müller-Plathe 2003) can be represented by either twisted, envelope or planar conformations. The simplest of them all – planar – is said to be sufficient to faithfully represent its molecular behaviour and thus is the one selected for the purpose of this study.

8.1.1. Schematic representation of the surface groups

These images were obtained through VMD (software version 1.8.7), using surface group configurations taken from the simulations. The grey area is the wall surface, green denotes the OPLS-UA CH_2 molecules, blue is for nitrogen, white is for hydrogens, yellow is for sulphur, and red indicate oxygen atoms.

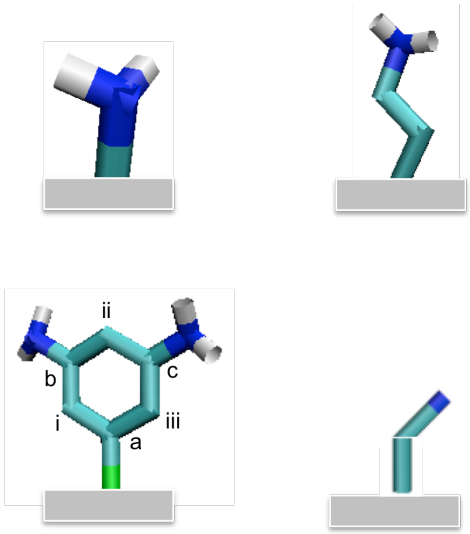

Figure A-1: Clockwise from the top-left corner: amino-methyl, amino-propyl, aceto-nitrile, and diamino-phenyl surface groups.

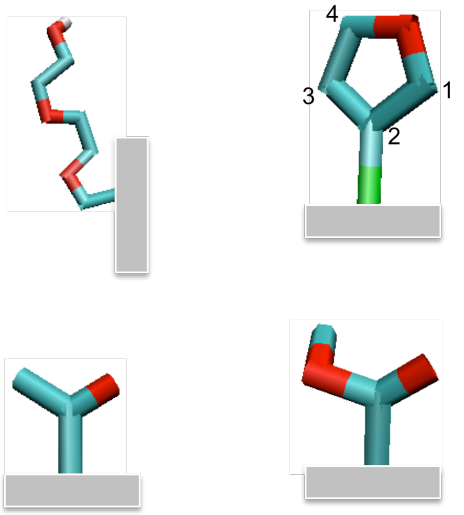

Figure A-2: Clockwise from the top-left corner: PEG, THF, methyl-acetate, and acetone surface groups.

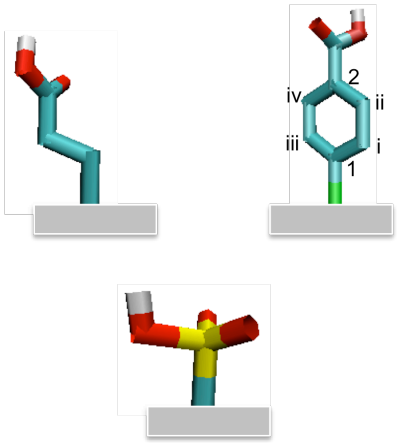

Figure A-3: From the top-left corner, clockwise: propanoic acid, benzoic acid, and methyl-sulfonic acid.

Al-Sahhaf, T. A. (1990) Vapor--liquid equilibria for the ternary system N2 + CO2 + CH4 at 230 and 250 K. *Fluid Phase Equilibria,* 55**,** 159-172.
Arfken, G. 1985. *The Method of Steepest Descents*. Orlando: Academic Press.
Atluri, R., Z. Bacsik, N. Hedin & A. E. Garcia-Bennett (2010) Structural variations in mesoporous materials with cubic Pmn symmetry. *Microporous and Mesoporous Materials,* 133**,** 27-35.
Atluri, R., N. Hedin & A. E. Garcia-Bennett (2008) Hydrothermal Phase Transformation of Bicontinuous Cubic Mesoporous Material AMS-6. *Chemistry of Materials,* 20**,** 3857-3866.
Babarao, R., Z. Hu, J. Jiang, S. Chempath & S. I. Sandler (2006) Storage and Separation of CO_2 and CH_4 in Silicalite, C_{168} Schwarzite, and IRMOF-1: A Comparative Study from Monte Carlo Simulation. *Langmuir,* 23**,** 659-666.
Bacsik, Z., R. Atluri, A. E. Garcia-Bennett & N. Hedin (2010a) Temperature-Induced Uptake of CO2 and Formation of Carbamates in Mesocaged Silica Modified with n-Propylamines. *Langmuir,* 26**,** 10013-10024.
Bacsik, Z. n., R. Atluri, A. E. Garcia-Bennett & N. Hedin (2010b) Temperature-Induced Uptake of CO2 and Formation of Carbamates in Mesocaged Silica Modified with n-Propylamines. *Langmuir,* 26**,** 10013-10024.
Battaile, C. C. (2008) The Kinetic Monte Carlo method: Foundation, implementation, and application. *Computer Methods in Applied Mechanics and Engineering,* 197**,** 3386-3398.
Battaile, C. C. & D. J. Srolovitz (2002) KINETIC MONTE CARLO SIMULATION OF CHEMICAL VAPOR DEPOSITION. *Annual Review of Materials Research,* 32**,** 297-319.
Bera, S. & I. Manna (2006) Hexagonal close packed to face centered cubic polymorphic transformation in nanocrystalline titanium-zirconium system by mechanical alloying. *Journal of Alloys and Compounds,* 417**,** 104-108.
Bezus, A. G., A. V. Kiselev, A. A. Lopatkin & P. Q. Du (1978) Molecular statistical calculation of the thermodynamic adsorption characteristics of zeolites using the atom-atom approximation. Part 1.-Adsorption of methane by zeolite NaX. *Journal of the Chemical Society, Faraday Transactions 2: Molecular and Chemical Physics,* 74**,** 367-379.
Blanc, E. & et al. (1996) X-ray diffraction study of the stacking faults in hexagonal C 70 single crystals. *EPL (Europhysics Letters),* 33**,** 205.
Briggs, J. M., T. B. Nguyen & W. L. Jorgensen (1991) Monte Carlo simulations of liquid acetic acid and methyl acetate with the OPLS potential functions. *The Journal of Physical Chemistry,* 95**,** 3315-3322.
Catlow, C. R. A., L. Ackermann, R. G. Bell, F. Cora, D. H. Gay, M. A. Nygren, J. C. Pereira, G. Sastre, B. Slater & P. E. Sinclair (1997) Computer modelling as a technique in solid state chemistry - Introductory lecture. *Faraday Discussions***,** 1-40.
Cavenati, S., C. A. Grande & A. r. E. Rodrigues (2006) Removal of Carbon Dioxide from Natural Gas by Vacuum Pressure Swing Adsorption. *Energy & Fuels,* 20**,** 2648-2659.

CECAM. 2010. Centre Europeen de Calcule Atomique et Moleculaire. ed. E. P. F. d. Lausanne. Lausanne.

Chang, A. C. C., S. S. C. Chuang, M. Gray & Y. Soong (2003) In-Situ Infrared Study of CO2 Adsorption on SBA-15 Grafted with Î³-(Aminopropyl)triethoxysilane. *Energy & Fuels,* 17**,** 468-473.

Corma, A. (1997) From microporous to mesoporous molecular sieve materials and their use in catalysis. *Chemical Reviews,* 97**,** 2373-2419.

Dacquin, J.-P., H. E. Cross, D. R. Brown, T. Duren, J. J. Williams, A. F. Lee & K. Wilson (2010) Interdependent lateral interactions, hydrophobicity and acid strength and their influence on the catalytic activity of nanoporous sulfonic acid silicas. *Green Chemistry,* 12**,** 1383-1391.

Davies, G. M., N. A. Seaton & V. S. Vassiliadis (1999) Calculation of pore size distributions of activated carbons from adsorption isotherms. *Langmuir,* 15**,** 8235-8245.

Delgado, J., M. Uguina, J. Sotelo, B. Ruíz & M. Rosário (2007) Separation of carbon dioxide/methane mixtures by adsorption on a basic resin. *Adsorption,* 13**,** 373-383.

Desideri, U. & A. Paolucci (1999) Performance modelling of a carbon dioxide removal system for power plants. *Energy Conversion and Management,* 40**,** 1899-1915.

Düren, T. 2002. Molecular modelling of equilibrium adsorption and transport diffusion in microporous solids. Hamburg: Technischen Universitat Hamburgh.

Düren, T., Y. S. Bae & R. Q. Snurr (2009) Using molecular simulation to characterise metal-organic frameworks for adsorption applications. *Chemical Society Reviews,* 38**,** 1237-1247.

Düren, T., F. Millange, G. Férey, K. S. Walton & R. Q. Snurr (2007) Calculating Geometric Surface Areas as a Characterization Tool for Metal−Organic Frameworks. *The Journal of Physical Chemistry C,* 111**,** 15350-15356.

Düren, T. & R. Q. Snurr (2007) Using molecular simulation to characterise metal-organic frameworks and judge their performance as adsorbents. *Characterisation of porous solids VII, Studies in Surface Science and Catalysis,* 160-161.

Ebenezer, S. A. 2005. Removal of Carbon Dioxide from Natural Gas for LNG Production. Trondheim, Norway: Institute of Petroleum Technology, Norwegian University of Science and Technology.

Fiaschi, D. & L. Lombardi (2002) Integrated Gasifier Combined Cycle Plant with Integrated CO2-H2S Removal: Performance Analysis, Life Cycle Assessment and Exergtic Life Cycle Assessment. *International Journal of Applied Thermodynamics,* 5**,** 13-24.

Firouzi, A., D. Kumar, L. Bull, T. Besier, P. Sieger, Q. Huo, S. Walker, J. Zasadzinski, C. Glinka & J. Nicol (1995) Cooperative organization of inorganic-surfactant and biomimetic assemblies. *Science,* 267**,** 1138-1143.

Frenkel, D. & B. Smit. 2001. *Understanding Molecular Simulation, Second Edition: From Algorithms to Applications (Computational Science Series, Vol 1)*. Academic Press.

Gadelmawla, E. S., M. M. Koura, T. M. A. Maksoud, I. M. Elewa & H. H. Soliman (2002) Roughness parameters. *Journal of Materials Processing Technology,* 123**,** 133-145.

García-Pérez, E., J. Parra, C. Ania, A. García-Sánchez, J. van Baten, R. Krishna, D. Dubbeldam & S. Calero (2007) A computational study of CO2, N2, and CH4 adsorption in zeolites. *Adsorption,* 13**,** 469-476.

Garofalini, S. H. & G. Martin (1994) Molecular Simulations of the Polymerization of Silicic Acid Molecules and Network Formation. *The Journal of Physical Chemistry,* 98**,** 1311-1316.

Girard, S. & F. Müller-Plathe (2003) Molecular dynamics simulation of liquid tetrahydrofuran: on the uniqueness of force fields. *Molecular Physics: An International Journal at the Interface Between Chemistry and Physics,* 101**,** 779-787.

Girard, S. e. a. (2003) Molecular dynamics simulation of liquid tetrahydrofuran: on the uniqueness of force fields. *Molecular Physics: An International Journal at the Interface Between Chemistry and Physics,* 101**,** 779-787.

Gonzalez, J. 2005. Adsorption properties of organically functionalised mesoporous solids and dynamics of adsorbed molecules in miroporous organic-inorganic hybrid solids. In *Chemistry*. St. Andrews, UK: University of St. Andrews.

Harris, J. G. & K. H. Yung (1995) Carbon Dioxide's Liquid-Vapor Coexistence Curve And Critical Properties as Predicted by a Simple Molecular Model. *The Journal of Physical Chemistry,* 99**,** 12021-12024.

Herdes, C., C. Ferreiro & T. Duren. 2011. Predicting neopentane isosteric enthalpy of adsorption at zero coverage in MCM-41. In *Langmuir (in revision)*.

Hill, T. L. 1956. *Statistical Mechanics: Principles and Selected Applications*. USA: McGraw-Hill.

Hunter, H. M. & P. A. Wright (2001) Synthesis and characterisation of the mesoporous silicate SBA-2 and its performance as an acid catalyst. *Microporous and Mesoporous Materials,* 43**,** 361-373.

Huo, Q., D. I. Margolese, U. Ciesla, D. G. Demuth, P. Feng, T. E. Gier, P. Sieger, A. Firouzi & B. F. Chmelka (1994a) Organization of Organic Molecules with Inorganic Molecular Species into Nanocomposite Biphase Arrays. *Chemistry of Materials,* 6**,** 1176-1191.

Huo, Q. S., R. Leon, P. M. Petroff & G. D. Stucky (1995) Mesostructure Design with Gemini Surfactants - Supercage Formation in a 3-Dimensional Hexagonal Array. *Science,* 268**,** 1324-1327.

Huo, Q. S., D. I. Margolese, U. Ciesla, P. Y. Feng, T. E. Gier, P. Sieger, R. Leon, P. M. Petroff, F. Schuth & G. D. Stucky (1994b) Generalized Synthesis of Periodic Surfactant Inorganic Composite-Materials. *Nature,* 368**,** 317-321.

Huo, Q. S., D. I. Margolese & G. D. Stucky (1996) Surfactant control of phases in the synthesis of mesoporous silica-based materials. *Chemistry of Materials,* 8**,** 1147-1160.

Jorgensen, W. L., J. M. Briggs & M. L. Contreras (1990) Relative partition coefficients for organic solutes from fluid simulations. *The Journal of Physical Chemistry,* 94**,** 1683-1686.

Jorgensen, W. L., J. D. Madura & C. J. Swenson (1984) Optimized Intermolecular Potential Functions for Liquid Hydrocarbons. *Journal of the American Chemical Society,* 106**,** 6638-6646.

Jorgensen, W. L., D. S. Maxwell & J. TiradoRives (1996) Development and testing of the OPLS all-atom force field on conformational energetics and properties of organic liquids. *Journal of the American Chemical Society,* 118**,** 11225-11236.

Kalke, M. & D. V. Baxter (2001) A kinetic Monte Carlo simulation of chemical vapor deposition: non-monotonic variation of surface roughness with growth temperature. *Surface Science,* 477**,** 95-101.

Kamath, G., G. Georgiev & J. J. Potoff (2005) Molecular Modeling of Phase Behavior and Microstructure of Acetoneâˆ'Chloroformâˆ'Methanol Binary Mixtures. *The Journal of Physical Chemistry B,* 109**,** 19463-19473.

Kim, J. M. & G. D. Stucky (2000) Synthesis of highly ordered mesoporous silica materials using sodium silicate and amphiphilic block copolymers. *Chemical Communications***,** 1159-1160.

Knofel, C., C. Martin, V. Hornebecq & P. L. Llewellyn (2009) Study of Carbon Dioxide Adsorption on Mesoporous Aminopropylsilane-Functionalized Silica and Titania Combining Microcalorimetry and in Situ Infrared Spectroscopy. *The Journal of Physical Chemistry C,* 113**,** 21726-21734.

Konduru, N., P. Lindner & N. M. Assaf-Anid (2007) Curbing the greenhouse effect by carbon dioxide adsorption with Zeolite 13X. *AIChE Journal,* 53**,** 3137-3143.

Kratzer, P. (2009) Monte Carlo and Kinetic Monte Carlo Methods - A Tutorial. *Multiscale Simulation Methods in Molecular Sciences,* 42**,** 51-76.

Kresge, C. T., M. E. Leonowicz, W. J. Roth, J. C. Vartuli & J. S. Beck (1992) Ordered Mesoporous Molecular-Sieves Synthesized by a Liquid-Crystal Template Mechanism. *Nature,* 359**,** 710-712.

Lanza, G. & C. Minichino (2009) How an Inert-Gas Matrix Can Modify the Molecular Properties of Lanthanide Trifluoride. *ChemPhysChem,* 10**,** 507-511.

Lin, H.-m. (1984) Peng-Robinson equation of state for vapor-liquid equilibrium calculations for carbon dioxide + hydrocarbon mixtures. *Fluid Phase Equilibria,* 16**,** 151-169.

Linstrom, P. J. & W. G. Mallard. 2003. *Thermophysical Properties of Fluid Systems in NIST Chemistry WebBook*. Gaithersburgh MC: National Institute of Standards and Technology.

Lu, G. Q. & X. S. Zhao. 2004. *Nanoporous Materials - Science and Engineering*. London: World Scientific.

Murthy, C. S., K. Singer, M. L. Klein & I. R. McDonald (1980) Pairwise additive effective potentials for nitrogen. *Molecular Physics: An International Journal at the Interface Between Chemistry and Physics,* 41**,** 1387 - 1399.

Myers, A. L. & P. A. Monson (2002) Adsorption in Porous Materials at High Pressure: Theory and Experiment. *Langmuir,* 18**,** 10261-10273.

Ng, L. V. & A. V. McCormick (1996) Acidic sol-gel polymerization of TEOS: Effect of solution composition on cyclization and bimolecular condensation rates. *Journal of Physical Chemistry,* 100**,** 12517-12531.

Nicholson, D. & E. Gubbins (1996) Separation of carbon dioxide-methane mixtures by adsorption: Effects of geometry and energetics on selectivity. *J. Chem. Phys,* 104**,** 8126-8134.

Perez-Mendoza, M., J. Gonzalez, P. A. Wright & N. A. Seaton (2004a) Elucidation of the pore structure of SBA-2 using Monte Carlo simulation to interpret experimental data for the adsorption of light hydrocarbons. *Langmuir,* 20**,** 7653-7658.

--- (2004b) Structure of the mesoporous silica SBA-2, determined by a percolation analysis of adsorption. *Langmuir,* 20**,** 9856-9860.

Perez-Mendoza, M. J. 2007-2010. personal reference. Universidad de Granada, Spain.

Press, W. H., B. P. Flannery, S. A. Teukolsky & W. T. Vetterling. 1992. *Numerical Recipes in FORTRAN: The Art of Scientific Computing*. Cambridge, England: Cambridge University Press.

Prof. Wright, r. g. 2007-2010. personal reference. University of St. Andrews.

Reuter, K. & M. Scheffler (2006) First-principles kinetic Monte Carlo simulations for heterogeneous catalysis: Application to the CO oxidation at RuO_{2}(110). *Physical Review B,* 73**,** 045433.

Richardi, J., P. H. Fries, R. Fischer, S. Rast & H. Krienke (1997) Structure and thermodynamic of liquid acetonitrile via Monte Carlo simulation and Ornstein-Zernike theories. *Journal of Molecular Liquids,* 74,74**,** 465-485.

Rouquerol, F., J. Rouquerol & K. Sing. 1999. *Adsorption by Powder & Porous Solid*. London: Academic Press.

Sandler, S. I. 1999. *Chemical and Engineering Thermodynamics*. USA: Wiley.

Sarnthein, J., A. Pasquarello & R. Car (1995) Model of Vitreous Sio2 Generated by an Ab-Initio Molecular-Dynamics Quench from the Melt. *Physical Review B,* 52**,** 12690-12695.

Schumacher, C. 2005. Design of Hybrid Organic/Inorganic Adsorbents for Gas Separation. In *Institute for Materials and Processes*. Edinburgh: The University of Edinburgh.

Schumacher, C., J. Gonzalez, M. Perez-Mendoza, P. A. Wright & N. A. Seaton (2006a) Design of hybrid organic/inorganic adsorbents based on periodic mesoporous silica. *Industrial & Engineering Chemistry Research,* 45**,** 5586-5597.

Schumacher, C., J. Gonzalez, P. A. Wright & N. A. Seaton (2006b) Generation of atomistic models of periodic mesoporous silica by kinetic Monte Carlo simulation of the synthesis of the material. *Journal of Physical Chemistry B,* 110**,** 319-333.

Serna-Guerrero, R., Y. Belmabkhout & A. Sayari (2010) Modeling CO2 adsorption on amine-functionalized mesoporous silica: 1. A semi-empirical equilibrium model. *Chemical Engineering Journal,* 161**,** 173-181.

Stoll, J., J. Vrabec & H. Hasse (2003) Vapor-liquid equilibria of mixtures containing nitrogen, oxygen, carbon dioxide, and ethane. *Aiche Journal,* 49**,** 2187-2198.

Sweatman, M. B. (2010) Equilibrium behaviour of a novel gas separation process, with application to carbon capture. *Chemical Engineering Science,* 65**,** 3907-3913.

Talu, O. & A. L. Myers (2001) Molecular simulation of adsorption: Gibbs dividing surface and comparison with experiment. *Aiche Journal,* 47**,** 1160-1168.

Torrens, F. & G. Castellano (2006) Fractal Dimension of Active-Site Models of Zeolite Catalysts. *Journal of Nanomaterials,* 2006**,** 17052.

Tu, Y. & J. Tersoff (2000) Structure and energetics of the Si-SiO2 interface. *Physical Review Letters,* 84**,** 4393-4396.
UK Research Council, U. (2011) Carbon Capture and Storage. http://www.co2storage.org.uk/ (last accessed.
van Wylen, G. J. & R. E. Sonntag. 1986. *Fundamentals of Classical Thermodynamics*. John Wiley & Sons Inc.
Varn, D. P., G. S. Canright & J. P. Crutchfield (2002) Discovering planar disorder in close-packed structures from x-ray diffraction: Beyond the fault model. *Physical Review B,* 66**,** 174110.
Voter, A. F. (2005) Introduction to the Kinetic Monte Carlo Method.
Williams, J. J., A. D. Wiersum, N. A. Seaton & T. DuÌˆren (2010a) Effect of Surface Group Functionalization on the CO2/N2 Separation Properties of MCM-41: A Grand-Canonical Monte Carlo Simulation Study. *The Journal of Physical Chemistry C,* 114**,** 18538-18547.
Williams, J. J., A. D. Wiersum, N. A. Seaton & T. Düren (2010b) Effect of Surface Group Functionalization on the CO2/N2 Separation Properties of MCM-41: A Grand-Canonical Monte Carlo Simulation Study. *The Journal of Physical Chemistry C,* 114**,** 18538-18547.
Wu, M. G. & M. W. Deem (2002) Monte Carlo study of the nucleation process during zeolite synthesis. *Journal of Chemical Physics,* 116**,** 2125-2137.
Yang, R. T. 1997. *Gas separation by adsorption processes*. Singapore.
Yun, J.-H., T. Düren, F. J. Keil & N. A. Seaton (2002) Adsorption of Methane, Ethane, and Their Binary Mixtures on MCM-41: Experimental Evaluation of Methods for the Prediction of Adsorption Equilibrium. *Langmuir,* 18**,** 2693-2701.
Zelenak, V., D. Halamova, L. Gaberova, E. Bloch & P. Llewellyn (2008) Amine-modified SBA-12 mesoporous silica for carbon dioxide capture: Effect of amine basicity on sorption properties. *Microporous and Mesoporous Materials,* 116**,** 358-364.
Zhao, D. Y., Q. S. Huo, J. L. Feng, B. F. Chmelka & G. D. Stucky (1998) Nonionic triblock and star diblock copolymer and oligomeric surfactant syntheses of highly ordered, hydrothermally stable, mesoporous silica structures. *Journal of the American Chemical Society,* 120**,** 6024-6036.
Zhou, W. Z., H. M. A. Hunter, P. A. Wright, Q. F. Ge & J. M. Thomas (1998) Imaging the pore structure and polytypic intergrowths in mesoporous silica. *Journal of Physical Chemistry B,* 102**,** 6933-6936.